Title
The Structure and Stellar Populations of Nuclear Star Clusters in Late-Type Spiral Galaxies

Author
Carson, Daniel James

Publication Date
2016

Peer reviewed|Thesis/dissertation

UNIVERSITY OF CALIFORNIA,
IRVINE

The Structure & Stellar Populations of Nuclear Star Clusters in Late-Type Spiral Galaxies

DISSERTATION

submitted in partial satisfaction of the requirements
for the degree of

DOCTOR OF PHILOSOPHY

in Physics

by

Daniel J. Carson

Dissertation Committee:
Professor Aaron Barth, Chair
Associate Professor Michael Cooper
Professor James Bullock

2016

TABLE OF CONTENTS

LIST OF FIGURES

LIST OF TABLES

ACKNOWLEDGMENTS

Support for program GO-12163 was provided by NASA through a grant from the Space Telescope Science Institute, which is operated by the Association of Universities for Research in Astronomy, Inc., under NASA contract NAS 5-26555. This research has made use of the NASA/IPAC Extragalactic Database (NED) which is operated by the Jet Propulsion Laboratory, California Institute of Technology, under contract with the National Aeronautics and Space Administration. I acknowledge the usage of the HyperLeda database (http://leda.univ-lyon1.fr).

Some of the text of this dissertation is a reprint of the material as it appears in the Astronomical Journal. Permission to use copyrighted material has been granted by the Astronomical Journal. The co-authors listed in this publication directed and supervised research which is the basis for the dissertation. I would like to thank my research collaborators Anil Seth, Mark den Brok, Luis Ho, Jenny Greene, Michele Cappellari, and Nadine Neumayer.

I would like to thank my advisor, Aaron Barth, for years of guidance and support, as well the members of the Barth research group past and present, especially Liuyi Pei, Ben Boizelle, Jonelle Walsh, Carol Hood, Daeseong Park, and Vivian U.

None of this would have been possible without the love and support of my wonderful family and friends. I am grateful for the encouragement my parents Tom and Judy Carson, my sister Nora Carson, my (soon to be) brother-in-law Jordan David, and my dear friends Paul Mockus, Alex Kirschenbaum, Beverly Tsai, Jay Mata, Jessica Mata, Steve Buchsbaum, Max Weidmann, Calvin Patel, Emon Heidari, and Coral Wheeler.

CURRICULUM VITAE

Daniel J. Carson

EDUCATION

Doctor of Philosophy in Physics & Astronomy **2016**
University of California, Irvine *Irvine, CA*

Master of Science in Physics **2011**
University of California, Irvine *Irvine, CA*

Bachelor of Science in Physics, Minor in Mathematics **2010**
University of Illinois at Urbana-Champaign *Urbana-Champaign, IL*

RESEARCH EXPERIENCE

Graduate Student Researcher **2011–2016**
University of California, Irvine *Irvine, California*

Undergraduate Researcher **2009–2010**
University of Illinois at Urbana-Champaign *Urbana-Champaign, Illinois*

TEACHING EXPERIENCE

Teaching Associate **2015–2016**
University of California, Irvine *Irvine, CA*

Tutor, Minority Sciences Program **2014–2015**
University of California, Irvine *Irvine, CA*

Teaching Assistant **2010–2011**
University of California, Irvine *Irvine, CA*

FIRST AUTHOR REFEREED JOURNAL PUBLICATIONS

The Structure of Nuclear Star Clusters in Late-type Spiral Galaxies from Hubble Space Telescope/Wide Field Camera 3 Imaging **2015**
The Astronomical Journal

FIRST AUTHOR PAPERS IN PREPARATION

The Stellar Populations of Nuclear Star Clusters in Late-type Spiral Galaxies from Hubble Space Telescope/Wide Field Camera 3 Imaging **2016**

OTHER REFEREED JOURNAL PUBLICATIONS CONTRIBUTED TO

Measuring the Mass of the Central Black Hole in the Bulgeless Galaxy NGC 4395 from Gas Dynamical Modeling **2015**
The Astrophysical Journal

Reverberation Mapping of the KEPLER Field AGN KA1858+4850 **2014**
The Astrophysical Journal

A Search for Optical Variability of Type 2 Quasars in SDSS Stripe 82 **2014**
The Astrophysical Journal

The Very Young Type Ia Supernova 2012cg: Discovery and Early-time Follow-up Observations **2012**
The Astrophysical Journal

ABSTRACT OF THE DISSERTATION

The Structure & Stellar Populations of Nuclear Star Clusters in Late-Type Spiral Galaxies

By

Daniel J. Carson

Doctor of Philosophy in Physics

University of California, Irvine, 2016

Professor Aaron Barth, Chair

Luminous, compact stellar systems known as nuclear clusters (NCs) are commonly found in the centers of galaxies across the entire Hubble sequence. I present an analysis of the structure and stellar populations of a sample of ten of the nearest and brightest NCs residing in late-type spiral galaxies, using images from Hubble Space Telescope Wide Field Camera 3 in seven bands that span the near-ultraviolet to the near-infrared in wavelength. The intrinsic shapes and sizes of the NCs, disentangled from the effects of point spread function (PSF) blurring, were measured using `GALFIT`. We find evidence for radial color gradients within the NCs, as well as young disk structures aligned with the host galaxy disk. In color-color diagrams spanning the near-UV through the near-IR, NCs tend to lie far from single-burst evolutionary tracks, indicating the presence of multi-age populations.

I developed a Monte Carlo code to fit linear combinations of simple stellar population models to the observed spectral energy distribution (SED) of each NC and assess the uncertainties in the fit parameters. Tests on a catalog of mock SEDs demonstrate that our method gives unbiased mass age, and reddening estimates for populations with $U-V$ colors redder than ~ -2 mag. Stellar masses computed via SED fitting are in good agreement with previous dynamical studies. The NCs are generally dominated by an old ($>$ 1 Gyr) population component, but are best described by temporally extended star formation histories. On average, populations with ages < 100 Myr contribute 1.8% of the total stellar mass and 10.4% of the total B-band luminosity. From spatially resolved stellar population modeling, we compute maps of stellar density and age, which reveal radial age gradients. Multi-Gaussian Expansion models of NC stellar surface density, which will be used in future dynamical studies, are presented. We report an effective surface density of $6.7^{+6.3}_{-1.8} \times 10^5$ $M_\odot$ pc^{-2} within $R_{\rm eff} = 2.0$ pc in IC 342, the densest cluster in our sample. Finally, we find evidence that NCs are more metal rich than their host galaxies, indicating that the inspiral of globular clusters is not the dominant growth mechanism in NCs.

Chapter 1

Introduction

The nucleus of a galaxy is a unique location because it corresponds to the bottom of the galaxy's potential well. Galactic nuclei commonly host many distinctive and interesting phenomena, such as supermassive black holes (SMBHs), active galactic nuclei (AGN), and bursts of star formation. Since the advent of CCD astronomy and space-based telescopes, it has become apparent that galactic nuclei are also home to luminous and dense stellar systems known as nuclear clusters (NCs). With typical half-light radii of a just few parsecs and dynamical masses of $\sim 10^6 - 10^7\ M_\odot$ (Böker et al., 1999, 2002; Walcher et al., 2005), NCs are the densest class of stellar systems in the Universe.

NCs were first detected as unresolved central light excesses in galaxy centers. In a *Hubble Space Telescope* (*HST*) Planetary Camera survey of 20 nearby disk galaxies, Phillips et al. (1996) noted that many of the galaxies in the sample had a sharply rising surface brightness profile in the center, in excess what would be expected from inward extrapolation of the surface brightness profile in the inner few arcseconds. Using ground-based imaging, Matthews & Gallagher (1997) detected unresolved nuclei in ten out of a sample of 49 extreme late-type spiral galaxies in the Southern Hemisphere. Despite the importance of these findings, only NCs in the nearest galaxies (e.g., M33) could only be spatially resolved before Wide Field and Planetary Camera 2 (WFPC2) was installed on *HST*. WFPC2 improved on its predecessor by incorporating corrective optics needed to overcome *HST*'s primary mirror defect, and paved the way for more detailed studies of the properties of NCs.

WFPC2 imaging surveys of NCs in the late 1990s and early 2000s established that NCs are a common feature of galaxies across the entire Hubble sequence. An NC was unambiguously detected in 75% of late-type (Scd-Sm) spirals in a survey by Böker et al. (2002), 50% of earlier-type (Sa-Sc) spirals in a survey by Carollo et al. (1997), and 70% of ellipticals (E and S0) in a survey by Côté et al. (2006). WFPC2 surveys also allowed for the structure of a large sample of NCs to be studied for the first time. To estimate the physical scale and luminosity of a sample of 35 NCs, Carollo et al. (1997) fit analytic models to one-dimensional (1D) radial surface brightness profiles measured from WFPC2 photometry, and showed that NCs are distinct from classical bulges. Matthews et al. (1999) obtained WFPC2 images of four NCs in late-type spiral galaxies and fit two-dimensional (2D) surface brightness models to the data, demonstrating that none of the nuclei could be adequately fit by a point source.

Subsequent surveys by Böker et al. (2002, 2004) provided further insights into the structural properties of NCs, as well as some of the first hints that properties of NCs are correlated with their host galaxies, with the observation that the luminosity of the NC scales with the luminosity of the host galaxy. These studies also showed that NCs are extremely compact, with typical effective radii of a few parsecs. The distribution of NC sizes is narrow and nearly identical to that of globular clusters (GCs) in the Milky Way. However, despite the structural similarities of NCs and GCs, it was found that NCs are on average 4 magnitudes brighter.

Another property of NCs that sets them apart from GCs are their complex star formation histories. Spectroscopic surveys in the mid 2000s carried out with the Space Telescope Imaging Spectrograph (STIS) on board *HST*, as well as various ground based telescopes, helped establish the basic stellar population properties of nuclear clusters. The development of high-resolution stellar population synthesis models by Bruzual & Charlot (2003a) made such studies possible. It has repeatedly been demonstrated that NCs in late-type spiral galaxies do in fact have complex, multi-age stellar populations, and their spectra are often consistent with a continuous star formation history (Walcher et al., 2006; Rossa et al., 2006; Seth et al., 2006). There is also limited evidence that nuclei of early-type galaxies also have complex star formation histories (Monaco et al., 2009; Seth et al., 2010; Lyubenova et al., 2013). The Walcher et al. (2006) study found that only linear combinations of single-age models yield mass-to-light ratios that match those obtained from dynamical measurements. For this sample of NCs in late-type galaxies, the last star formation episode was on average 34 Myr ago, indicating that they have undergone repeated episodes of star formation. Rossa et al. (2006) found that NCs in late-type spirals are on average younger and less massive than NCs in early-type spirals. Mass-weighted ages are ~ 0.7 dex older than luminosity weighted ages for NCs in late-type and early-type galaxies, indicating the presence of an underlying older population that does not contribute much light but contains a significant fraction of the mass. Nuclear cluster masses strongly correlate with both the Hubble types of their host galaxies and the luminosities of their bulges, much like black holes (BHs). Any plausible scenario for how NCs form has to account for the connection between NCs and their host galaxies.

In addition to having complex stellar populations, NCs are also structurally complex. In a study of nine NCs in edge-on, late-type galaxies imaged with *HST*/Advanced Camera for Surveys, Seth et al. (2006) found evidence for multiple, coincident structural components in three of the clusters. The elongated components, which represent nuclear stellar disks or rings, are younger than the spheroidal components and are aligned with the host galaxies' major axes. *HST* imaging studies by Georgiev & Böker (2014) and Carson et al. (2015) have uncovered evidence for radially varying stellar populations in the nuclei of late-type galaxies, in the sense that their half-light radii tend to be smaller when measured in bluer filters.

Although more detailed studies of the spatially resolved properties of NC stellar populations have been conducted for M33 (Lauer et al., 1998) and the Milky Way (Paumard et al., 2006; Lu et al., 2013; Schödel et al., 2014; Feldmeier-Krause et al., 2015), a comprehensive, multi-band study with a large sample of NCs has not been carried out.

Due to the fact that NCs reside at the bottom of their host galaxy's potential well, the process of formation and growth of a nuclear cluster is likely to be complex. Two main scenarios have been proposed to explain the formation of NCs: in-situ formation from the accretion of low angular momentum gas onto the galactic nucleus (Milosavljević, 2004), and mergers of globular clusters migrating towards the galactic nucleus due to dynamical friction (Tremaine et al., 1975; Lotz et al., 2001). Evidence from observations and N-body simulations indicates that both processes are plausible, and some combination of the two is probably at work. Hartmann et al. (2011) compared simulations of the migratory/merger scenario with integral field unit (IFU) observations of NGC 4244, and found that in-situ formation accounts for at least 50% of the NC's mass. Antonini (2013, 2014) and Arca-Sedda & Capuzzo-Dolcetta (2014) demonstrated that the migratory/merger scenario predicts correlations between the masses of NCs and global properties of their host galaxies that match observed correlations. The young populations observed in most NCs rule out the sinking of globular clusters as the sole process for NC formation (i.e., the sinking of younger star clusters or gas accretion must play some role). However, our understanding of the formation of NCs is still incomplete.

NCs are structurally similar to ultra-compact dwarf (UCD) galaxies (Phillipps et al., 2001), which led to the intriguing proposal that UCDs may be the remnant nuclei of tidally disrupted dwarf elliptical (dE) galaxies (Bekki et al., 2001; Böker, 2008; Seth et al., 2014). UCDs are offset by about two orders of magnitude in luminosity from the $M_{\rm BH}$-luminosity relation, with overmassive BHs at a given galaxy luminosity Mieske et al. (2013). Georgiev & Böker (2014) found that the largest and brightest NCs in spiral galaxies occupy the regime between UCDs and the nuclei of early-type galaxies in the size-luminosity plane. These observations are all consistent with the idea originally put forth by Bekki et al. (2001). The nuclei of dEs may indeed be the progenitors of UCDs.

NCs share a connection with black holes (BHs), which are also often found in the nuclei of galaxies. NCs and BHs are known to coexist in galaxies of all Hubble types across a wide range of masses (Seth et al., 2008a), but some NCs have no central BH down to highly constraining limits. The NC in NGC 4935, for example, contains a NC (Filippenko & Ho, 2003) as well as a Type 1 active galactic nucleus (AGN) powered by accretion onto a central BH (Filippenko & Sargent, 1989), with mass estimates ranging from 5×10^4 to 3.6×10^5 $M_\odot$ (Peterson et al., 2005; Edri et al., 2012), while dynamical studies of the NC in M33, a galaxy with a similar mass to NGC 4395, have placed remarkably tight upper limits of 1500 – 3000 $M_\odot$ on the mass of any central BH (Gebhardt et al., 2001; Merritt et al., 2001). These studies indicate that at least some NCs can host a central BH, but the overall occupation fraction of BHs in NCs highly unconstrained.

Much like BHs, NCs obey scaling relations with properties of their host galaxies. The masses of both NCs (Ferrarese et al., 2006; Wehner & Harris, 2006) and BHs (Ferrarese & Merritt, 2000; Gebhardt et al., 2000; Häring & Rix, 2004) are correlated with the masses of their host galaxy bulges. Galaxies with mass above 10^{10} $M_\odot$ tend to host BHs, while less massive galaxies tend to host NCs, with a transition region for galaxies with mass 10^8 – 10^{10} $M_\odot$ where both objects coexist (Graham & Spitler, 2009). Interestingly, for galaxies known to contain both a NC and a central BH, the ratio $(M_{\rm BH} + M_{\rm NC})/M_{\rm bulge}$ (where $M_{\rm bulge}$ denotes the mass of the bulge or pseudobulge component of the host galaxy) shows less scatter than either $M_{\rm BH}/M_{\rm bulge}$ or $M_{\rm NC}/M_{\rm bulge}$ (Kormendy & Ho, 2013), suggesting a link between the building of NCs and BHs. These studies add to a growing body of evidence that NCs and BHs are both generic by-products of galaxy formation, and the growth mechanisms of NCs and BHs are somehow related (Ferrarese et al., 2006).

NCs in late-type galaxies offer a promising means to study intermediate-mass black holes

(IMBHs). With masses of $\sim 10^{4-6} M_{\odot}$, IMBHs are thought to be the initial seeds of present-day supermassive black holes (SMBHs) which have not experienced significant growth over cosmic time. Although the shape of the $M_{\rm BH} - \sigma_{*}$ and $M_{\rm BH} - M_{\rm bulge}$ relations are highly uncertain at the low mass end, a naive extrapolation towards the low-mass end suggests that NCs in late-type galaxies with little or no bulge component should harbor IMBHs. Pure disk galaxies have not experienced major merger events which fuel BH growth. BHs in late-type galaxies therefore represent a fossil record of the high-redshift seeds of present-day SMBHs.

Volonteri et al. (2008) followed the evolution of different high-redshift BH seeds from $z = 20$ to $z = 0$ in Monte Carlo merger tree simulations. They found that the present-day BH mass function strongly depends on the initial BH seed, which in their models is either the remnant of a Population III star or the result of a direct collapse of a metal-poor gas cloud. The Population III scenario leads to a higher occupation fraction of central BHs in late-type galaxies, and a much steeper $M_{\rm BH} - \sigma_{*}$ relation at the low-$M_{\rm BH}$ end. Dynamical studies of NCs in late-type galaxies can help to constrain the occupation fraction of IMBHs in late-type galaxies, as well as the shape of the $M_{\rm BH} - \sigma_{*}$ relation. In addition to improving our understanding of NC and BH demographics, dynamical studies NCs in late-type galaxies may also provide insights into how SMBHs are formed.

Although IMBHs are difficult targets for dynamical searches, dynamical modeling has been carried out on a limited number of NCs in late-type galaxies. Studies of IC 342 (Böker et al., 1999) and NGC 3621 (Barth et al., 2009) have constrained $M_{\rm BH}$ by using *HST* imaging and integrated stellar velocity dispersion measurements of the NC in order to carry out Jeans modeling of the clusters. Kormendy et al. (2010) and Neumayer & Walcher (2012) have also performed Jeans modeling of NCs in order to measure NC masses and set upper limits the masses of central BHs. Adaptive optics (AO) assisted IFU observations can resolve the kinematics of the nearest and brightest NCs and increase the sensitivity to BHs within the clusters. For example, Seth et al. (2010) placed an upper limit of $\sim 10^{5}\ M_{\odot}$ for the central BH in NGC 404 from dynamical modeling of the stellar kinematics of the NC using a combination of AO-assisted near-IR IFU spectroscopy, optical spectroscopy, and *HST* imaging. Using similar methods, Hartmann et al. (2011) measured a mass of 1.1×10^7 $M_\odot$ for the NC in NGC 4244, and found that if the NC hosts a central BH at all, its mass is less than 1% of the NC mass.

While previous dynamical studies of NCs have typically assumed a spatially uniform stellar mass-to-light ratio (M/L e.g., Böker et al., 1999; Walcher et al., 2005; Barth et al., 2009; Kormendy et al., 2010), better constraints on BH masses can be obtained by accounting for the fact that M/L of NCs is generally non-uniform. This can be achieved by incorporating results from spatially resolved stellar population modeling. Performing stellar population modeling at each resolution element in a set of images is a technique that has been widely used to study the spatially resolved properties of galaxies (e.g., Lanyon-Foster et al., 2007; Welikala et al., 2008; Zibetti et al., 2009; Welikala et al., 2009; Wuyts et al., 2012; Hemmati et al., 2014), but has not yet been applied to NCs. In addition to revealing variations in age, metallicity, and dust content across the galaxy, such studies are able to produce surface density maps, which are crucial ingredients in dynamical models.

Despite the substantial progress that has been made over the last two decades, there is still much to learn about the detailed structure and stellar populations of nuclear clusters. In this thesis, I present a an in depth analysis of a set of uniform, high-signal-to-noise (S/N), unsaturated images of NCs with wavelength coverage from the near-ultraviolet (UV) to the near-infrared (IR) for a sample of ten of the nearest late-type galaxies hosting NCs. The data represent a substantial improvement in spatial resolution, wavelength coverage, and homogeneity over previous imaging studies of NCs. Although all of the galaxies in our sample have archival *HST* images available from previous studies, the archival data are very heterogeneous, including images that are saturated in the core of the NC and images taken with several different cameras. The homogeneity of our data allows for a more detailed study of the NCs than would be possible with archival data alone.

The remainder of the document is organized as follows. Chapter 2 describes properties of the sample of NCs, and gives detailed description of the images taken with Wide Field Camera 3 on board *HST*. An analysis of the wavelength dependent structural properties of this sample of NCs, which was carried out via surface brightness profile fitting, is presented Chapter 3. Chapter 4 describes the analysis of the stellar population properties of the sample. This analysis was carried out by performing fits to the global spectral energy distribution (SED) of each NC, as well as performing SED fits on a pixel-by-pixel basis. A summary of the main results of this work and concluding remarks are given in Chapter 5. The Appendix outlines a series of tests we performed in order to determine the optimal number of single-age stellar population templates to include in our model SEDs and to determine the accuracy of our Monte Carlo SED fitting method.

Chapter 2

HST/WFC3 data

2.1 Sample Selection

We obtained *HST*/WFC3 images of ten of the nearest and brightest nuclear clusters in seven different filter bands, spanning the near-UV to near-IR in wavelength. The images were taken over a total of 20 *HST* orbits for the GO-12163 observing program.

The galaxies in our sample were selected according to the following criteria: Hubble type in the range Sc–Sm, distance < 5 Mpc (with one exception), and the presence of a nuclear star cluster with magnitude brighter than $V = 19$ mag. The Hubble type selection criterion ensures that the galaxies in our sample have little or no bulge component. NGC 3621, at a distance of 7 Mpc, was included in the sample because it is a rare example of a nearby galaxy containing a Type 2 AGN in its nuclear cluster (Satyapal et al., 2007; Barth et al., 2009). Basic properties of the galaxy sample are presented in Table 2.1. The morphological types, B-band magnitudes and heliocentric radial velocities listed in this table are from *The Third Reference Catalogue of Bright Galaxies* (de Vaucouleurs et al., 1991) and were looked up in the NASA/IPAC Extragalactic Database [1]. For eight of the galaxies in our sample,

Table 2.1. The Galaxy Sample

Object	D (Mpc)	$m - M$	Reference	Morphology	Host M_{B}	$E(B-V)$
IC 342	3.3 ± 0.3	27.58 ± 0.18	1	SAB(rs)cd	-23.99	0.480
M33 (NGC 598)	0.9 ± 0.1	24.65 ± 0.19	2	SA(s)cd	-19.05	0.036
NGC 247	3.4 ± 0.3	27.68 ± 0.20	2	SAB(s)d	-18.82	0.016
NGC 300	2.0 ± 0.3	26.48 ± 0.28	2	SA(s)d	-18.04	0.011
NGC 2403	3.1 ± 0.2	27.43 ± 0.15	3	SAB(s)cd	-19.14	0.034
NGC 2976	3.6 ± 0.1*	27.77 ± 0.07	4	SAc pec	-17.74	0.064
NGC 3621	7.3 ± 0.2	29.30 ± 0.06	3	SA(s)d	-20.38	0.068
NGC 4244	4.3 ± 0.1*	28.16 ± 0.07	4	SA(s)cd	-18.96	0.018
NGC 4395	4.3 ± 0.4	28.17 ± 0.18	5	SA(s)m	-17.66	0.015
NGC 7793	3.4 ± 0.1	27.68 ± 0.05	6	SA(s)d	-18.38	0.017

References. — Redshift-independent distances and distance moduli $(m - M)$ were obtained from the following: (1) Saha et al. (2002); (2) Bono et al. (2010); (3) Saha et al. (2006); (4) Jacobs et al. (2009); (5) Thim et al. (2004); (6) Pietrzyński et al. (2010). All distances were measured using Cepheid variables except those marked with an asterisk (*), which are TRGB distances. The $E(B-V)$ reddening due to Galactic dust for each galaxy is from Schlafly & Finkbeiner (2011).

the distances quoted were measured using Cepheid variables. We used tip of the red giant branch (TRGB) distances for NGC 2976 and NGC 4244, because Cepheid variable distances were not available.

2.2 Description of Observations

Each cluster was observed in seven filter bands over a total of two orbits. For each galaxy, a series of four exposures was taken in each filter band. These four exposures were offset by fractional-pixel shifts relative to each other using a four-point box dither pattern. The

[1]The NASA/IPAC Extragalactic Database (NED) is operated by the Jet Propulsion Laboratory, California Institute of Technology, under contract with the National Aeronautics and Space Administration.

final images were constructed by combining these exposures, which allowed for the removal of cosmic-ray hits and bad pixels.

In the UVIS channel, we used the F275W, F336W, F438W, F547M, and F814W filters. We used F547M instead of a wide-band filter for the V band because it does not include flux from the [O3], Hα, or Hβ emission lines. The UVIS channel CCD has a pixel scale of 004 pixel^{-1}. At a distance of 5 Mpc, a pixel on the UVIS CCD subtends 0.96 pc. The point spread functions (PSFs) range in full width at half maximum from 0092 in F275W to 0196 in F153M. These angular sizes correspond to physical sizes of 2.20 pc and 4.70 pc at a distance of 5 Mpc. Since NCs typically have effective radii of a few pc, WFC3 provides sufficient spatial resolution for studies of their structure. In order to observe each NC with several filters in just two orbits, it is necessary to reduce readout time and eliminate buffer dump overheads. To accomplish this, we used the MS512C subarray readout mode, which gives a $20'' \times 20''$ field of view. This field of view is more than wide enough to cover the entire NC and sample the region where the NC surface brightness profile merges with that of the host galaxy.

In the IR channel, we used two medium-band filters, F127M and F153M, to sample the J and H bands because the NCs are bright enough to saturate with very short exposure times ($<$ 10 seconds) using wide-band filters. The IR channel HgCdTe array has coarser resolution than the UVIS channel CCD, with a scale of 013 pixel^{-1}. The IRSUB256 subarray was used, giving a $35'' \times 31''$ field of view for the IR images. We used SPARS10 sampling sequences with NSAMP=10, with the exception of the two brightest NCs, IC 342 and M33, where RAPID readout mode was used to avoid saturation.

Throughput curves of the *HST*/WFC3 filters are shown in Figure 2.1. Table 2.2 lists the central wavelengths and band widths of the filters as well as the exposure times used. Shorter exposure times were used for the two galaxies with the brightest NCs, IC 342 and M33, in order to avoid saturation. Due to the shorter exposure times and RAPID sampling, the

Table 2.2. *HST*/WFC3 Filter Properties & Exposure Times

Filter	Channel	Central Wavelength (Å)	Band Width (Å)	Exp. Time (s)	IC 342 Exp. Time (s)	M33 Exp. Time (s)
F275W	UVIS	2710.2	164.51	4×380	4×130	4×130
F336W	UVIS	3354.8	158.44	4×290	4×55	4×55
F438W	UVIS	4326.5	197.30	4×115	4×35	4×42
F547M	UVIS	5447.4	206.22	4×95	4×25	4×90
F814W	UVIS	8029.5	663.33	4×75	4×15	4×40
F127M	IR	12740.0	249.55	4×60	8×5	8×5
F153M	IR	15322.0	378.94	4×60	8×5	8×5

Note. — The central wavelength listed is the "pivot wavelength", a source-independent measure of the characteristic wavelength of the filter, and the band width is the "passband rectangular width", the integral with respect to wavelength of the throughput across the filter passband divided by the maximum throughput, as defined in the WFC3 Instrument Handbook (Dressel, 2012).

sequence of 4 exposures was duplicated for the IR observations of IC 342 and M33.

We obtained the reddening $E(B-V)$ for each galaxy from the latest Galactic dust maps (Schlafly & Finkbeiner, 2011), and we calculated the extinction due to Galactic dust in each band for all of the galaxies in the sample using the PyRAF/STSDAS task `Calcphot` (Bushouse & Simon, 1994). We applied the appropriate reddening to an F star template spectrum using the Cardelli et al. (1989) reddening law. From simulated *HST*/WFC3 observations, we obtained the magnitudes of the reddened and unreddened template star in each band, and determined the extinction from the difference between the two. All absolute magnitudes listed in this paper have been corrected for Galactic extinction and are given in the Vega magnitude system. The conversion between magnitudes in the Vega system and magnitudes in the AB system ($m_{\mathrm{AB}} - m_{\mathrm{Vega}}$) is 1.50 mag in F275W, 1.18 mag in F336W, -0.15 mag in F438W, 0.42 in F814W, 0.96 in F127M, and 1.25 mag in F153M.

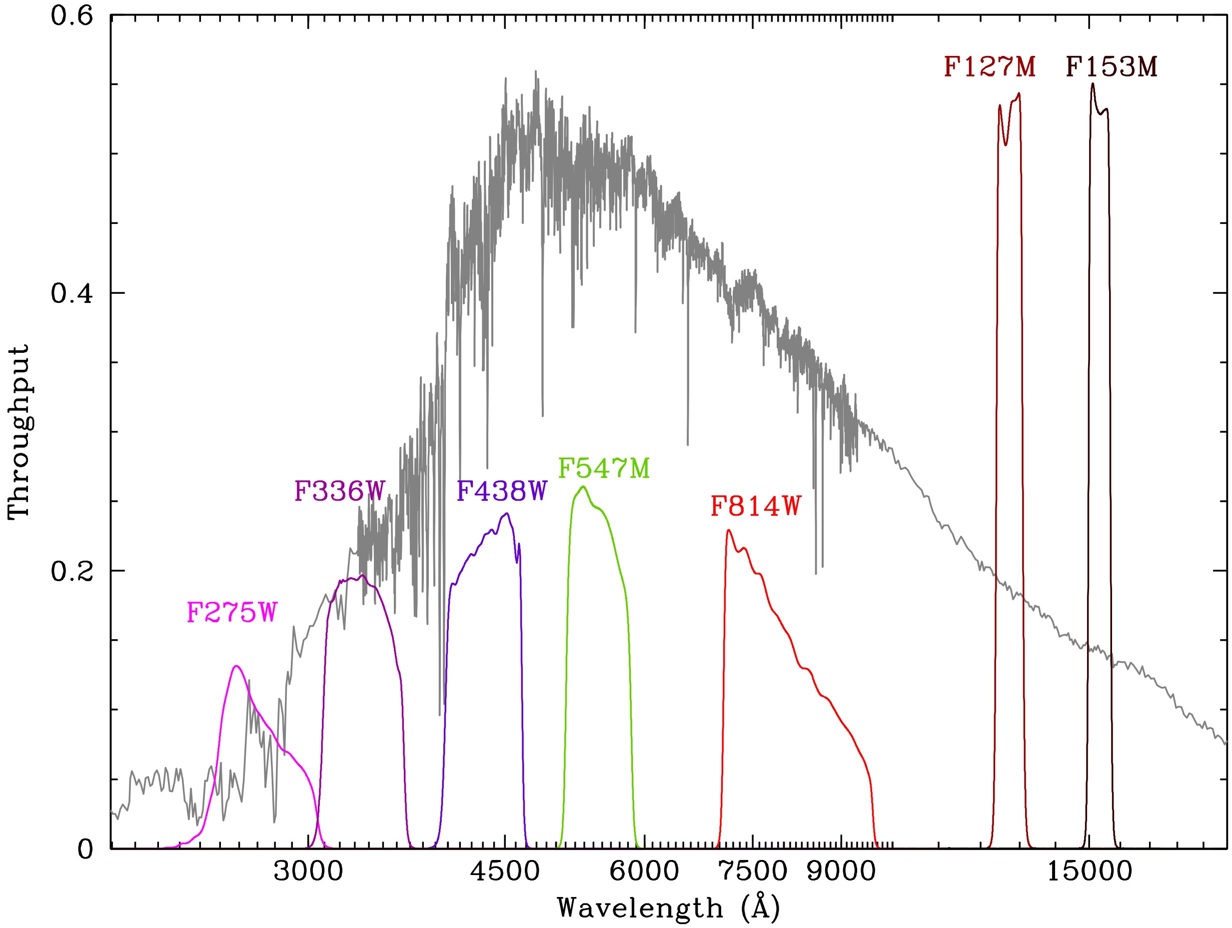

Figure 2.1 Throughput curves for the seven *HST*/WFC3 filters taken from the PyRAF/STSDAS task `Calcband`. Also shown in gray is a model spectrum of a 1.4 Gyr old stellar population with solar metallicity from Bruzual & Charlot (2003b).

2.3 Data Reduction

The standard *HST* calibration pipeline was used for flat fielding, bias correction and dark current subtraction. In order to reject cosmic-ray hits and bad pixels and to correct for the geometric distortion introduced by the optics of *HST* and WFC3, the four offset exposures for each filter were combined into a final image using the PyRAF/STSDAS task `AstroDrizzle`, using a square kernel with $pixfrac = 1$, exposure time weighting, and sky subtraction turned off. In addition, as part of the `AstroDrizzle` process, we resampled the IR images onto the UVIS grid for a uniform pixel size of 004 in all bands. The resulting images are shown in Figure 2.2. Color composite images of each cluster, along with images of their host galaxies, are shown in Figure 2.3.

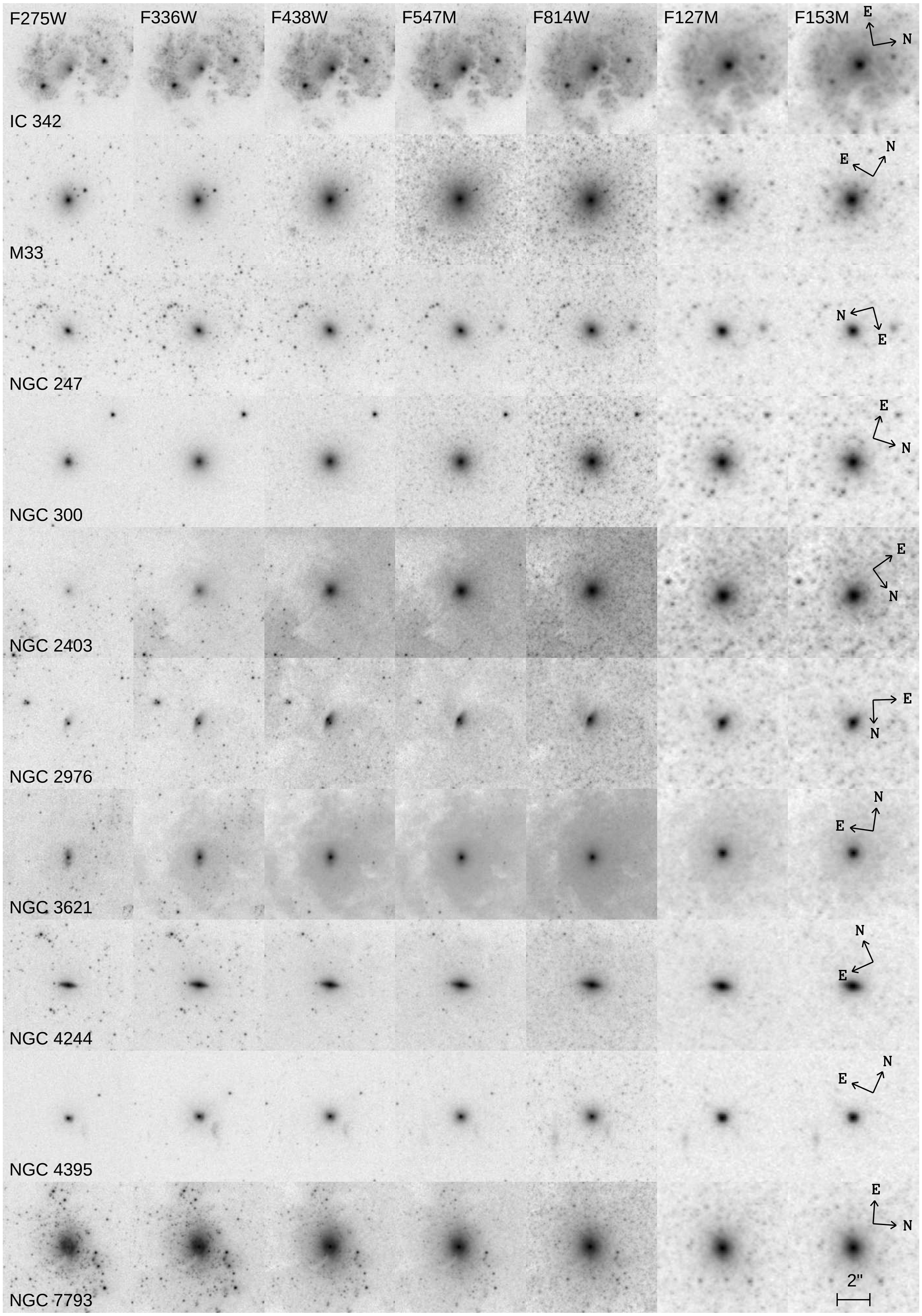

Figure 2.2 Inverted grayscale images of the inner $8'' \times 8''$ of each galaxy in all seven *HST*/WFC3 filters, shown with an asinh stretch. Images are displayed with their native orientation.

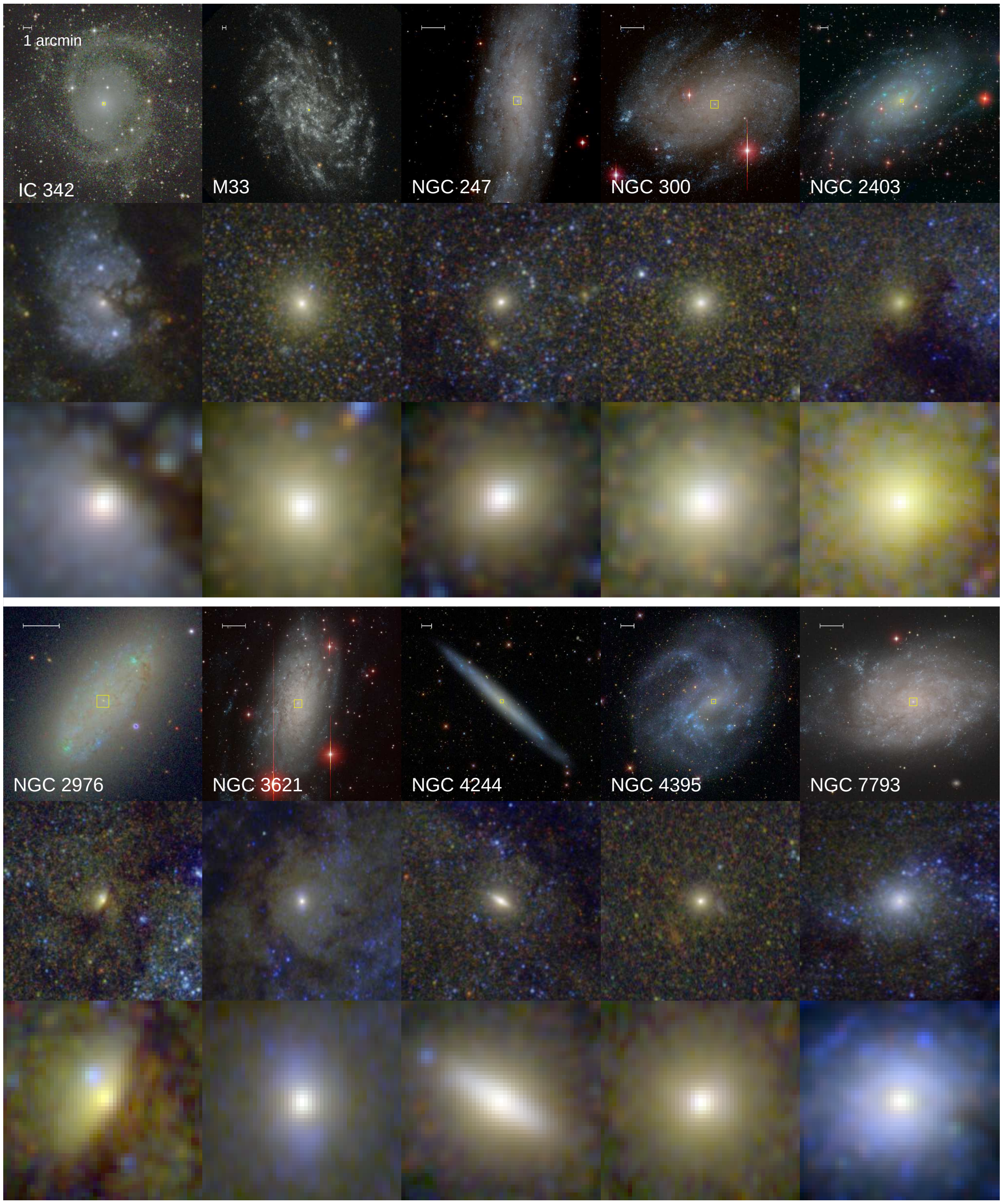

Figure 2.3 Color composite images of each NC and its host galaxy. For each object, the top panel shows the entire host galaxy, the middle panel shows the inner $12'' \times 12''$ of the galaxy, and the bottom panel shows the inner $2'' \times 2''$ centered on the NC. Host galaxy images were taken from the following sources: 2MASS (Skrutskie et al., 2006, IC 342), GALEX (Gil de Paz et al., 2007, M33), SDSS (Baillard et al., 2011, NGC 2403, NGC 2976, NGC 4244, and NGC 4395), and CGS (Ho et al., 2011, NGC 247, NGC 300, NGC 3621, and NGC 7793). For the NC images, the *HST*/WFC3 F275W, F547M, and F814W images were used to populate the blue, green and red color channels, respectively. The yellow boxes on the host galaxy images show the full $20'' \times 20''$ UVIS field of view and the scale bar denotes $1'$. All of the images have been rotated so that north is up and are shown with an asinh stretch.

Chapter 3

Analysis of Structural Properties

3.1 Surface Brightness Profile Fitting

A 2D model of the surface brightness profile was fit to each image using `GALFIT` version 3.0.4 (Peng et al., 2002, 2010). For each image, we specified the components of the model surface brightness profile to fit to the image (e.g., Sérsic, exponential) and supplied initial estimates for the model parameters (e.g., total magnitude, position of the center of the profile). A model image based on these parameters is produced and then convolved with the corresponding *HST*/WFC3 PSF. The χ^2 difference between the *HST* image and model image is computed, and minimization of χ^2 is achieved (and thus, best-fitting model parameters are found) using the Levenberg-Marquardt downhill-gradient method. To properly weight each pixel in the χ^2 calculation, we used the sigma image generated internally by GALFIT based on each input image.

We fit 2D surface brightness profiles to the images rather than fitting 1D radial profiles to elliptical isophotes of the images, because it allowed us to more accurately disentangle the instrumental PSF from the intrinsic profile of the clusters. The clusters are quite compact

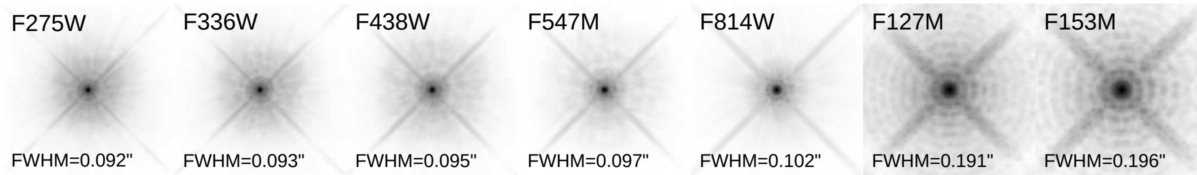

Figure 3.1 Model PSFs in each filter. The full width at half maximum of each PSF is given in arcseconds.

and the fits are therefore very sensitive to the details of the PSF profile. *HST*/WFC3 PSFs have non-axisymmetric features that cannot be described by a 1D radial profile. In addition, we find that some clusters have strongly non-axisymmetric features such as flattened disk components, which cannot be modeled accurately in 1D. PSF convolution in 1D is therefore not a suitable alternative to 2D convolution for the purpose of extracting the intrinsic 2D structure of the NCs from the *HST* images.

3.1.1 PSF Models

Simulated images of the *HST*/WFC3 PSFs in each filter were generated using version 7.4 of the `TinyTim` software package (Krist, 1993; Krist et al., 2011), which creates a model *HST* PSF based on the based on the instrument, detector chip, detector chip position, and filter used in the observations. To ensure that the model PSFs were processed in the same way as the *HST* images, we produced four versions of each PSF on a subsampled grid with sub-pixel offsets, using the same four-point box dither pattern as the *HST*/WFC3 exposures. Each model PSF was convolved with the appropriate charge diffusion kernel in order to account for the effect of electrons leaking into neighboring pixels on the CCD. The PSFs were then combined and resampled onto a final grid with a pixel size of 004 in all bands using `AstroDrizzle`, with the same settings that were used to combine the NC images. The resulting model PSFs are shown in Figure 3.1.

3.1.2 Fitting Method

The NCs sit at the center of their host galaxies, whose surface brightness profiles can generally be described by an exponential disk model because they have either a weak bulge component or no bulge component at all. The disk of the host galaxy contributes a significant amount of flux in our images, particularly in the outskirts of the NCs, and can have a strong effect on NC fit parameters such as the Sérsic index and effective radius. Our images have a small field of view and only sample the very inner regions of the galaxies. For example, the most distant galaxy in our sample, NGC 3621, has apparent angular dimensions $12' \times 7'$ (Gil de Paz et al., 2007), compared to the $20'' \times 20''$ UVIS field of view. Although the NCs sit against a non-uniform background, it is not always possible to detect a gradient in the background level across the image due to the small field of view. In order to model the host galaxy surface brightness profile, we masked out the NC as well as any prominent dust lanes and attempted to fit a model consisting of an exponential disk and a flat sky level to the host galaxy. If this fit converged, we performed the NC fit with the host galaxy exponential disk and sky parameters fixed at the best-fit values found in the previous step. We were only able to fit the host galaxy with an exponential disk and flat sky level using this method for IC 342, NGC 3621, and NGC 4244. For the rest of the sample, the scale length and total magnitude were flagged as a problematic parameters by `GALFIT`, indicating that the host galaxy profile is too flat across the image to be modeled by an exponential disk profile. For M33, NGC 247, NGC 300, NGC 2403, NGC 2976, NGC 4395 and NGC 7793, we used a flat sky level to model the host galaxy light and left its surface brightness as a free parameter when fitting the NC surface brightness profile.

For each fit, we used a 401×401 pixel ($16'' \times 16''$) fitting region centered on the brightest pixel in the NC. This fitting region size is quite large compared to the typical angular size of NCs in our sample, whose effective radii are all well under $1''$. We experimented with a range of different fitting region sizes to quantify the effect of the fitting region size on the fit results and find that these effects are at the 10 % level for the nuclear cluster properties. For a single Sérsic component fit with a flat sky level, increasing the size of the fitting region will lead to an increase in the brightness of the Sérsic component, an increase in the effective radius, an increase in the Sérsic index, and a decrease in the sky level. For example, when we performed a single Sérsic component fit to the F814W image of NGC 2403 using a 150×150 pixel fitting region, we obtained a magnitude of 15.48 mag, an effective radius of 10.00 pixels, and a Sérsic index of 1.51 for the NC component. When we performed the same fit using a 300×300 pixel fitting region, we obtained a magnitude of 15.41 mag, an effective radius of 10.82 pixels, and a Sérsic index of 1.64 for the NC component. In order to be able to compare fit results in different filters, it is important to use a consistent fitting region. In order to optimally sample the host galaxy light, we used the largest fitting region size that could be applied to every image while still excluding bad pixels on the edges of the image introduced during the image combination step of `AstroDrizzle`.

We experimented with different functions available in `GALFIT` to fit to the WFC3 images. Exponential, Gaussian, and de Vaucouleurs profiles are not flexible enough to describe the wide range of inner profile slopes seen in the NCs in our sample. Modified King (Elson, 1999), Nuker (Lauer et al., 1995) and Sérsic (1968) profiles all provided good fits to the F814W images of M33, NGC 300, and NGC 7793. These NCs have relatively simple structures and serve as instructive cases for comparison of different surface brightness models. In each case, the Sérsic profile results in the smallest χ^2, although the difference in χ^2 between fits performed using Sérsic and King profiles is always at the 10% level or less. The Nuker profile has five independent parameters and the King profile has four, while the Sérsic profile is described by only three independent parameters: the total magnitude, effective radius (half-light radius) and Sérsic index. We used a Sérsic profile to model the light profile of the NCs in our sample because the Sérsic profile provides the best flexibility in describing the structure of different NCs using the smallest number of free parameters. To allow for elliptical shapes we left the axis ratio (b/a, where b and a are the lengths of the semiminor and semimajor axes, respectively) and the position angle (PA) of the semimajor axis as free parameters in the fits.

With the exception of NGC 2976, NGC 4395 and NGC 4244, a single Sérsic profile was used to model each NC in every band. In the bands blueward of F814W, the structure of the NC in NGC 2976 is difficult to fit with any reasonable set of analytic models due to its small-scale clumpiness. This NC also contains a compact blue foreground component to the north (see Figure 2.3). For NGC 2976, we used aperture photometry to measure the total magnitude of the cluster and the magnitude of the blue component in F275W, F336W, and F438W, and F547M. Since the blue component becomes faint and the structure of the NC becomes smoother at longer wavelengths, we used `GALFIT` to fit a single Sérsic profile to the cluster in F814W, F127M and F153M. Seth et al. (2008b) found that the NC in NGC 4244 has two distinct morphological components: a red/old, compact, spheroidal structure, and a blue/young, extended disk structure, while studies by Filippenko & Sargent (1989) and Filippenko & Ho (2003) have shown that NGC 4395 hosts a NC as well as an unobscured AGN. Based on these studies, we modeled the NC in NGC 4244 using two Sérsic components, and for NGC 4395 we used a Sérsic component to model the NC and a point source component to model the AGN. For comparison to the rest of the sample, we also performed single Sérsic component fits to the NGC 4244 and NGC 4395 images. A more detailed discussion of individual objects is given in Section 3.3. Figure 3.2 shows the results of the fits to the F814W images for each NC.

3.1.3 Comparison with `ISHAPE`

Georgiev & Böker (2014) used the `ISHAPE` procedure in the `BAOLAB` software package (Larsen, 1999) to measure effective radii, axis ratios, and magnitudes of a sample of 228 NCs in late-type spiral galaxies using images from the *HST*/WFPC2 archive. Much like `GALFIT`, `ISHAPE` measures structural properties by minimizing the χ^2 difference between an image and a PSF convolved model, but it performs the fit over a circular, rather than a rectangular fitting region. In their study, the NCs were modeled using single component King and power-law models and the *HST*/WFPC2 model PSFs were generated using `TinyTim`. However, they did not allow for the possibility of an exponential disk profile to model the host galaxy light. The substructure seen in some of the clusters in our sample would not be easily detected at the distances typical of NCs in their sample, which was selected using a distance cut of 40 Mpc. As a test, we used `ISHAPE` to fit single Sérsic component models to our F814W images using a 200 pixel fitting radius and found very good agreement with our `GALFIT` results. The mean offset between magnitudes measured using `ISHAPE` and magnitudes measured using `GALFIT` (i.e., $|m_{\rm GALFIT} - m_{\rm ISHAPE}|$) was 0.05 mag, while on average, the effective radii and Sérsic indices agreed within 11% and 24%, respectively.

3.1.4 1D Radial Profiles

The "goodness of fit" is easy to visualize in a 1D radial profile plot, although non-axisymmetric features of the surface brightness profiles are lost in this representation. We fit elliptical isophotes (ellipses of constant surface brightness) to both the *HST*/WFC3 images and the PSF-convolved `GALFIT` models using the PyRAF/STSDAS routine `Ellipse` (Freudling, 1993), which is based on methods detailed by Jedrzejewski (1987). For each isophote, this routine computes the semimajor axis (SMA) of the ellipse, as well as the isophote surface brightness and ellipticity ($e = 1 - b/a$, where b/a is the axis ratio). We also performed isophotal fits to the model PSFs in order to display their radial surface brightness profiles. Plots of the F814W radial profiles of the surface brightness and ellipticity for each cluster are shown in Figure 3.6. In every case the PSF-convolved `GALFIT` models are significantly more extended than the PSF and the cluster effective radius exceeds the radius which encloses half of the flux of the F814W PSF (0063), indicating that all of the NCs in our sample are

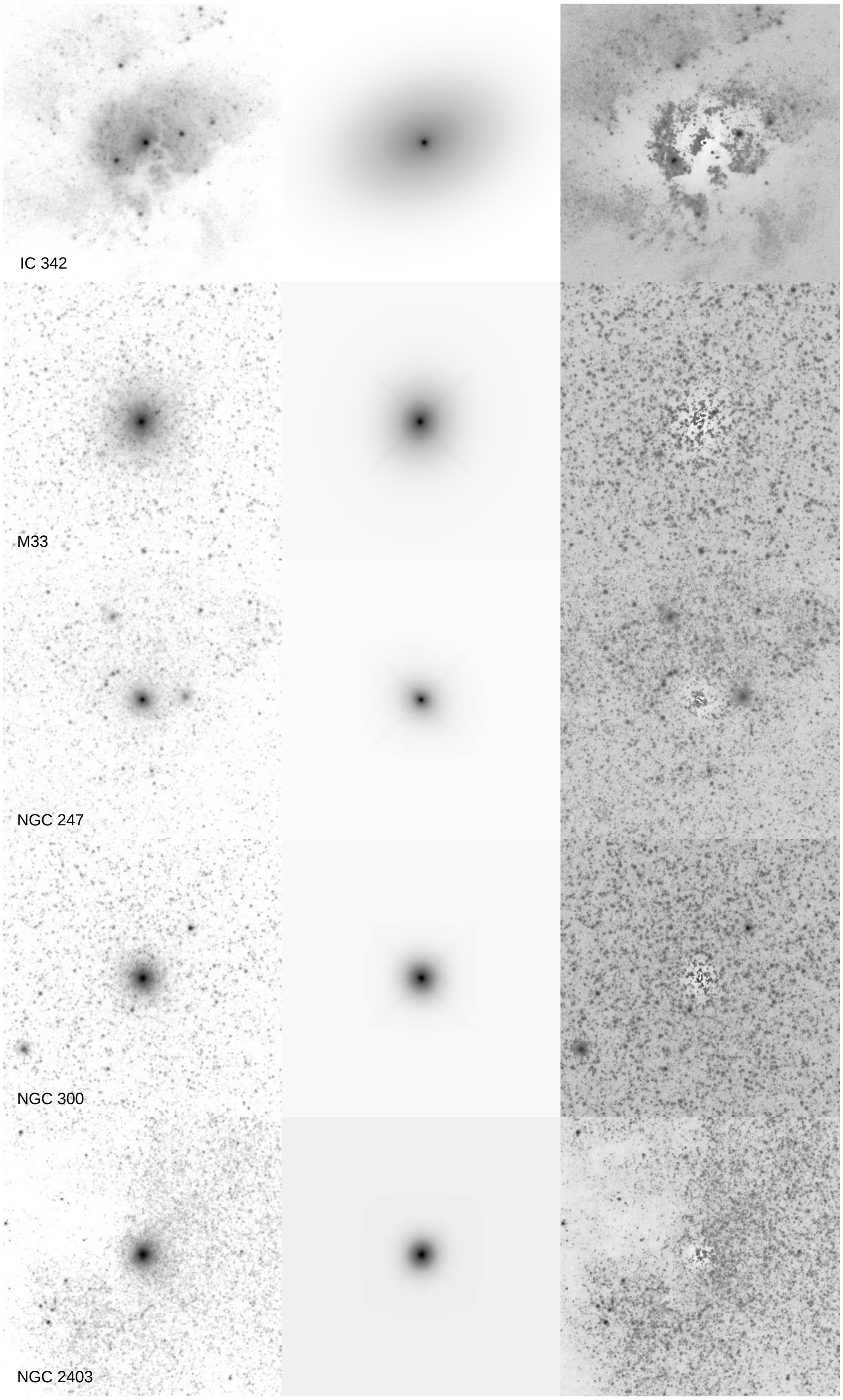

Figure 3.2 Results of the F814W fits. The panels (from left to right) show the F814W image, the best-fit model convolved with the PSF, and the residuals (*image* − *model*). The field of view is $16'' \times 16''$ for all fits. Images are displayed with their native orientation, as in Figure 2.2.

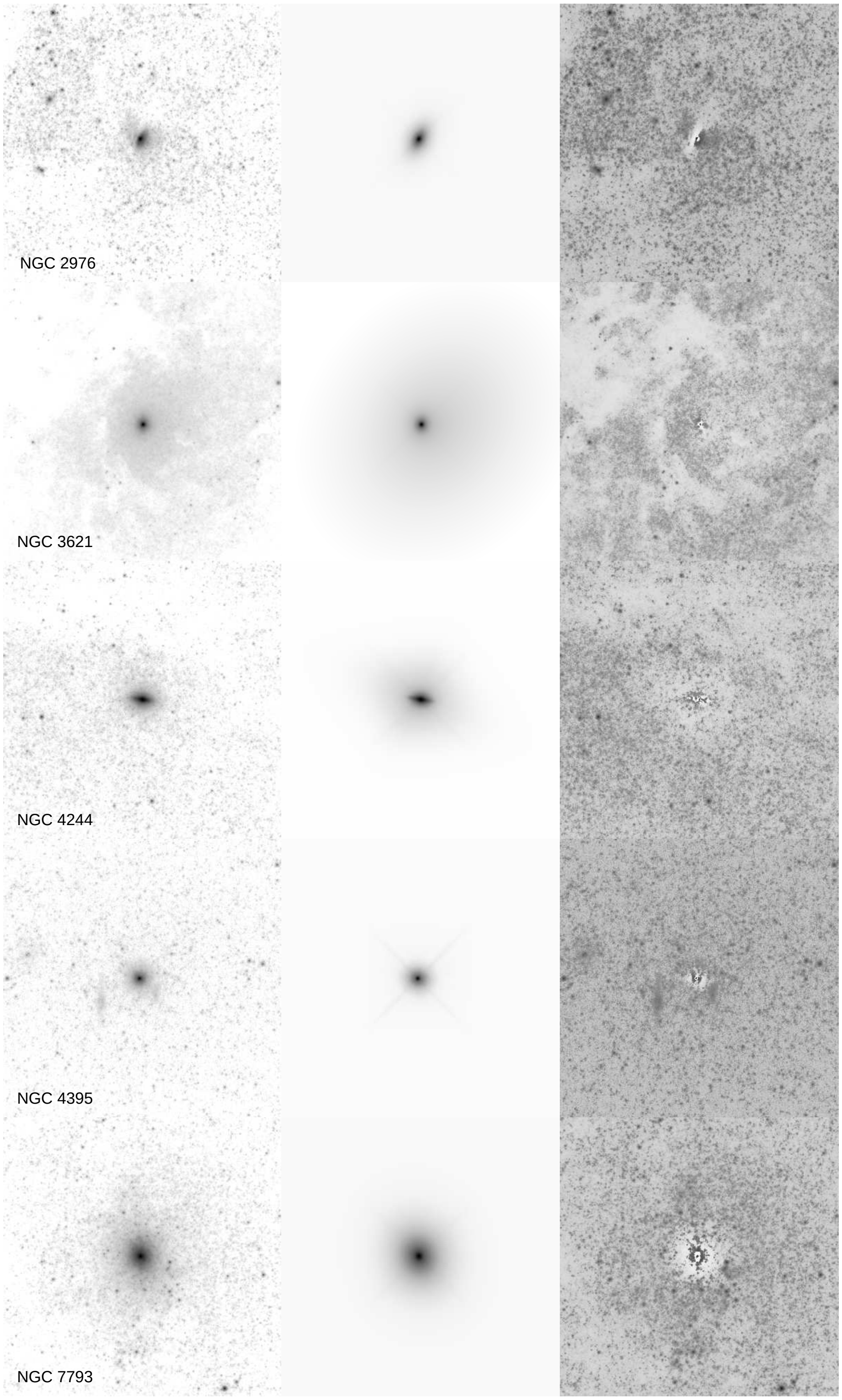

Figure 3.5 Results of the fits in F814W (continued).

spatially resolved.

3.1.5 Uncertainties in Cluster Parameters

Because the data have very high S/N, the formal `GALFIT` measurement uncertainties in the best-fit parameters obtained from propagating the uncertainty in electron counts at each pixel are quite small. Our error budget is dominated by uncertainties that arise due to the degeneracy between the NC and the background light of the host galaxy light, which we model in `GALFIT` using either a flat sky level or the combination of a flat sky level and an exponential disk. Estimates of the uncertainties of the best-fit parameters should therefore reflect how sensitive these parameters are to variations in the background level. In general, there is no unambiguous way to define a boundary between the NC and the underlying background light from the disk of the host galaxy. In addition, the background can be quite non-uniform and lumpy, due to the presence of resolved stars, off-nuclear clusters, and patchy dust lanes in the immediate vicinity of the NC.

The formal uncertainty on the sky parameter returned by `GALFIT` is typically small (< 0.1 ADU), and does not reflect the true uncertainty resulting from the lumpy nature of the immediate surroundings of the NC. In order to more realistically estimate the uncertainty in the sky parameter ($\sigma_{\rm sky}$), we took the 401×401 pixel section of each image that was used in the fit, and divided it into eight equally sized wedges, by splitting it into quadrants along the vertical and horizontal axes of the image, and then splitting each quadrant in half at a $45°$ angle with respect to the vertical and horizontal axes. We found the mean sky level in each wedge while masking the NC and computed the standard deviation of these values, to obtain $\sigma_{\rm sky}$. This uncertainty (typically a few ADU), is much larger than the formal uncertainty on the sky parameter returned by `GALFIT`. We used the mean sky level in this calculation, as opposed to the mode sky, because the mean sky is a better representation

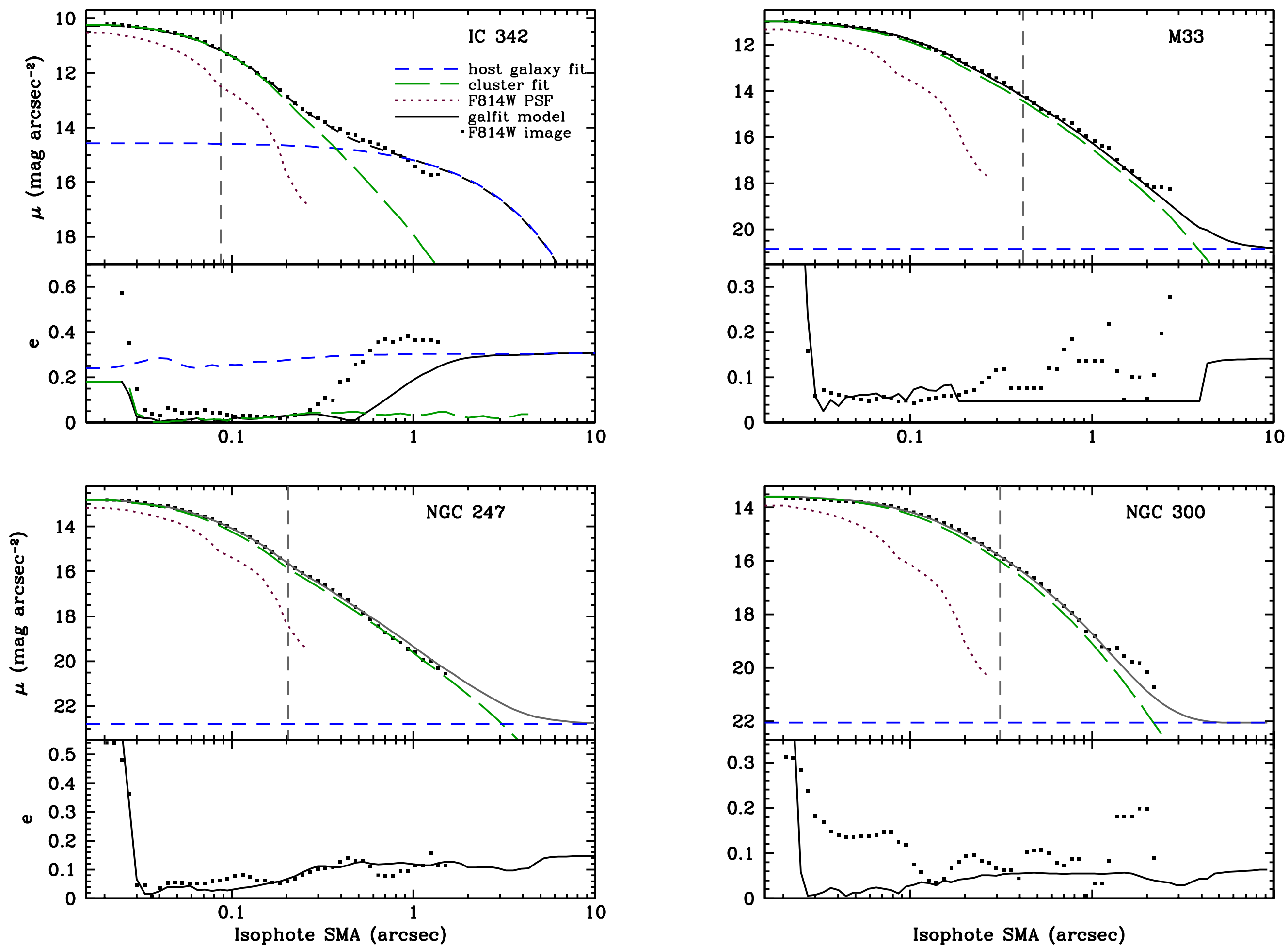

Figure 3.6 F814W radial profiles of the surface brightness and ellipticity of the GALFIT model (solid black line) and *HST*/WFC3 image (black squares) as a function of SMA, as well as the subcomponents of the fit. These radial profiles were obtained using the elliptical isophote fitting routine Ellipse. The host galaxy model light profile is denoted by a blue dashed line, and the NC model light profile is denoted by a green long-dashed line. For reference, we include a radial profile of the F814W PSF, indicated by a red dotted line. The vertical gray long-dashed line shows the effective radius of the NC. The convolved NC radial profiles are significantly more extended than the PSF, demonstrating that the clusters are spatially resolved in each case.

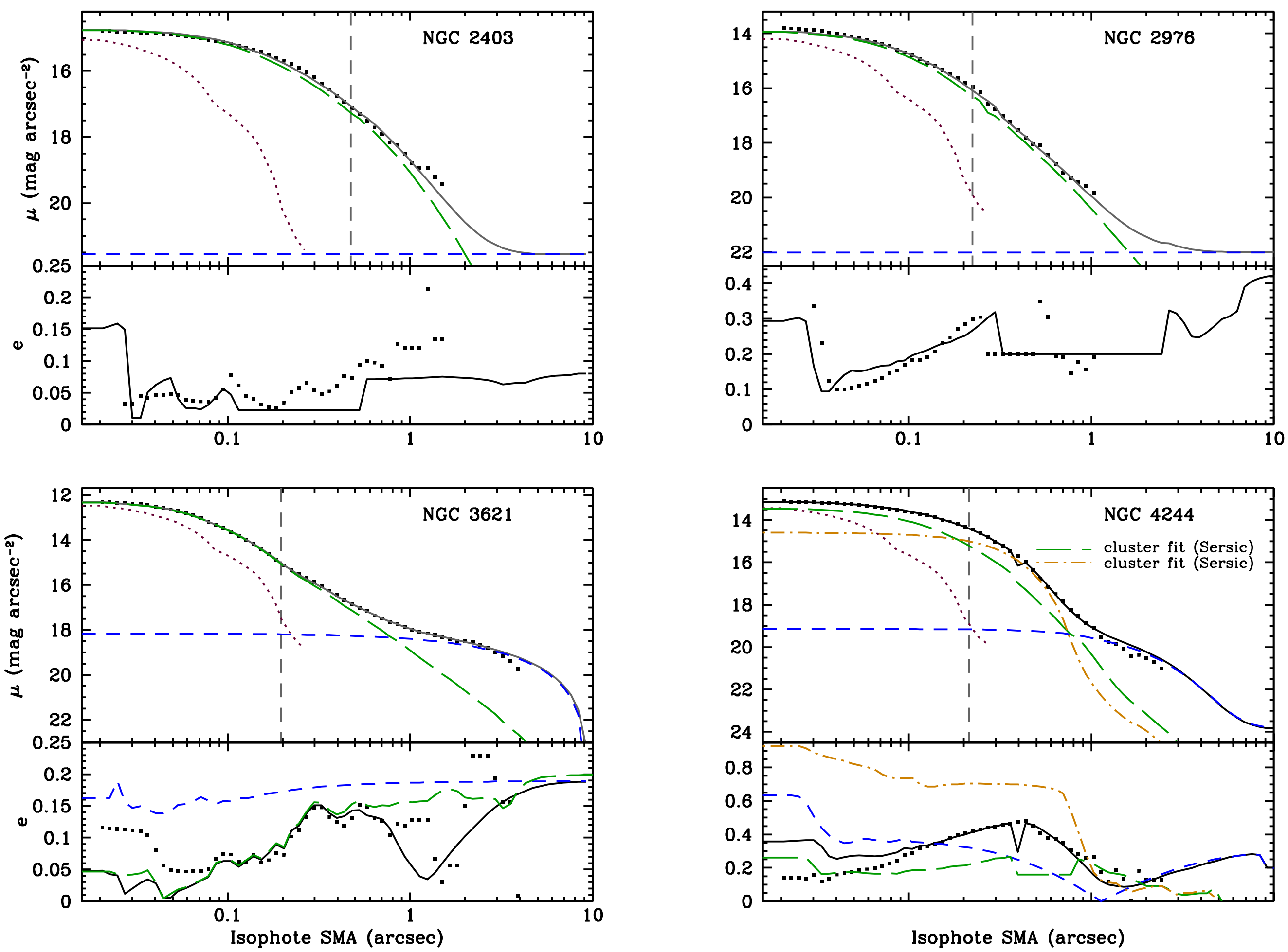

Figure 3.6 F814W radial profile plots (continued). NGC 4244 is fit with 2 Sérsic components, which are indicated by a green long-dashed line and an orange dash-dotted line.

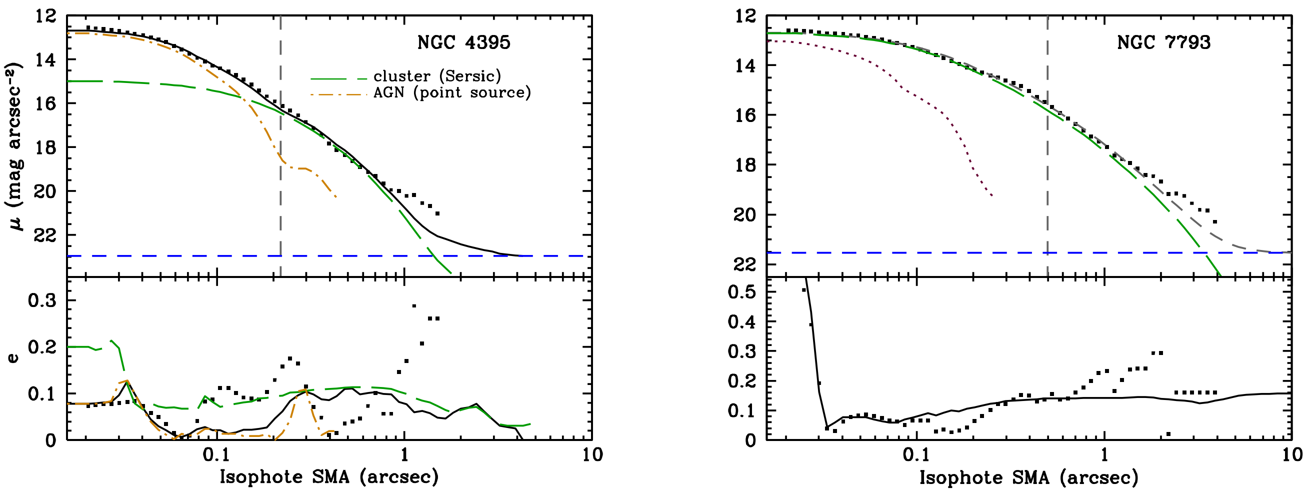

Figure 3.6 F814W radial profile plots (continued). NGC 4395 is fit with a Sérsic component (indicated by a green long-dashed line) and a point source component (orange dash-dotted line), and the vertical gray long-dashed line denotes the effective radius of the Sérsic component of this two component fit. We do not include an additional PSF for reference in this plot because the point source is included a fit component.

of the surface brightness of the host galaxy, which includes resolved sources, such as bright stars and off-nuclear clusters. Using the mode sky would underestimate the host galaxy surface brightness by excluding the contribution of individual resolved stars.

For fits where a flat sky level was used to model the background light from the host galaxy, the corresponding uncertainties in the NC best-fit parameters were estimated by re-running `GALFIT` while holding the sky parameter fixed at $sky - \sigma_{\rm sky}$ (where sky is the best-fit sky parameter from the original fit), and again with the sky parameter fixed at $sky + \sigma_{\rm sky}$. For fits where a combination of a flat sky level and exponential disk were used to model the host galaxy, we re-ran the host galaxy fit as explained in Section 3.1.2, but held the sky parameter fixed at $sky - \sigma_{\rm sky}$, and again with the sky parameter fixed at $sky + \sigma_{\rm sky}$. We then performed the NC fit with the host galaxy exponential disk and sky parameters fixed at the best-fit values found in the previous step to find the upper and lower uncertainties in the NC best-fit parameters. These uncertainties were added in quadrature to the formal measurement uncertainties computed by `GALFIT` in order to produce the total uncertainty on each fit parameter.

The uncertainty on the distance to each galaxy is an additional source of systematic uncertainty that affects absolute magnitudes in different bands in the same way. In order for the uncertainties that we quote to reflect only our own analysis, we did not include the uncertainty on the distance modulus in the error budget for absolute magnitudes. However, interested readers can refer to the uncertainties on distance moduli quoted in Table 2.1.

3.2 Results

3.2.1 Single Band Results

Structural Properties

The NCs in our sample have a wide range of structural properties. From single Sérsic component fits, we find that F814W absolute magnitudes range from −11.20 mag to −15.05 mag with a mean of −12.56 mag, effective radii range from 1.38 to 8.28 pc with a mean of 4.27 pc, Sérsic indices range from 1.63 to 9.73 with a mean of 3.93, and axis ratios range from 0.57 to 0.94 with a mean of 0.83. The best-fit parameters in each band are shown in Table 3.1. We also include the extinction along the line of sight to each galaxy in this table. To help visualize the properties of the sample as a whole, we constructed histograms of the best-fit absolute magnitudes, effective radii, Sérsic indices, and axis ratios for the single Sérsic component fits in each band, which are shown in Figure 3.7.

We measure a much wider range of best-fit Sérsic indices than in previous studies, including some very large values ($n > 8$). For the small number of NCs for which a measurement of the Sérsic index has been performed, previous studies have generally found $n \sim 1$–3 (Graham & Spitler, 2009; Seth et al., 2010). In order to investigate the robustness of these high concentrations, we used `GALFIT` to produce noise-free Sérsic models with an effective radius of 023 (which is the mean value for our sample) and Sérsic indices ranging from 0.5 to 10, all which were convolved with the F547M PSF. We show their radial surface brightness profiles, along with radial profiles of the corresponding intrinsic Sérsic models (which have not been convolved with the PSF) in Figure 3.8. The large values of the Sérsic index that we measure are determined more by the behavior of the profile in the wings than in the core, because the PSF blurs out information about the slope of the inner profile. For radii inside the half width at half maximum of the PSF, the profiles for $n > 6$ are not distinguishable. However, these profiles are strongly divergent at radii outside of the core of the PSF. Therefore, the large Sérsic indices that are seen in some objects serve as useful indicators of the shape of the NC profile outside of the core of the PSF. We conclude that NCs have a wide range of concentrations as indicated by the wide range of Sérsic indices, and that Sérsic indices above 6 do not indicate differences in core concentrations, but instead are dependent on the wings of the profile.

Table 3.1: Best-fit surface brightness profile parameters and their corresponding uncertainties. We include the extinction in each band (A) along the line of sight to each galaxy. Some axis ratios have very small uncertainties, which round to 0.00. We list an uncertainty of 0.01 in these cases. Best-fit parameters for all 10 NCs are available in the online version of the table. For NGC 4244, we list the best-fit parameters for each Sérsic component separately. For NGC 4395, we list the best-fit parameters for the Sérsic component and the point source component separately.

		F275W	F336W	F438W	F547M	F814W	F127M	F153M
IC 342	A (mag)	2.94	2.44	2.00	1.51	0.90	0.41	0.30
	m (mag)	$17.25^{+0.25}_{-0.08}$	$16.21^{+0.10}_{-0.23}$	$15.99^{+0.08}_{-0.17}$	$15.01^{+0.07}_{-0.14}$	$13.43^{+0.06}_{-0.08}$	$11.71^{+0.05}_{-0.10}$	$11.14^{+0.06}_{-0.10}$
	M (mag)	$-13.27^{+0.25}_{-0.08}$	$-13.80^{+0.10}_{-0.23}$	$-13.59^{+0.08}_{-0.17}$	$-14.07^{+0.07}_{-0.14}$	$-15.05^{+0.06}_{-0.08}$	$-16.27^{+0.05}_{-0.10}$	$-16.74^{+0.06}_{-0.10}$
	$R_{\rm eff}$ (pc)	$1.42^{+0.48}_{-0.12}$	$1.38^{+0.48}_{-0.16}$	$1.41^{+0.38}_{-0.13}$	$1.42^{+0.33}_{-0.14}$	$1.38^{+0.19}_{-0.13}$	$1.40^{+0.20}_{-0.09}$	$1.40^{+0.20}_{-0.09}$
	n	$1.03^{+0.63}_{-0.63}$	$1.94^{+0.95}_{-0.50}$	$2.56^{+0.88}_{-0.36}$	$2.97^{+0.78}_{-0.36}$	$3.79^{+0.48}_{-0.40}$	$2.47^{+0.73}_{-0.32}$	$2.49^{+0.69}_{-0.32}$
	b/a	$0.98^{+0.02}_{-0.01}$	$0.84^{+0.07}_{-0.07}$	$0.89^{+0.02}_{-0.01}$	$0.92^{+0.02}_{-0.01}$	$0.94^{+0.01}_{-0.01}$	$0.91^{+0.01}_{-0.01}$	$0.92^{+0.01}_{-0.01}$
M33	A (mag)	0.22	0.18	0.15	0.11	0.07	0.03	0.02
	m (mag)	$14.97^{+0.07}_{-0.14}$	$14.47^{+0.06}_{-0.10}$	$14.55^{+0.03}_{-0.03}$	$13.84^{+0.04}_{-0.03}$	$12.88^{+0.04}_{-0.04}$	$11.95^{+0.05}_{-0.07}$	$11.53^{+0.05}_{-0.06}$
	M (mag)	$-9.89^{+0.07}_{-0.14}$	$-10.36^{+0.06}_{-0.10}$	$-10.25^{+0.03}_{-0.03}$	$-10.92^{+0.04}_{-0.03}$	$-11.84^{+0.04}_{-0.04}$	$-12.73^{+0.05}_{-0.07}$	$-13.14^{+0.05}_{-0.06}$
	$R_{\rm eff}$ (pc)	$0.69^{+0.29}_{-0.10}$	$1.25^{+0.31}_{-0.16}$	$1.39^{+0.06}_{-0.06}$	$1.57^{+0.09}_{-0.10}$	$1.72^{+0.12}_{-0.13}$	$1.73^{+0.22}_{-0.14}$	$1.78^{+0.20}_{-0.13}$
	n	$7.08^{+2.66}_{-1.15}$	$6.11^{+1.13}_{-0.70}$	$4.07^{+0.19}_{-0.19}$	$4.01^{+0.20}_{-0.24}$	$3.93^{+0.24}_{-0.27}$	$3.64^{+0.47}_{-0.32}$	$3.81^{+0.43}_{-0.31}$
	b/a	$0.79^{+0.01}_{-0.01}$	$0.84^{+0.01}_{-0.01}$	$0.82^{+0.01}_{-0.01}$	$0.85^{+0.01}_{-0.01}$	$0.86^{+0.01}_{-0.01}$	$0.86^{+0.01}_{-0.01}$	$0.85^{+0.01}_{-0.01}$

NGC 247	A (mag)	0.10	0.08	0.06	0.05	0.03	0.01	0.01
	m (mag)	$17.03^{+0.01}_{-0.02}$	$16.80^{+0.06}_{-0.05}$	$17.00^{+0.09}_{-0.13}$	$16.52^{+0.07}_{-0.19}$	$15.66^{+0.12}_{-0.12}$	$15.13^{+0.08}_{-0.22}$	$14.66^{+0.13}_{-0.18}$
	M (mag)	$-10.75^{+0.01}_{-0.02}$	$-10.96^{+0.06}_{-0.05}$	$-10.75^{+0.09}_{-0.13}$	$-11.21^{+0.07}_{-0.19}$	$-12.05^{+0.12}_{-0.12}$	$-12.57^{+0.08}_{-0.22}$	$-13.04^{+0.13}_{-0.18}$
	$R_{\rm eff}$ (pc)	$0.79^{+0.07}_{-0.07}$	$1.12^{+0.10}_{-0.09}$	$1.75^{+0.58}_{-0.26}$	$2.44^{+1.39}_{-0.33}$	$3.41^{+1.18}_{-0.78}$	$3.41^{+1.88}_{-0.39}$	$3.49^{+1.80}_{-0.69}$
	n	$2.98^{+0.40}_{-0.30}$	$7.00^{+1.01}_{-1.57}$	$8.29^{+3.38}_{-1.93}$	$6.49^{+3.55}_{-1.18}$	$8.29^{+2.11}_{-1.85}$	$3.91^{+3.02}_{-0.89}$	$5.92^{+2.08}_{-1.92}$
	b/a	$0.55^{+0.01}_{-0.01}$	$0.67^{+0.01}_{-0.01}$	$0.73^{+0.01}_{-0.01}$	$0.76^{+0.01}_{-0.01}$	$0.85^{+0.01}_{-0.01}$	$0.87^{+0.01}_{-0.01}$	$0.89^{+0.01}_{-0.01}$
NGC 300	A (mag)	0.07	0.06	0.05	0.03	0.06	0.01	0.01
	m (mag)	$17.62^{+0.01}_{-0.01}$	$16.95^{+0.02}_{-0.03}$	$17.00^{+0.02}_{-0.02}$	$16.27^{+0.02}_{-0.02}$	$15.34^{+0.02}_{-0.02}$	$14.49^{+0.04}_{-0.05}$	$14.10^{+0.04}_{-0.05}$
	M (mag)	$-8.93^{+0.01}_{-0.01}$	$-9.59^{+0.02}_{-0.03}$	$-9.53^{+0.02}_{-0.02}$	$-10.25^{+0.02}_{-0.02}$	$-11.20^{+0.02}_{-0.02}$	$-12.00^{+0.04}_{-0.05}$	$-12.39^{+0.04}_{-0.05}$
	$R_{\rm eff}$ (pc)	$1.52^{+0.03}_{-0.03}$	$2.36^{+0.10}_{-0.08}$	$2.60^{+0.09}_{-0.07}$	$2.86^{+0.09}_{-0.08}$	$2.99^{+0.10}_{-0.09}$	$3.11^{+0.23}_{-0.15}$	$3.12^{+0.25}_{-0.16}$
	n	$2.32^{+0.09}_{-0.08}$	$2.66^{+0.16}_{-0.13}$	$2.41^{+0.12}_{-0.10}$	$2.25^{+0.10}_{-0.08}$	$2.27^{+0.10}_{-0.08}$	$2.56^{+0.29}_{-0.20}$	$2.65^{+0.33}_{-0.22}$
	b/a	$0.85^{+0.01}_{-0.01}$	$0.91^{+0.01}_{-0.01}$	$0.92^{+0.01}_{-0.01}$	$0.93^{+0.01}_{-0.01}$	$0.94^{+0.01}_{-0.01}$	$0.93^{+0.01}_{-0.01}$	$0.93^{+0.01}_{-0.01}$
NGC 2403	A (mag)	0.21	0.17	0.14	0.11	0.06	0.03	0.02
	m (mag)	$20.24^{+0.20}_{-0.55}$	$18.48^{+0.13}_{-0.29}$	$18.27^{+0.11}_{-0.19}$	$17.18^{+0.10}_{-0.16}$	$15.87^{+0.11}_{-0.10}$	$14.70^{+0.14}_{-0.29}$	$14.21^{+0.15}_{-0.27}$
	M (mag)	$-7.40^{+0.20}_{-0.55}$	$-9.12^{+0.13}_{-0.29}$	$-9.31^{+0.11}_{-0.19}$	$-10.35^{+0.10}_{-0.16}$	$-11.62^{+0.11}_{-0.10}$	$-12.76^{+0.14}_{-0.29}$	$-13.24^{+0.15}_{-0.27}$
	$R_{\rm eff}$ (pc)	$3.57^{+5.08}_{-0.90}$	$6.63^{+2.19}_{-0.88}$	$5.89^{+1.51}_{-0.62}$	$5.93^{+1.26}_{-0.59}$	$6.13^{+0.76}_{-0.68}$	$7.08^{+3.50}_{-1.09}$	$7.29^{+3.28}_{-1.23}$
	n	$3.69^{+2.76}_{-0.87}$	$2.07^{+0.78}_{-0.21}$	$1.55^{+0.43}_{-0.19}$	$1.58^{+0.36}_{-0.18}$	$1.63^{+0.18}_{-0.22}$	$1.99^{+0.93}_{-0.37}$	$2.12^{+0.90}_{-0.43}$
	b/a	$0.87^{+0.06}_{-0.06}$	$0.89^{+0.04}_{-0.04}$	$0.90^{+0.01}_{-0.01}$	$0.92^{+0.01}_{-0.01}$	$0.92^{+0.01}_{-0.01}$	$0.93^{+0.01}_{-0.01}$	$0.92^{+0.01}_{-0.01}$
NGC 2976	A (mag)	0.40	0.33	0.27	0.20	0.12	0.05	0.04

	m (mag)	$19.06^{+0.10}_{-0.10}$	$18.67^{+0.10}_{-0.10}$	$18.91^{+0.10}_{-0.10}$	$18.00^{+0.10}_{-0.10}$	$16.53^{+0.08}_{-0.24}$	$15.21^{+0.09}_{-0.34}$	$14.70^{+0.10}_{-0.42}$
	M (mag)	$\cdots$	$\cdots$	$\cdots$	$\cdots$	$-11.36^{+0.08}_{-0.24}$	$-12.61^{+0.09}_{-0.34}$	$-13.11^{+0.10}_{-0.42}$
	$R_{\rm eff}$ (pc)	$\cdots$	$\cdots$	$\cdots$	$\cdots$	$3.87^{+2.13}_{-0.48}$	$3.69^{+4.02}_{-0.49}$	$3.70^{+6.30}_{-0.56}$
	n	$\cdots$	$\cdots$	$\cdots$	$\cdots$	$3.64^{+1.95}_{-0.57}$	$4.66^{+5.03}_{-1.07}$	$5.26^{+7.21}_{-1.36}$
	b/a	$\cdots$	$\cdots$	$\cdots$	$\cdots$	$0.57^{+0.01}_{-0.01}$	$0.67^{+0.03}_{-0.01}$	$0.69^{+0.03}_{-0.01}$
NGC 3621	A (mag)	0.42	0.35	0.28	0.21	0.13	0.06	0.04
	m (mag)	$18.52^{+0.19}_{-0.19}$	$17.18^{+0.04}_{-0.02}$	$17.04^{+0.14}_{-0.06}$	$16.24^{+0.17}_{-0.07}$	$15.18^{+0.13}_{-0.07}$	$14.11^{+0.04}_{-0.06}$	$13.68^{+0.05}_{-0.04}$
	M (mag)	$-11.20^{+0.19}_{-0.19}$	$-12.46^{+0.04}_{-0.02}$	$-12.54^{+0.14}_{-0.06}$	$-13.27^{+0.17}_{-0.07}$	$-14.25^{+0.13}_{-0.07}$	$-15.25^{+0.04}_{-0.06}$	$-15.66^{+0.05}_{-0.04}$
	$R_{\rm eff}$ (pc)	$17.27^{+3.83}_{-3.83}$	$25.95^{+0.92}_{-2.26}$	$17.02^{+0.29}_{-4.14}$	$11.02^{+1.98}_{-3.54}$	$6.88^{+1.38}_{-1.84}$	$6.57^{+0.99}_{-0.56}$	$6.15^{+0.72}_{-0.72}$
	n	$3.22^{+0.53}_{-0.53}$	$7.62^{+0.18}_{-0.18}$	$8.00^{+0.47}_{-0.92}$	$8.99^{+0.71}_{-1.62}$	$9.73^{+1.00}_{-1.67}$	$8.77^{+0.95}_{-0.56}$	$9.63^{+0.75}_{-0.84}$
	b/a	$0.48^{+0.01}_{-0.01}$	$0.63^{+0.01}_{-0.01}$	$0.71^{+0.22}_{-0.01}$	$0.77^{+0.01}_{-0.01}$	$0.80^{+0.01}_{-0.01}$	$0.92^{+0.01}_{-0.01}$	$0.93^{+0.01}_{-0.01}$
NGC 4244	A (mag)	0.11	0.09	0.07	0.06	0.03	0.02	0.01
	m (mag)	$18.54^{+0.06}_{-0.06}$	$18.00^{+0.22}_{-0.04}$	$17.93^{+0.09}_{-0.03}$	$17.08^{+0.04}_{-0.04}$	$16.00^{+0.05}_{-0.05}$	$15.39^{+0.08}_{-0.02}$	$15.17^{+0.03}_{-0.03}$
	M (mag)	$-9.73^{+0.06}_{-0.06}$	$-10.26^{+0.22}_{-0.04}$	$-10.31^{+0.09}_{-0.03}$	$-11.14^{+0.04}_{-0.04}$	$-12.19^{+0.05}_{-0.05}$	$-12.79^{+0.08}_{-0.02}$	$-13.01^{+0.03}_{-0.03}$
	$R_{\rm eff}$ (pc)	$2.59^{+0.33}_{-0.33}$	$3.01^{+0.59}_{-0.58}$	$3.02^{+0.90}_{-0.21}$	$3.39^{+0.74}_{-0.20}$	$3.53^{+0.42}_{-0.31}$	$5.57^{+0.17}_{-0.17}$	$5.87^{+0.14}_{-0.16}$
	n	$3.46^{+0.69}_{-0.69}$	$2.33^{+1.12}_{-0.37}$	$1.66^{+1.42}_{-0.08}$	$1.73^{+1.12}_{-0.19}$	$1.71^{+0.61}_{-0.20}$	$2.71^{+0.06}_{-0.05}$	$2.38^{+0.14}_{-0.09}$
	b/a	$0.62^{+0.02}_{-0.05}$	$0.68^{+0.05}_{-0.05}$	$0.69^{+0.05}_{-0.05}$	$0.69^{+0.08}_{-0.02}$	$0.67^{+0.06}_{-0.01}$	$0.78^{+0.02}_{-0.01}$	$0.79^{+0.01}_{-0.01}$
	m (mag)	$17.81^{+0.02}_{-0.02}$	$17.60^{+0.07}_{-0.07}$	$17.93^{+0.11}_{-0.11}$	$17.48^{+0.04}_{-0.25}$	$16.73^{+0.02}_{-0.22}$	$15.20^{+0.04}_{-0.04}$	$14.66^{+0.02}_{-0.02}$
	M (mag)	$-10.47^{+0.02}_{-0.02}$	$-10.65^{+0.07}_{-0.07}$	$-10.31^{+0.11}_{-0.11}$	$-10.74^{+0.04}_{-0.25}$	$-11.47^{+0.02}_{-0.22}$	$-12.97^{+0.04}_{-0.04}$	$-13.51^{+0.02}_{-0.02}$

	$R_{\rm eff}$ (pc)	$5.75^{+0.05}_{-0.05}$	$5.64^{+0.09}_{-0.09}$	$5.74^{+0.19}_{-0.19}$	$5.81^{+0.10}_{-0.41}$	$6.12^{+0.08}_{-0.39}$	$5.22^{+0.07}_{-0.07}$	$4.99^{+0.03}_{-0.03}$
	n	$0.42^{+0.01}_{-0.01}$	$0.48^{+0.02}_{-0.02}$	$0.50^{+0.03}_{-0.03}$	$0.52^{+0.07}_{-0.02}$	$0.52^{+0.08}_{-0.04}$	$0.92^{+0.06}_{-0.01}$	$1.09^{+0.01}_{-0.02}$
	b/a	$0.24^{+0.01}_{-0.01}$	$0.25^{+0.01}_{-0.01}$	$0.24^{+0.02}_{-0.02}$	$0.23^{+0.04}_{-0.01}$	$0.20^{+0.02}_{-0.02}$	$0.27^{+0.01}_{-0.01}$	$0.28^{+0.01}_{-0.01}$
NGC 4395	A (mag)	0.09	0.08	0.06	0.05	0.03	0.01	0.01
	m (mag)	$17.54^{+0.01}_{-0.01}$	$17.62^{+0.01}_{-0.01}$	$18.45^{+0.03}_{-0.04}$	$17.73^{+0.06}_{-0.09}$	$16.98^{+0.03}_{-0.04}$	$15.63^{+0.02}_{-0.03}$	$15.32^{+0.03}_{-0.06}$
	M (mag)	$-10.72^{+0.01}_{-0.01}$	$-10.63^{+0.01}_{-0.01}$	$-9.78^{+0.03}_{-0.04}$	$-10.48^{+0.06}_{-0.09}$	$-11.21^{+0.03}_{-0.04}$	$-12.55^{+0.02}_{-0.03}$	$-12.86^{+0.03}_{-0.06}$
	$R_{\rm eff}$ (pc)	$1.80^{+0.02}_{-0.02}$	$2.67^{+0.03}_{-0.02}$	$3.47^{+0.05}_{-0.03}$	$3.62^{+0.06}_{-0.03}$	$4.56^{+0.05}_{-0.04}$	$2.97^{+0.10}_{-0.07}$	$3.25^{+0.45}_{-0.16}$
	n	$2.95^{+0.24}_{-0.10}$	$1.87^{+6.63}_{-6.63}$	$1.84^{+0.23}_{-0.16}$	$6.22^{+3.29}_{-3.29}$	$1.42^{+0.18}_{-0.12}$	$2.32^{+0.11}_{-0.10}$	$3.32^{+0.56}_{-0.56}$
	b/a	$0.66^{+0.01}_{-0.01}$	$0.72^{+0.01}_{-0.01}$	$0.84^{+0.01}_{-0.01}$	$0.84^{+0.01}_{-0.01}$	$0.87^{+0.01}_{-0.01}$	$0.96^{+0.01}_{-0.01}$	$0.91^{+0.01}_{-0.01}$
	m (mag)	$17.54^{+0.01}_{-0.01}$	$17.62^{+0.01}_{-0.01}$	$18.45^{+0.03}_{-0.04}$	$17.73^{+0.06}_{-0.09}$	$16.98^{+0.03}_{-0.04}$	$15.63^{+0.02}_{-0.03}$	$15.32^{+0.03}_{-0.06}$
	M (mag)	$-10.72^{+0.01}_{-0.01}$	$-10.63^{+0.01}_{-0.01}$	$-9.78^{+0.03}_{-0.04}$	$-10.48^{+0.06}_{-0.09}$	$-11.21^{+0.03}_{-0.04}$	$-12.55^{+0.02}_{-0.03}$	$-12.86^{+0.03}_{-0.06}$
NGC 7793	A (mag)	0.10	0.09	0.07	0.05	0.03	0.01	0.01
	m (mag)	$15.38^{+0.13}_{-0.10}$	$15.18^{+0.12}_{-0.10}$	$15.42^{+0.08}_{-0.04}$	$14.92^{+0.06}_{-0.05}$	$14.12^{+0.05}_{-0.06}$	$13.24^{+0.09}_{-0.16}$	$12.84^{+0.09}_{-0.16}$
	M (mag)	$-12.41^{+0.13}_{-0.10}$	$-12.59^{+0.12}_{-0.10}$	$-12.33^{+0.08}_{-0.04}$	$-12.82^{+0.06}_{-0.05}$	$-13.59^{+0.05}_{-0.06}$	$-14.46^{+0.09}_{-0.16}$	$-14.86^{+0.09}_{-0.16}$
	$R_{\rm eff}$ (pc)	$12.45^{+1.83}_{-1.83}$	$11.65^{+1.69}_{-1.65}$	$10.23^{+0.61}_{-1.00}$	$9.40^{+0.75}_{-0.82}$	$8.28^{+0.80}_{-0.65}$	$8.01^{+2.69}_{-1.02}$	$7.94^{+2.73}_{-1.02}$
	n	$1.39^{+0.24}_{-0.27}$	$1.74^{+0.27}_{-0.30}$	$2.08^{+0.14}_{-0.25}$	$2.50^{+0.21}_{-0.24}$	$2.85^{+0.26}_{-0.22}$	$3.12^{+1.09}_{-0.51}$	$3.29^{+1.18}_{-0.56}$
	b/a	$0.80^{+0.01}_{-0.01}$	$0.82^{+0.01}_{-0.01}$	$0.84^{+0.01}_{-0.01}$	$0.85^{+0.01}_{-0.01}$	$0.84^{+0.01}_{-0.01}$	$0.79^{+0.01}_{-0.01}$	$0.78^{+0.01}_{-0.01}$

Size vs. Luminosity

We show the F547M effective radius plotted against the F547M absolute magnitude for the NCs in our sample (Figure 3.9) for comparison with the NCs and the derived size-luminosity relation from Georgiev & Böker (2014). The magnitudes that they measured in the WFPC2 F606W and F555W filters were converted to *HST*/WFC3 F547M magnitudes using the PyRAF/STSDAS task `Calcphot`, assuming a 5 Gyr, solar metallicity simple stellar population (SSP) for the spectral shape (this is the same spectrum that they used to convert between *HST*/WFPC2 magnitudes and Johnson magnitudes). For NGC 2976, we show the F547M absolute magnitude and the F814W effective radius. Most of our clusters fall below the Georgiev & Böker (2014) best-fit size-luminosity relation, which may be in part due to our small sample size. In addition, because they used a large distance cut (40 Mpc), 11% of the NCs in their sample were not spatially resolved and thus were not used to derive their size-luminosity relation. As a result, the subset of spatially resolved NCs in their sample may be somewhat biased towards larger objects. It is also worth noting that the NC in IC 342 is exceptionally bright and compact. This NC is by far the brightest in our sample, and has a F547M absolute magnitude brighter than 95% of the NCs in the Georgiev & Böker (2014) sample.

NC Magnitude vs. Host Galaxy Magnitude

Böker et al. (2004) found that the luminosities of nuclear clusters in late-type spiral galaxies generally correlate with the total luminosities of their host galaxies. In particular, the I-band luminosities of NCs show a strong correlation with the B-band luminosity of the host, and a weak correlation with the far-IR luminosity of the host, which suggests that NC masses are more governed by the mass of the host galaxy rather than the total star formation rate of the host galaxy. In Figure 3.10, we plot the I-band absolute magnitudes of the NCs in our

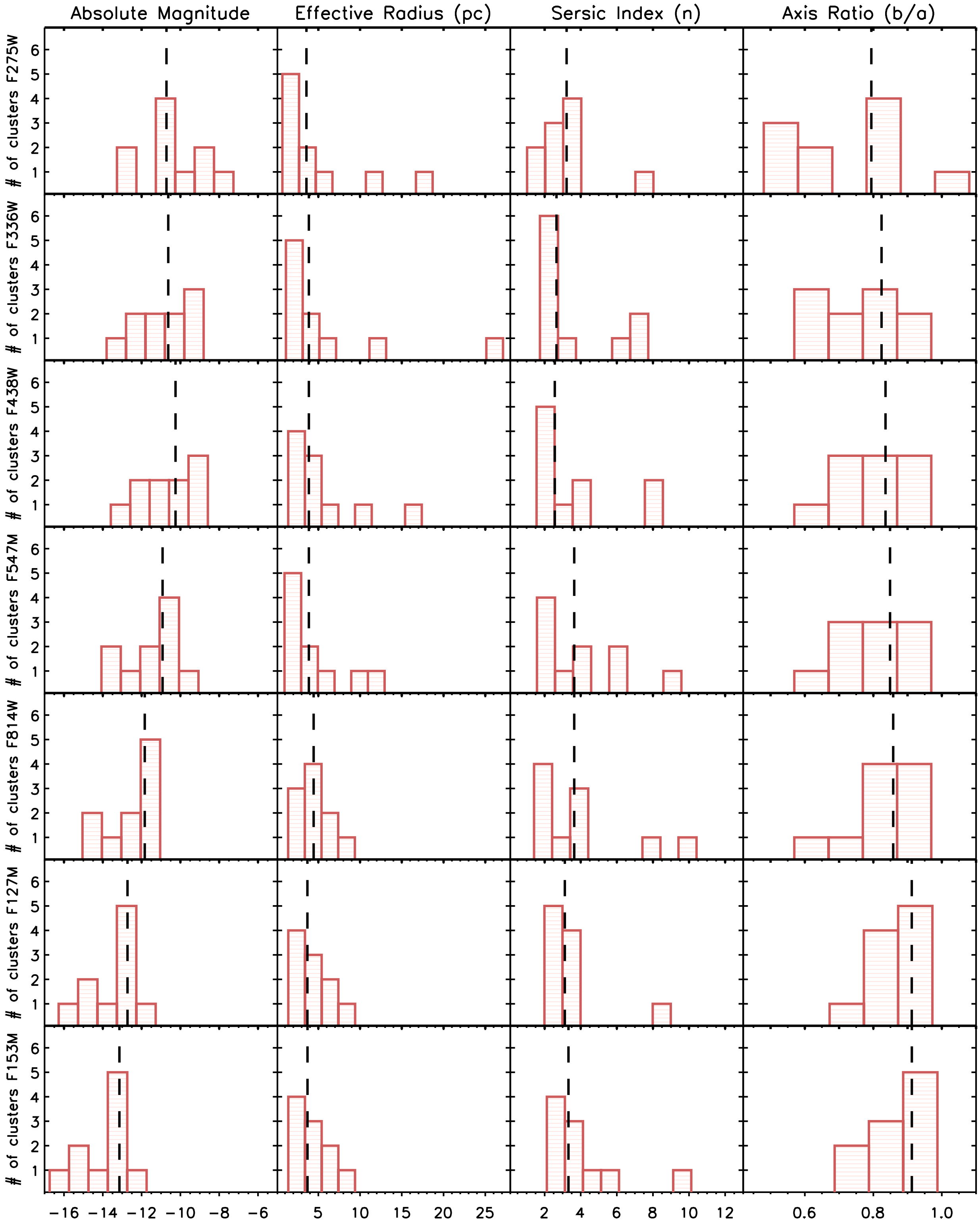

Figure 3.7 Histograms of the best-fit parameters in each band. For NGC 4244 and NGC 4395, the results of the single Sérsic component fits are shown. From left to right, each row contains (for a given band) histograms of absolute magnitudes, effective radii, Sérsic indices, and axis ratios. The median value for each parameter is denoted by a vertical dashed line.

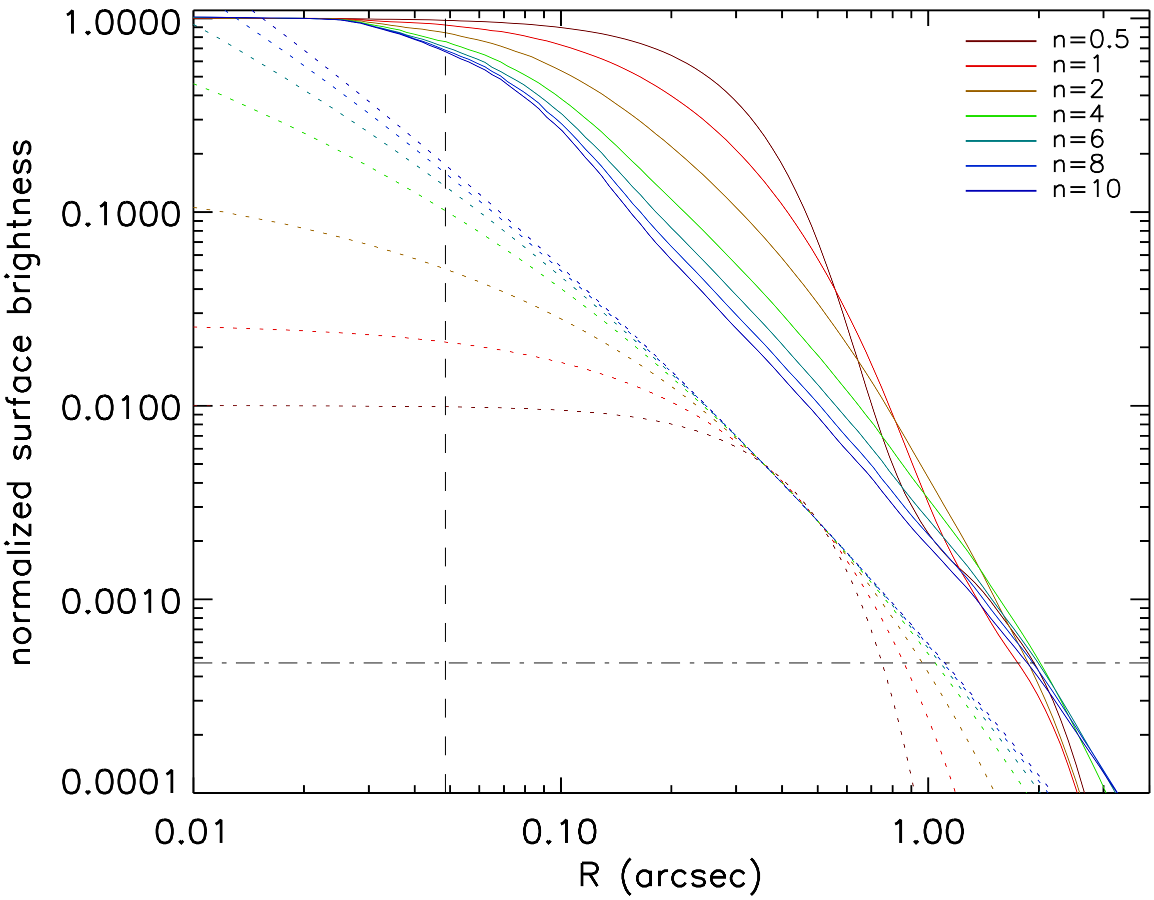

Figure 3.8 Sérsic models for $R_{\text{eff}} = 023$, with and without convolution with the F547M PSF. Solid lines denote Sérsic models that have been convolved with the F547M PSF, while the dotted lines denote intrinsic Sérsic models which have not been convolved with the PSF. Convolved models are normalized to the same surface brightness at $R = 0$, while unconvolved models are normalized at $R = 023$. The black vertical long-dashed line indicates the half width at half maximum of the F547M PSF. The black horizontal dash-dotted line indicates the ratio between the central surface brightness of the host galaxy and the central surface brightness of the NC in F814W, averaged over all ten objects in the sample.

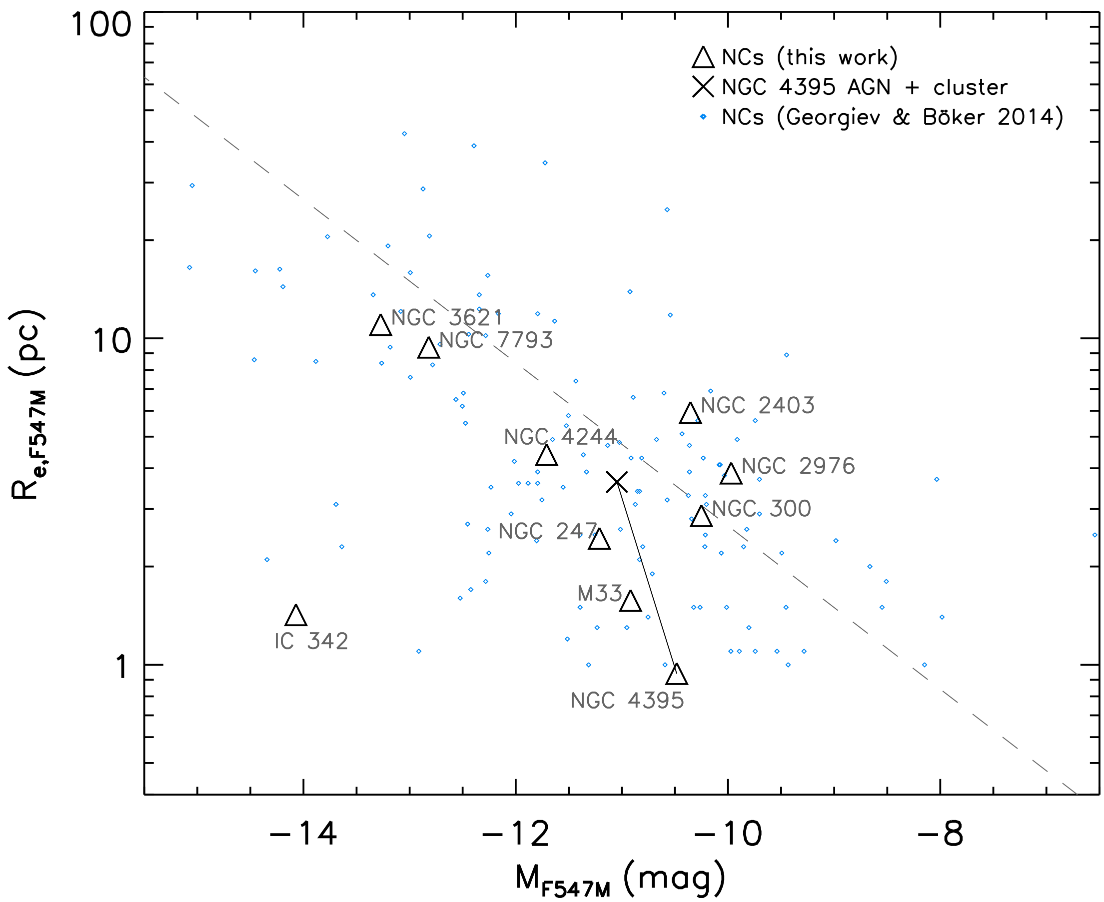

Figure 3.9 The effective radius measured in the F547M filter vs. the F547M absolute magnitude. Black triangles denote NCs from this work. The black "x" indicates the single Sérsic component fit to NGC 4395 (that is, the effective radius and magnitude of the NC plus AGN). The small light blue diamonds indicate NCs from Georgiev & Böker (2014) and the gray dashed line indicates the best-fit V band size-luminosity relation derived from their data set.

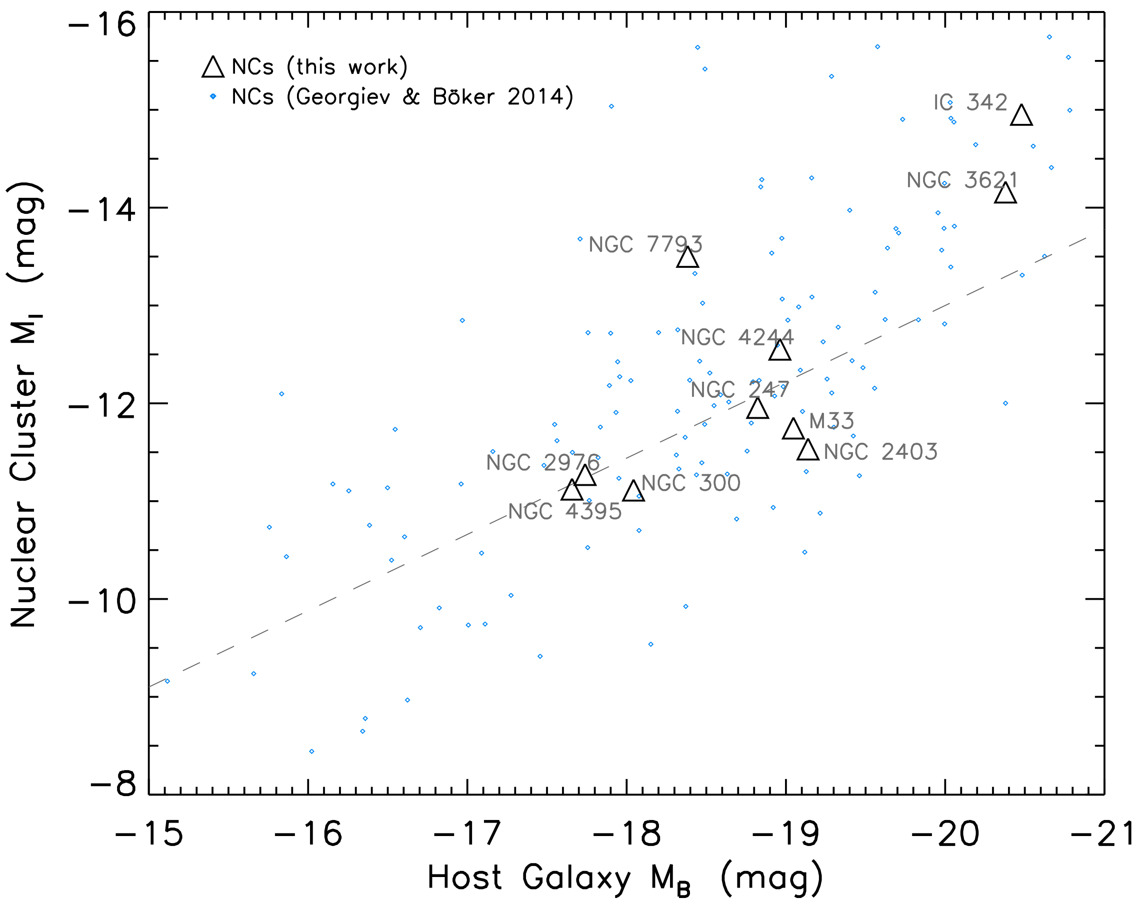

Figure 3.10 I-band absolute magnitudes of NCs vs. B-band absolute magnitudes of their host galaxies. Black triangles denote NCs from this work, and small light blue diamonds indicate NCs from Georgiev & Böker (2014). The gray dashed line indicates the best fit relation from Böker et al. (2004).

sample against the B-band absolute magnitudes of their host galaxies, which were taken from NED. We also include the NCs from Georgiev & Böker (2014) and show the best-fit relation from Böker et al. (2004). As described above, *HST* magnitudes were converted to Johnson magnitudes using `Calcphot`, assuming a 5 Gyr, solar metallicity SSP for the spectral shape, and extinctions in the Johnson B and I bands were determined using the method described in Section 2.2. Most of the objects in our sample lie close to the best-fit relation and have luminosities that are quite typical for NCs in late-type spiral galaxies.

3.2.2 Panchromatic Results

Color Gradients

We find a strong wavelength dependence of the the effective radius in the majority of the clusters, indicating radial color gradients. In Figure 3.11, we plot the best fit effective radius of each NC against wavelength, showing the results of the single Sérsic component fits for NGC 4244 and NGC 4395. We performed a formal power-law fit to each curve shown in Figure 3.11 to compute their slopes [$d\log(R_{\rm eff}/{\rm pc})/d\log(\lambda/{\rm Å})$] and corresponding uncertainties. For IC 342, NGC 2976, NGC 2403, and NGC 4244, the best-fit slope is consistent with zero at the 1 σ confidence level. Positive slopes were found for M33, NGC 247, NGC 300, and NGC 4395 (best-fit slopes of 0.24 ± 0.06, 1.00 ± 0.13, 0.53 ± 0.02, and 1.00 ± 0.01, respectively). This suggests the presence of a young population that is more concentrated than the bulk of the stars in the NC, or in the case of NGC 4395, indicates the presence of the AGN. These results are consistent with results from the recent *HST*/WFPC2 archival study by Georgiev & Böker (2014), which found that on average, NCs have larger effective radii when measured in redder filters. However, we find a trend of *decreasing* effective radius with wavelength in NGC 3621 and NGC 7793 (best-fit slopes of 0.95 ± 0.07 and -0.30 ± 0.10, respectively), which may indicate recent circumnuclear star formation. It should be noted that the larger extent of NGC 3621 in UV bands may be due to UV photons from the central engine of the AGN scattering off narrow-line region clouds rather than a radial gradient in the stellar populations. These color gradients will be explored in more detail in future work, where we will perform spatially resolved stellar population modeling of the NCs in this sample.

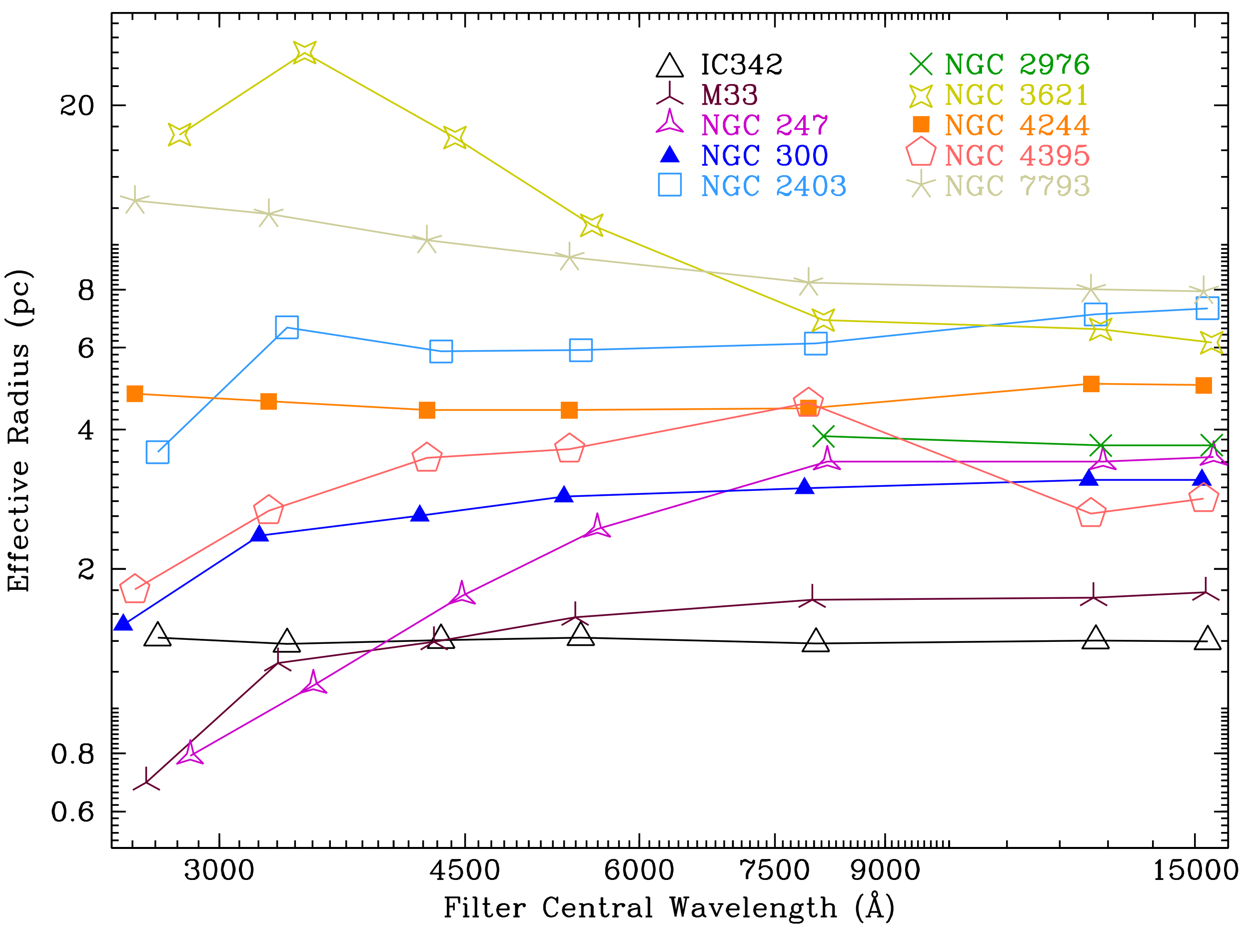

Figure 3.11 Effective radius of the NCs in each filter. For NGC 4244 and NGC 4395, the results of the single Sérsic component fits are shown.

Increasing Roundness With Wavelength

In a majority of the clusters, we also find a trend of increasing roundness with wavelength. In Figure 3.12, we plot best-fit NC axis ratios vs. wavelength, showing the results of the single Sérsic component fits for NGC 4244 and NGC 4395. We also include the axis ratios of the PSF in each band, all of which are nearly unity (> 0.98). We performed a formal power-law fit to each curve shown in Figure 3.12 to obtain best-fit slopes $[d \log(b/a)/d \log(\lambda/\text{Å})]$ and their corresponding uncertainties. For every NC in the sample, this slope is not consistent with zero at the 1 σ confidence level. IC 342 and NGC 7793 have slightly negative slopes, while every other NC has a positive slope, indicating a monotonically increasing axis ratio with wavelength. This suggests that the young stars in NCs often form in flattened disks, regardless of whether these disks are more extended or compact than the older stellar populations in the cluster. If a cluster contains a young population of stars in a flattened disk structure in addition to an older population in a spheroidal structure, the 2D axis ratio should be closer to unity when measured in redder bands, provided that the disk component is not face-on. On the other hand, if the young and old populations have identical morphologies, the axis ratio should not exhibit any trends with wavelength, but would not necessarily be equal to unity. Thus, if the young stars in NCs typically form in disks, while the older population is in a spheroidal distribution, we would expect objects containing a young stellar disk to exhibit a monotonic increase in axis ratio with wavelength. In NGC 4244, for example, the cluster is clearly being viewed edge-on, and the best-fit axis ratio from the single Sérsic component fits is $0.29^{+0.01}_{-0.01}$ in F275W and $0.44^{+0.01}_{-0.01}$ in F153M. This is consistent with a previous study by Seth et al. (2008b), which showed that the NC contains morphologically distinct old and young populations.

If the half-light radius of the cluster is significantly smaller than that of the PSF, the intrinsic axis ratio of the cluster will not be recovered in the fit. In the limit of spatially unresolved sources, the best-fit axis ratio will be completely determined by the axis ratio of the PSF,

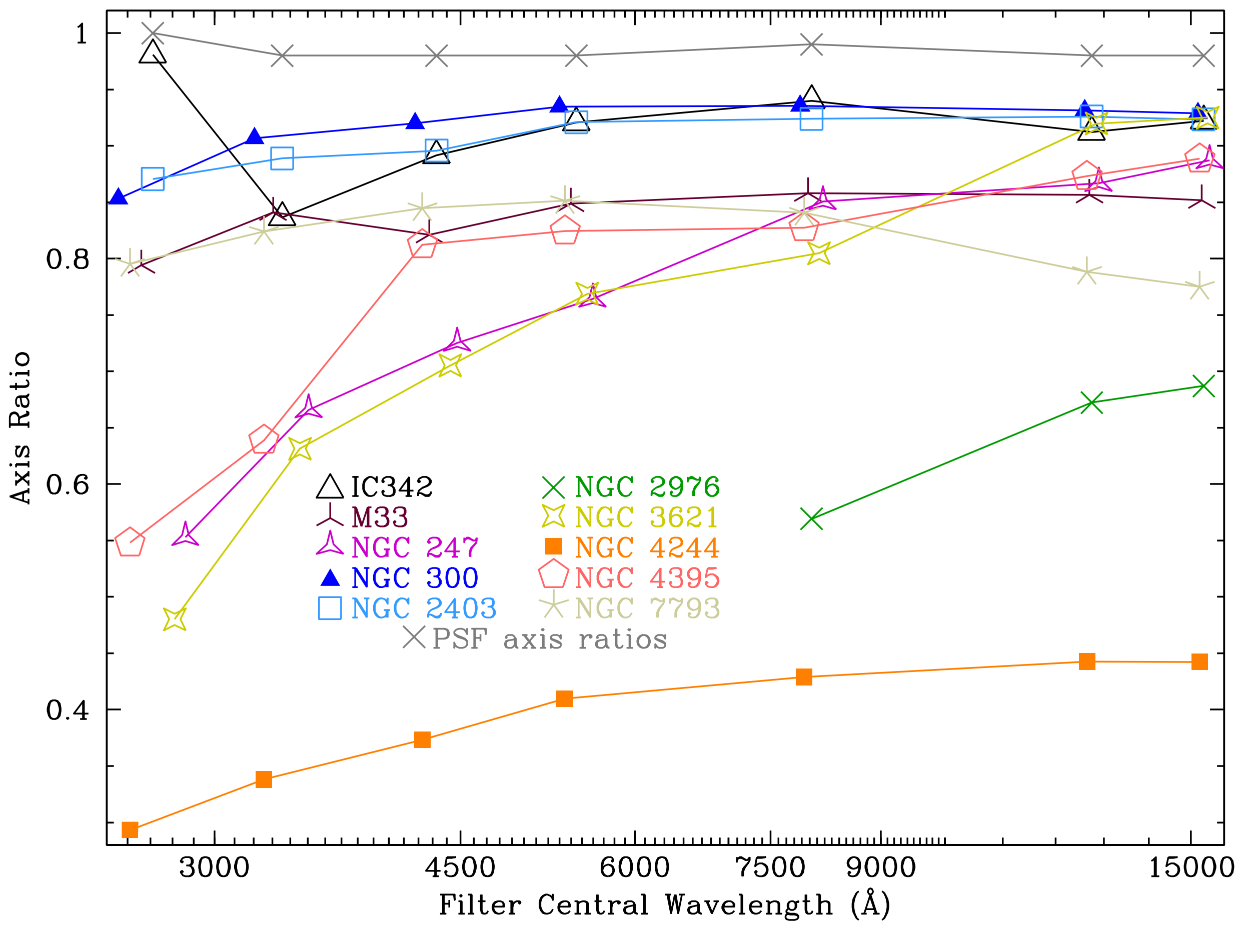

Figure 3.12 Axis ratios of the NCs in each filter. For NGC 4244 and NGC 4395, the results of the single Sérsic component fits are shown. The gray x's denote the axis ratio of the PSF in each filter.

which is always near unity. For our sample, the clusters are sufficiently well resolved that we were able to recover information about their axis ratios. With the exception of IC 342, all the clusters have effective radii larger than the PSF half-light radius in all bands. This suggests the variations in size and flattening with wavelength that we are observing are robust, indicating a difference in the spatial distribution of young and old stellar populations.

The flattening preferentially seen in the bluest bands indicates that the young stars form in disks, possibly fueled by the accretion of low angular momentum gas onto the center of the galaxy. However, simulations by Hartmann et al. (2011) demonstrated that the star cluster migratory/merger scenario can also produce NCs with young, blue disks, such as in NGC 4244. These simulations also showed that the star cluster migratory/merger and gas infall formation scenarios predict different kinematics in the resulting NC. Spatially resolved measurements of the kinematics of the NCs are needed to distinguish between these formation scenarios.

In Figure 3.13, we plot $d\log(b/a)/d\log(\lambda/\text{Å})$ (top panel) and F814W axis ratios (bottom panel) of the NCs against the axis ratios of the host galaxy disk, which were calculated using 2MASS K-band images (Jarrett et al., 2003). The galaxies in our sample with the smallest axis ratios contain the NCs that have the strongest trend of increasing roundness with wavelength and are the most flattened (this can also be seen in Figure 2.3). The *HST*/WFC3 images of the NCs in NGC 2976, NGC 3621, and NGC 4244 clearly show the presence of a disk which has the same orientation as the disk of the host galaxy. In each of these cases, the PA of the NC as measured by `GALFIT` is nearly aligned with the PA of the host galaxy (ΔPA $< 20°$). Conversely, none of the galaxies in our sample which are close to face-on contain flattened NCs. We conclude that blue disks which lie in the plane of the host galaxy are a common feature of NCs in late-type galaxies, but are difficult to detect in galaxies that are close to face-on.

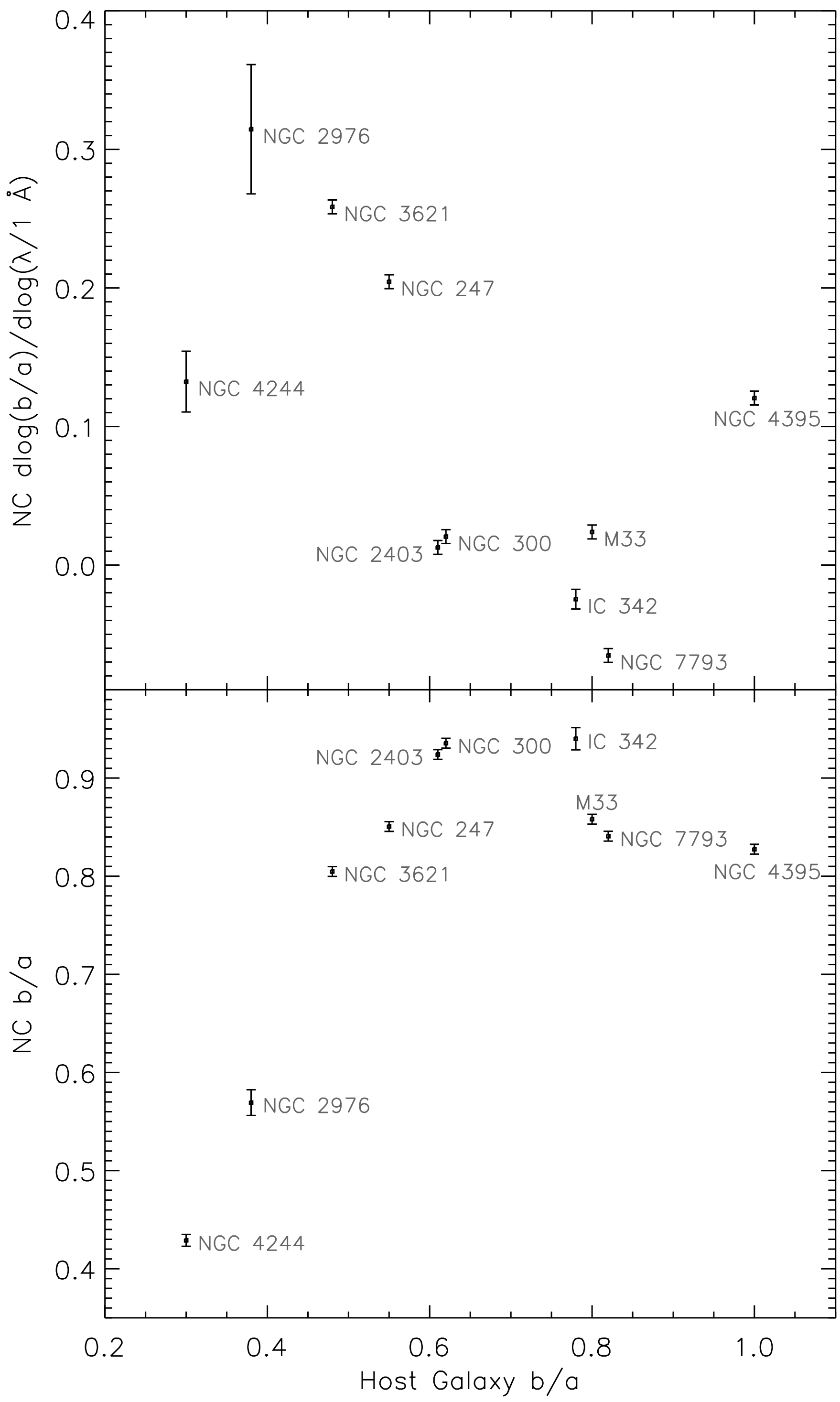

Figure 3.13 Top panel: $d\log(b/a)/d\log(\lambda/\text{Å})$ of each NC vs. the axis ratio of the host galaxy. These slopes $[d\log(b/a)/d\log(\lambda/\text{Å})]$ were calculated by performing a formal power-law fit to the curves shown in Figure 3.12. Bottom panel: axis ratios of the NCs measured in F814W vs. the axis ratios of their host galaxies.

3.2.3 Stellar Populations

Nuclear Cluster SEDs

For each cluster, we measured a total apparent magnitude using either `GALFIT` or aperture photometry in all seven bands, allowing us to construct a spectral energy distribution (SED) spanning the near-UV to the near-IR in wavelength. We corrected for Galactic extinction using dust maps from Schlafly & Finkbeiner (2011), as explained in Section 2.2. Magnitudes were converted to flux units (erg s^{-1} cm^{-2} $Å^{-1}$) using `Calcphot`, then finally converted to luminosities using the distances given in Table 2.1. The resulting SEDs are shown in Figure 3.14. Color-color diagrams (see below) provide a way to visualize the comparison between the observed SEDs and model spectra. Fits of multi-component stellar population models to the NC SEDs are needed to more precisely characterize the stellar populations present in each NC, and will be described in a future paper.

Nuclear Cluster Colors

In order to characterize their stellar populations, we computed NC colors from our extinction-corrected absolute magnitudes and compared them to colors of single-age simple stellar populations from Bruzual & Charlot (2003b) for metallicity $Z = 0.008$, 0.02, and 0.05. We created two color-color diagrams, one spanning UV to the IR, and one restricted to the optical bands, which are given in Figures 3.15 and 3.16, respectively. For NGC 4395, we show colors of the NC (Sérsic component, denoted by a black triangle) as well as the combined colors of the NC and AGN (Sérsic plus point source component, denoted by a black "x"). We also include colors of the NCs from Georgiev & Böker (2014) on the optical only color-color plot. The magnitudes that they measured in the WFPC2 F450W, F606W, and F814W filters were converted to magnitudes in the *HST*/WFC3 F438W, F547M, and F814W filters using

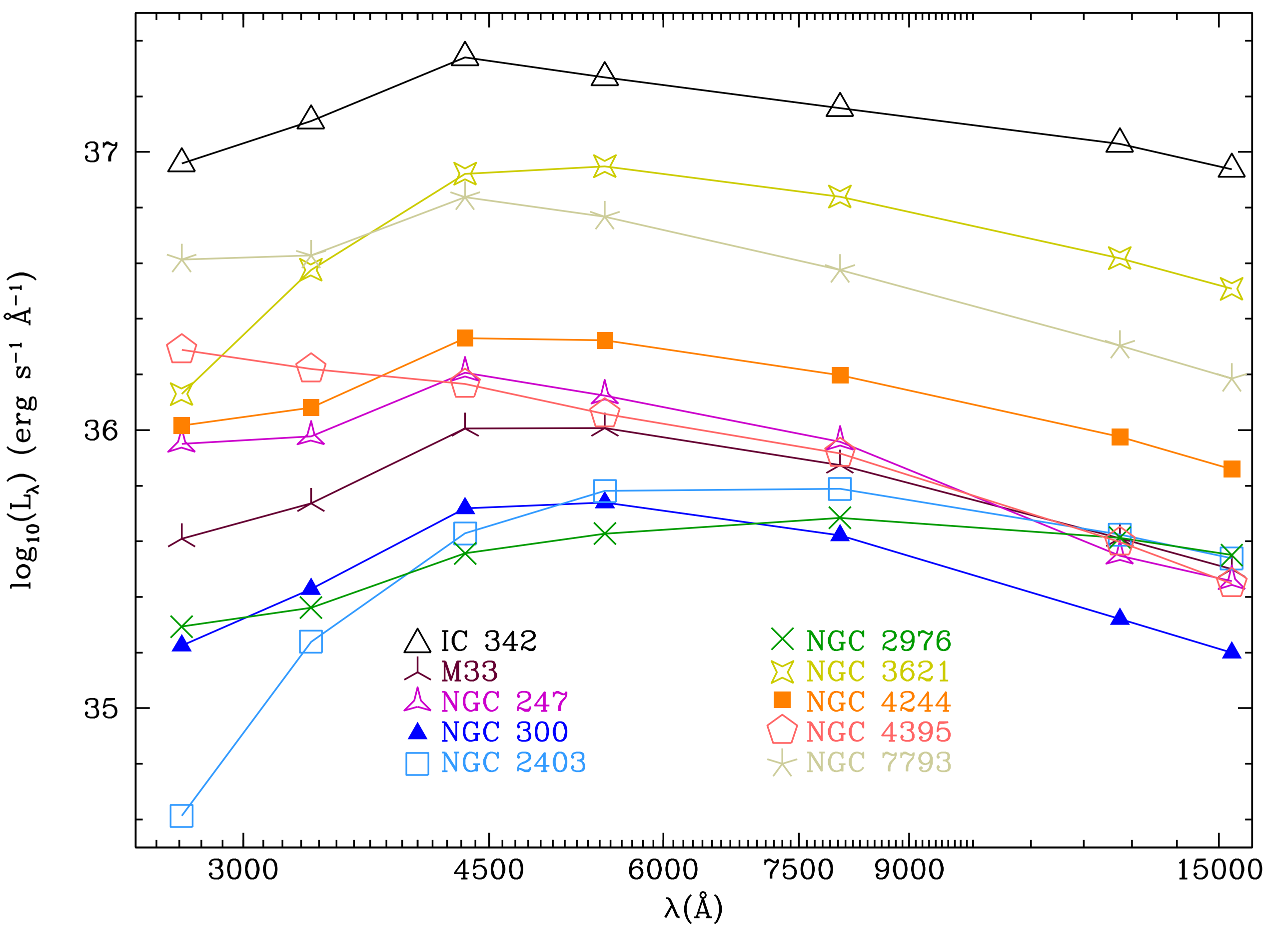

Figure 3.14 SEDs of the 10 NCs in our sample. For NGC 4244 and NGC 4395, we show the composite SED of the two components of the fit.

`Calcphot`, assuming a 5 Gyr, solar metallicity SSP for the spectral shape. In this plot, our NCs fall close to the SSP tracks and are broadly consistent with the colors of the NCs from Georgiev & Böker (2014).

Most of the NCs in our sample lie at locations distinctly offset from the SSP tracks in F336W − F438W vs. F547M − F127M color-color space, confirming that a mix of stellar populations with different ages is present in many of the NCs. This is expected, given that previous studies have shown that the star formation histories of NCs are generally not well described by a single starburst event (Walcher et al., 2006; Rossa et al., 2006). In order to investigate the mix of ages, we took linear combinations of Bruzual & Charlot (2003b) SSP spectra with ages 11 Gyr and 25 Myr and computed their colors in order to construct a "mixing curve", which traces the color of the total population as the fractional contribution from the 11 Gyr population to the total luminosity is adjusted from 1.0 to 0.0 and the contribution from the 25 Myr population to the total luminosity is adjusted from 0.0 to 1.0, in steps of 0.1. A mixing curve for a combination of a 11 Gyr and 290 Myr SSP is also included in the UV-optical-IR color-color plot. The typical age mix for the NCs in our sample is a combination of an old ($>$ 1.4 Gyr) and a young (100 - 300 Myr) population. The mix of ages is in the NCs is obvious when considering colors that span the UV to the IR, but is not apparent from the optical colors only. These color-color plots reinforce the conclusions of de Meulenaer et al. (2014), who highlighted the importance of broad wavelength coverage in stellar population studies, and demonstrated how degeneracies between age, metallicity and extinction, which limit stellar population studies that utilize optical bands only, can be broken with full UV to IR coverage.

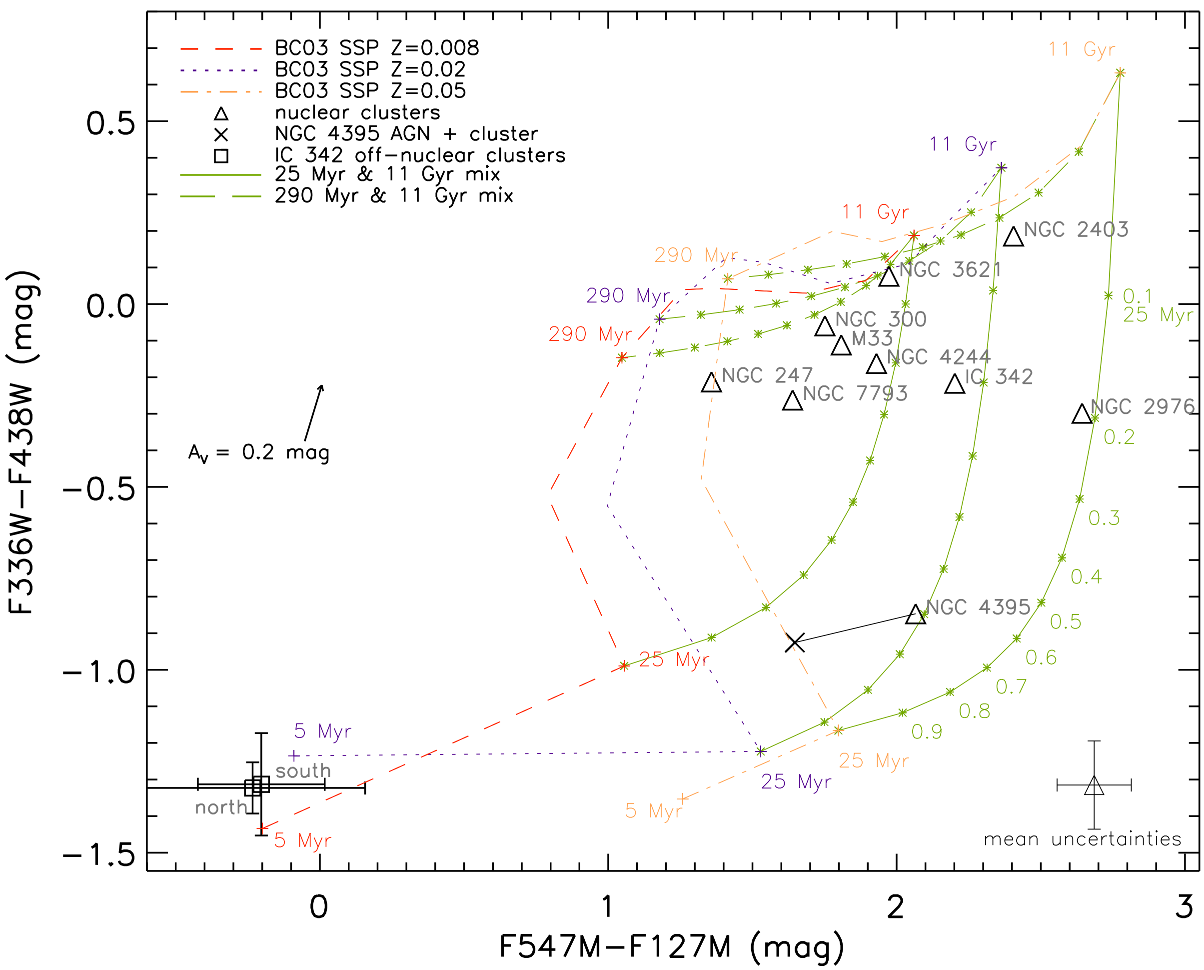

Figure 3.15 F336W − F438W vs. F547M − F127M colors. Black triangles denote NCs from this work, and the off-nuclear clusters in IC 342 are shown as black squares. For NGC 4395, we show colors of the NC as well as the combined colors of the NC and AGN (denoted by a black "x"). We include evolutionary tracks of SSPs from Bruzual & Charlot (2003b) with $Z = 0.008$ (denoted by the red dashed line), $Z = 0.02$ (purple short-dashed line), and $Z = 0.05$ (orange dash-dot line). Mixing curves for a combination of Bruzual & Charlot (2003b) SSPs with age 25 Myr and 11 Gyr are denoted by the solid gray green lines, and mixing curves for a combination of 290 Myr and 11 Gyr SSPs are denoted by the long-dashed gray green lines. We include mixing curves for metallicity $Z = 0.008$, 0.02, and 0.05. The arrow indicates a reddening vector of $A_V = 0.2$ mag. The error bars in the lower right corner show the mean uncertainty in the colors on each axis (averaged over all NCs in the sample).

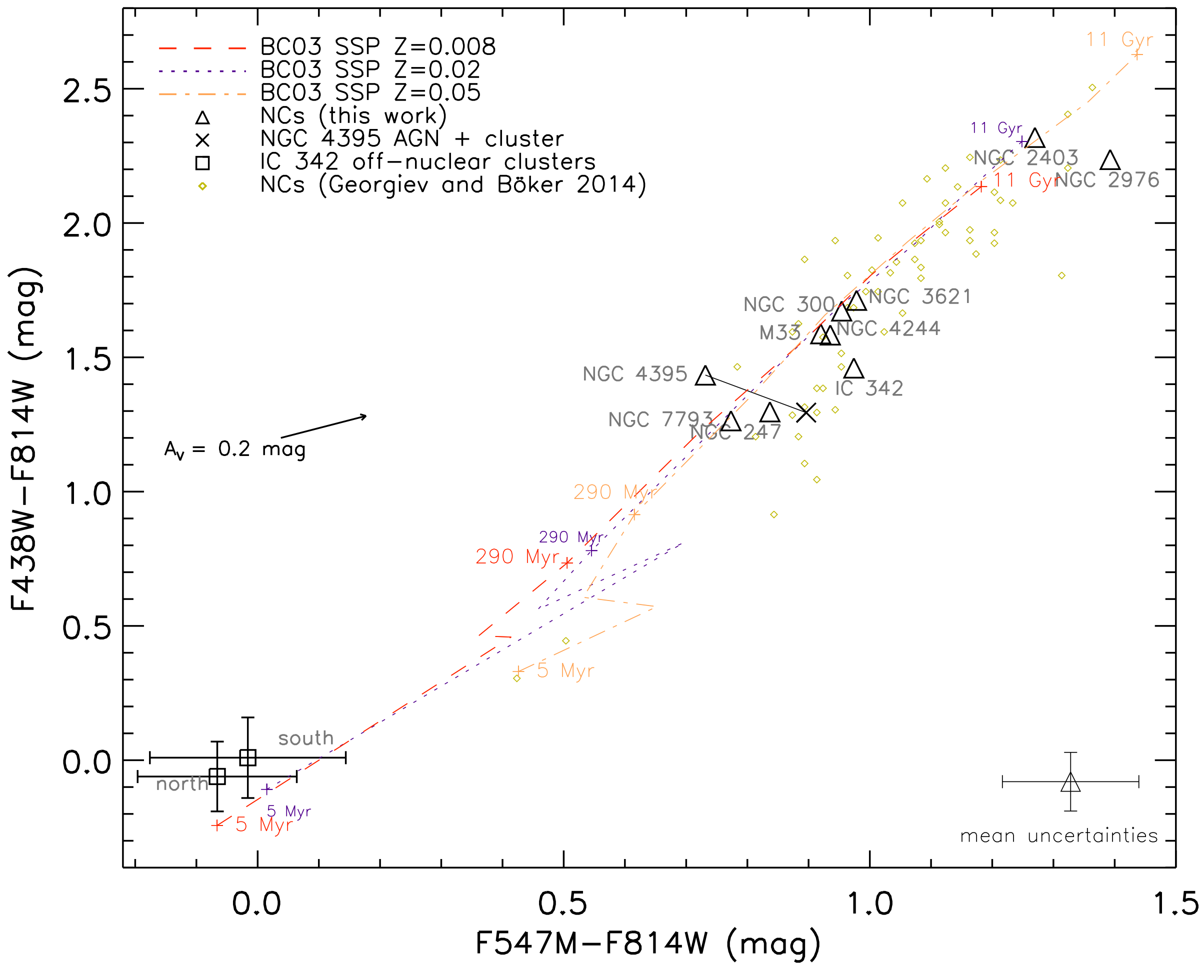

Figure 3.16 F438W − F814W vs. F547M − F814W colors. We include NC colors from Georgiev & Böker (2014), denoted by small gold diamonds. We did not include mixing curves in this plot because the model tracks are nearly straight lines in this color-color space, especially at older ages.

3.3 Comments on Individual Objects

3.3.1 IC 342

IC 342 is a face-on giant Scd spiral galaxy located in the Maffei Group at a distance of 3.3 Mpc (Saha et al., 2002). In a dynamical study of IC 342 using CO bandhead spectra and *HST*/WFPC2 images, Böker et al. (1999) measured an integrated stellar velocity dispersion of 33 km s^{-1} for the NC, estimated the total stellar mass to be 6×10^6 $M_\odot$, and placed an upper limit on the mass of any central BH of 5×10^5 $M_\odot$. Due to its proximity to the Galactic plane, there is significant foreground extinction, particularly in the UV bands ($A_{\rm F275W}$= 2.94 mag). There are dust lanes to the east and west of the main cluster that we masked out during the fits. We were able to fit a model consisting of an exponential disk and a flat sky level to the host galaxy in every band, and the nuclear cluster was fit using a single Sérsic component in every band. Böker et al. (1999) measured an apparent V-band magnitude of 15.19 mag for the cluster, which corresponds to an extinction-corrected F547M absolute magnitude of -13.91 mag, which is somewhat discrepant with our measurement of $-14.07^{+0.07}_{-0.14}$ mag. However, the *HST*/WFC2 images that they used were saturated in the core of the NC, which may explain the discrepancy. The NC in IC 342 is one of the most compact and by far the most luminous in our sample, with an I-band absolute magnitude $M_{\rm F814W}$= $-15.05^{+0.06}_{-0.08}$ mag. The effective radius is nearly constant with wavelength, with a best-fit value of $1.38^{+0.19}_{-0.13}$ pc in F814W.

There are several off-nuclear clusters in the central regions of IC 342. The brightest two are located 211 (projected distance 33.55 pc) to the north and 192 (30.53 pc) to the south of the NC, respectively. Although other galaxies in our sample contain off-nuclear clusters, these two were included in the color-color diagrams in Section 3.2.3 because they are by far the most luminous in our sample, and actually outshine the main NC in UV bands. We measured their magnitudes using aperture photometry over a circular aperture (and applied an aperture correction to account for flux lost outside the aperture due to PSF blurring), because `GALFIT` could not converge on a good fit without the use of constraints. These off-nuclear clusters have extremely blue colors, consistent with 5 Myr SSPs, as shown on the color-color diagrams shown in Figures 3.15 and 3.16. We will carry out a more detailed examination, including an analysis of stellar population ages and stellar masses, of the complete set of off-nuclear clusters in our sample in future work.

3.3.2 M33

Located at a distance of 0.9 Mpc (Bono et al., 2010), M33 is the only member of the Local Group in our sample. Gebhardt et al. (2001) measured an integrated velocity dispersion of 20 km s^{-1} for the cluster, and placed a very tight upper limit on the mass of any central BH of 1500 $M_\odot$. Using the same *HST* data, Merritt et al. (2001) placed an upper limit of 3000 $M_\odot$ on the mass of the central BH. Kormendy et al. (2010) estimated the total stellar mass in the cluster to be 10^6 $M_\odot$. The nucleus of M33 coincides with the ultraluminous X-ray source X-8 (Trinchieri et al., 1988), which is believed to be a stellar-mass BH accreting at a super-Eddington rate (Foschini et al., 2004).

In all bands, we fit a flat sky level to the host galaxy and a single Sérsic component to the nuclear cluster. The NC in M33 is one of the most compact in the sample. We find a steady increase in the effective radius with filter central wavelength from $0.69^{+0.29}_{-0.10}$ pc in F275W to $1.78^{+0.20}_{-0.13}$ pc in F153M, which indicates that the center of the cluster is bluer than the wings. This is consistent with a *HST*/WFPC2 imaging study by Lauer et al. (1998), which found a decrease in the $V-I$ color towards the center of the cluster, and a study by Kormendy & McClure (1993) which found a similar gradient in the $B-R$ color.

3.3.3 NGC 247

NGC 247 is a member of the Sculptor Group, at a distance 3.4 Mpc (Bono et al., 2010). We fit a flat sky level to the host galaxy and a single Sérsic component to the NC in all bands. We find evidence for a color gradient within this cluster as well. The effective radius is smallest in the UV and increases towards the IR, with a best-fit value of $0.79^{+0.07}_{-0.07}$ in F275W and $3.49^{+1.80}_{-0.69}$ in F153M. The best-fit axis ratio is $0.55^{+0.01}_{-0.01}$ in F275W and monotonically increases to $0.89^{+0.01}_{-0.01}$ in F153M, which suggests that the young stars formed in a disk.

3.3.4 NGC 300

At a distance of 2.0 Mpc (Bono et al., 2010), NGC 300 lies in the field between the Local Group and the Sculptor Group. Walcher et al. (2005) measured a stellar velocity dispersion of 13.3 km s^{-1} and a mass of $10^{6.02}$ $M_\odot$ for the NC. We fit a flat sky level to the host galaxy and a single Sérsic component to the NC in all bands. NGC 300 was included in the Böker et al. (2002) *HST*/WFPC2 NC imaging survey, where an I-band absolute magnitude of -11.43 ± 0.40 mag was measured for the NC. Correcting for the slightly different distances used, this corresponds to a WFC3 F814W absolute magnitude of -11.08 ± 0.40 mag, which is consistent with our measurement of $-11.20^{+0.02}_{-0.02}$ mag. The best-fit effective radius increases monotonically from $1.52^{+0.03}_{-0.03}$ pc in F275W to $3.12^{+0.25}_{-0.16}$ pc in F153M, indicating a color gradient within the cluster. The Sérsic index is nearly constant across all filter bands, with a value of $2.27^{+0.10}_{-0.08}$ in F814W.

3.3.5 NGC 2403

NGC 2403 resides in the outskirts of the M81 Group at a distance of 3.1 Mpc (Saha et al., 2006). In addition to the NC, NGC 2403 hosts a highly variable central X-ray source, likely to be an X-ray binary system with a stellar mass BH accretor (Yukita et al., 2007). We fit a flat sky level to the host galaxy and a single Sérsic component to the NC in every band. Dust lanes southwest of the NC were masked out during the fits. With an effective radius of 6.13 pc and an absolute magnitude of $-11.62^{+0.11}_{-0.10}$ in F814W, the cluster has a low surface brightness, leading to relatively large uncertainties in the fit parameters. The effective radius of the cluster is generally larger when observed in redder filters, with a value of in $3.57^{+5.08}_{-0.90}$ pc F275W and $7.29^{+3.28}_{-1.23}$ pc in F153M.

3.3.6 NGC 2976

NGC 2976 is located at a distance of 3.6 Mpc (Jacobs et al., 2009) in the M81 group. In F814W, F153M, and F153M, we were able to fit a single Sérsic component to the NC while fitting a flat sky level to the host galaxy. In these bands, the cluster is highly flattened and the PA is nearly aligned with that of the host galaxy disk ($b/a = 0.57$ and $\Delta\text{PA} = 13°$ in F814W). In the bands blueward of F814W, the structure of the NC is difficult to fit with any reasonable set of analytic models due to its small-scale clumpiness. In these bands, the cluster can be resolved into two distinct structures: a compact blue component to the north and a more extended, irregularly shaped red component to the south (see Figure 2.3). The contrast between these components diminishes at larger wavelengths, and they completely blend together in the F814W, F127M, and F153M images (as can be seen in Figure 2.2). In order to obtain the total cluster magnitude in F275W, F336W, F438W, and F547M, we performed aperture photometry using an elliptical aperture centered on the centroid of the cluster. We used the axis ratio and position angle of the best-fit Sérsic model in F814W to define the position angle and axis ratio of the elliptical aperture. The semimajor axis of the aperture we used was $9 \times R_{\mathrm{e,F814W}}$ (where $R_{\mathrm{e,F814W}}$ is the best-fit effective radius for the cluster in F814W), while the inner and outer radii of the sky annulus were $9 \times R_{\mathrm{e,F814W}}$ and $10 \times R_{\mathrm{e,F814W}}$, respectively. These aperture and sky annulus sizes were found to give the best agreement with the total cluster magnitude obtained from `GALFIT` in F814W, F127M, and F153M. We calculated a mean difference of 0.10 mag between the total cluster magnitude obtained from `GALFIT` and from aperture photometry in F814W, F127M and F153M, and used this to define the measurement uncertainty. From aperture photometry, we measured the following extinction-corrected absolute magnitudes for the cluster: $M_{\rm F275W} = -9.10$ mag, $M_{\rm F336W} = -9.43$ mag, $M_{\rm F438W} = -9.13$ mag, $M_{\rm F547M} = -9.97$ mag.

We also measured the magnitude of the blue component in F275W, F336W, F438W, and F547M by performing aperture photometry over a circular aperture. In each band, we performed the measurement 12 times using aperture radii in the range 2–5 pixels, inner sky radii in the range 5–20 pixels and outer sky radii in the range 10–30 pixels, applying the appropriate aperture correction each time. We calculated the median between the largest and smallest magnitude obtained from the 12 trials, and used this range to define the associated measurement uncertainty. We obtained the following absolute magnitudes for the blue component: $M_{\rm F275W} = -8.49 \pm 0.09$ mag, $M_{\rm F336W} = -8.38 \pm 0.22$ mag, $M_{\rm F438W} = -7.35 \pm 0.50$ mag, $M_{\rm F547M} = -7.98 \pm 0.78$ mag. For comparison, the brightest Wolf-Rayet and O stars in the R136 cluster in the LMC have V-band absolute magnitudes as bright as -7.33 mag (Crowther et al., 2010). Because of the large uncertainties in our measurements, we cannot rule out the possibility of the blue component being an extremely luminous, hot star, although it may also be a very young, compact star cluster. We are unable to determine whether this object is associated with the NC or being viewed in projection.

3.3.7 NGC 3621

NGC 3621 is the most distant galaxy in our sample, at 7.3 Mpc (Saha et al., 2006). The NC has a velocity dispersion of 43 km s^{-1}, one of the largest ever measured for any NC in a late-type spiral galaxy, which sets a fairly high upper limit on the mass of any central BH of $3 \times 10^6\ M_\odot$ (Barth et al., 2009). Satyapal et al. (2007) discovered a faint AGN in the NC from mid-IR [Ne5] line emission and based on estimates of its bolometric luminosity, set a lower limit on the mass of the central BH of $4 \times 10^3\ M_\odot$. Gliozzi et al. (2009) found further evidence for an AGN in NGC 3621 with the detection of a weak X-ray point source coincident with the nucleus.

We successfully fit an exponential profile plus a flat sky level to the host galaxy in every band, and we fit a single Sérsic component to the NC in all seven bands. Although NGC 3621 contains an AGN, adding a point source component did not improve the quality of the fits, consistent with expectations for a highly obscured AGN. Dust lanes northeast, southeast, and northwest of the NC were masked out during the fits. Barth et al. (2009) measured a J-band apparent magnitude of 14.14 mag for the NC from archival NICMOS images, which corresponds to a F127M absolute magnitude of −15.24 mag, in very good agreement with our measurement of $-15.25^{+0.07}_{-0.13}$ mag. The NC has a very large Sérsic index ($n > 7$) in all bands, with a best-fit value as high as $9.73^{+1.00}_{-1.67}$ in F127M. In the UV, the cluster is highly elongated along the north-south axis, with an axis ratio (b/a) of $0.48^{+0.01}_{-0.01}$. This elongated UV emission can also be seen in the color composite image shown in Figure 2.3. The axis ratio monotonically increases with wavelength to $0.93^{+0.01}_{-0.01}$ in F153M. The cluster is also more extended in the UV, with an effective radius of $17.27^{+3.83}_{-3.83}$ pc in F275W and in $6.15^{+0.72}_{-0.72}$ F127M. The greater north-south elongation and larger extent of the cluster in the UV could potentially be explained by UV emission from the central engine being obscured by an edge-on torus oriented along the east-west axis and scattering off narrow-line region clouds to the north and the south. If so, the extended UV emission would be linearly polarized. Alternatively, the extended UV emission could be explained by extended star formation in the outskirts of the cluster. In F275W, the PA of the semimajor axis of the NC is nearly aligned (ΔPA $= 19°$) with the PA of the host galaxy measured from the 2MASS K-band image (Jarrett et al., 2003), which is expected if the NC primarily grows through gas accretion rather than star cluster mergers (Seth et al., 2006; Hartmann et al., 2011).

However, there is no correlation between the orientation of AGNs and their host galaxies (Fischer et al., 2013), so we cannot determine the nature of the extended UV emission from our UV images alone. UV spectroscopy and/or polarimetry can help to distinguish between young stars and scattered AGN emission.

3.3.8 NGC 4244

Located at a distance of 4.3 Mpc (Jacobs et al., 2009) in the M94 Group, NGC 4244 is the only galaxy in our sample with an edge-on orientation. In a recent Gemini Near-Infrared Integral Field Spectrograph (NIFS) study of this NC, Seth et al. (2008b) discovered rotation of 30 km s^{-1} in the central 10 pc of the cluster and found that the NC contains two distinct populations: an old, compact spheroidal component and a young, extended disk component. In each band, we fit an edge-on exponential disk plus a flat sky level to the host galaxy, while the NC was modeled with two Sérsic components. In F814W, the flattened component has an effective radius of $6.12^{+0.08}_{-0.39}$ pc, a Sérsic index of $0.52^{+0.08}_{-0.04}$, and an axis ratio of $0.20^{+0.02}_{-0.02}$, while the rounder component has an effective radius of $3.53^{+0.42}_{-0.31}$ pc, a Sérsic index of $1.71^{+0.61}_{-0.20}$, and an axis ratio of $0.67^{+0.06}_{-0.01}$. SEDs of the two components, as well as plots of their effective radii, Sérsic indices, and axis ratios as a function of wavelength are shown in Figure 3.17. We also fit a single Sérsic component to the NC in each band for comparison with other clusters. The single Sérsic component effective radius is nearly constant with wavelength, with a best-fit value of $4.77^{+0.02}_{-0.02}$ pc in F275W and $4.98^{+0.01}_{-0.01}$ in F153M. From the single Sérsic component fits, we find that the axis ratio monotonically increases from $0.29^{+0.01}_{-0.01}$ in F275W to $0.44^{+0.01}_{-0.01}$ in F153M, and the semimajor axis is nearly aligned with that of the host galaxy in every band ($\Delta PA = 12° - 13°$). The alignment of the NC and host galaxy semimajor axes is consistent with previous studies of NGC 4244 (Seth et al., 2006; Hartmann et al., 2011; De Lorenzi et al., 2013), and suggests that gas accretion has played a significant role in the formation of the NC.

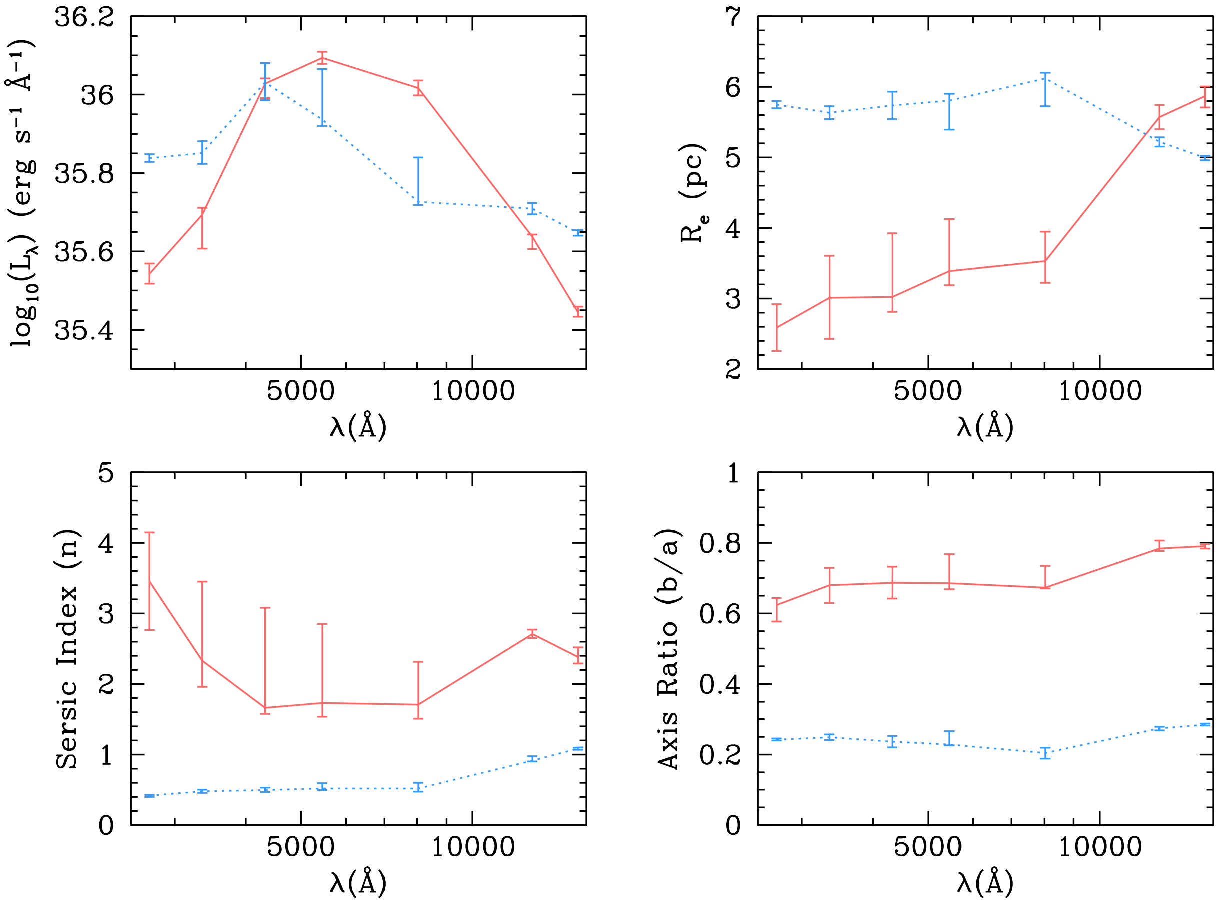

Figure 3.17 Luminosities, effective radii, Sérsic indices and axis ratios of the individual Sérsic components as a function of filter central wavelength for NGC 4244. The cluster consists of an extended, highly flattened, blue component and a compact, spheroidal, red component. These components are denoted with a blue short-dashed line and a red solid line, respectively.

3.3.9 NGC 4395

NGC 4395 is oriented face-on at a distance of 4.3 Mpc (Thim et al., 2004) in the M94 Group. The existence of a NC in NGC 4395 was explicitly demonstrated by Filippenko & Ho (2003), from `GALFIT` analysis of a *HST*/WFPC2 *I*-band image. The discovery of faint broad hydrogen and helium lines in its optical spectrum revealed that NGC 4395 contains one of the least luminous Type 1 AGNs known (Filippenko & Sargent, 1989). A *HST*/STIS reverberation-mapping program by Peterson et al. (2005) yielded an estimate of 3.6×10^5 $M_\odot$ for the mass of the central BH, which implies that the AGN is very underluminous and is accreting at just 1.2×10^{-3} times the Eddington rate. In a recent photometric reverberation mapping campaign, Edri et al. (2012) measured an Hα lag of just 3.6 hours, corresponding to a BH mass of 5×10^4 $M_\odot$ (the large discrepancy in the BH mass estimates from this study and Peterson et al. is in part due to the different assumed values of the scaling factor in the BH mass calculation, which depends on the unknown geometry and kinematics of the broad-line region). Minezaki et al. (2006) detected J and H band flux variations over a single night of monitoring of the AGN, in addition to large flux variations in optical to near-IR bands on timescales of days to months.

We used a flat sky level to model the host galaxy, a single Sérsic component for the NC, and included a point source component for the AGN, since the central engine is unobscured along the line of sight. There is an emission line region west of the cluster which was masked during the fits. With no constraints on any of the fit parameters, we find that the Sérsic component has the largest effective radius in the F814W band (R_{eff} = 4.56 pc, $n = 1.42$), and the smallest effective radius in F275W (R_{eff} = 1.80 pc, $n = 3.01$). We found no obvious trends in the effective radius or the Sérsic index with wavelength. In order to examine the degeneracy between the magnitude of the Sérsic component and the point source component in our fits, we repeated the fits in all seven bands with the effective radius of the Sérsic component fixed at 1.80 pc and the Sérsic index fixed at 3.01, and then again with

with the effective radius fixed at 4.56 pc and the Sérsic index fixed at 1.42. The range of magnitudes obtained from these fits gives a rough estimate of the photometric uncertainties due to the degeneracy between the profiles of the point source component and the Sérsic component in the fits. Figure 3.18 shows the SED of both the Sérsic component and point source component obtained from these fits. From single Sérsic component fits (with no PSF component), we find that the axis ratio monotonically increases from $0.55^{+0.01}_{-0.01}$ in F275W to $0.89^{+0.01}_{-0.01}$ in F153M.

Filippenko et al. (1993) measured a UV continuum slope of $\alpha = -2$ by fitting a power-law model of the form $f_\nu \propto \nu^\alpha$ to a *HST*/Faint Object Spectrograph (FOS) spectrum of the AGN over the range 2200 to 3300 Å. We fit a single power-law model to the SED of the AGN from the `GALFIT` decomposition over all seven photometric bands using the IDL-based least-squares fitting code `MPFIT` (Markwardt, 2009), and measured a continuum slope $\alpha = -0.8 \pm 0.2$. We also independently fit power-law models to the SED in the UV and from the optical to the IR, and measured a slope of -1.5 ± 0.6 between F275W and F336W, which is consistent with Filippenko et al. (1993), and a measured a slope of -0.3 ± 0.4 between F438W and F153M. However, our observations only represent a single temporal snapshot of the state of the AGN, and past observations have shown that the optical continuum shape of the AGN sometimes undergoes rapid changes. Lira et al. (1999) found that the optical continuum slope changed from -2 to 0 over a period of just six months between July 1996 and January 1997. The SED of the AGN from the `GALFIT` decomposition has an irregular shape, and the slope between the B, V, and I bands is not smooth, suggesting that the fits are strongly affected by degeneracy between the AGN and compact cluster component. The photometric uncertainties from the `GALFIT` decomposition are quite large ($\sim$ 0.4 mag for point source component and $\sim$ 0.2 mag for the Sérsic component in F814W), and improving this decomposition will require imaging of the NC with higher spatial resolution than what is currently available.

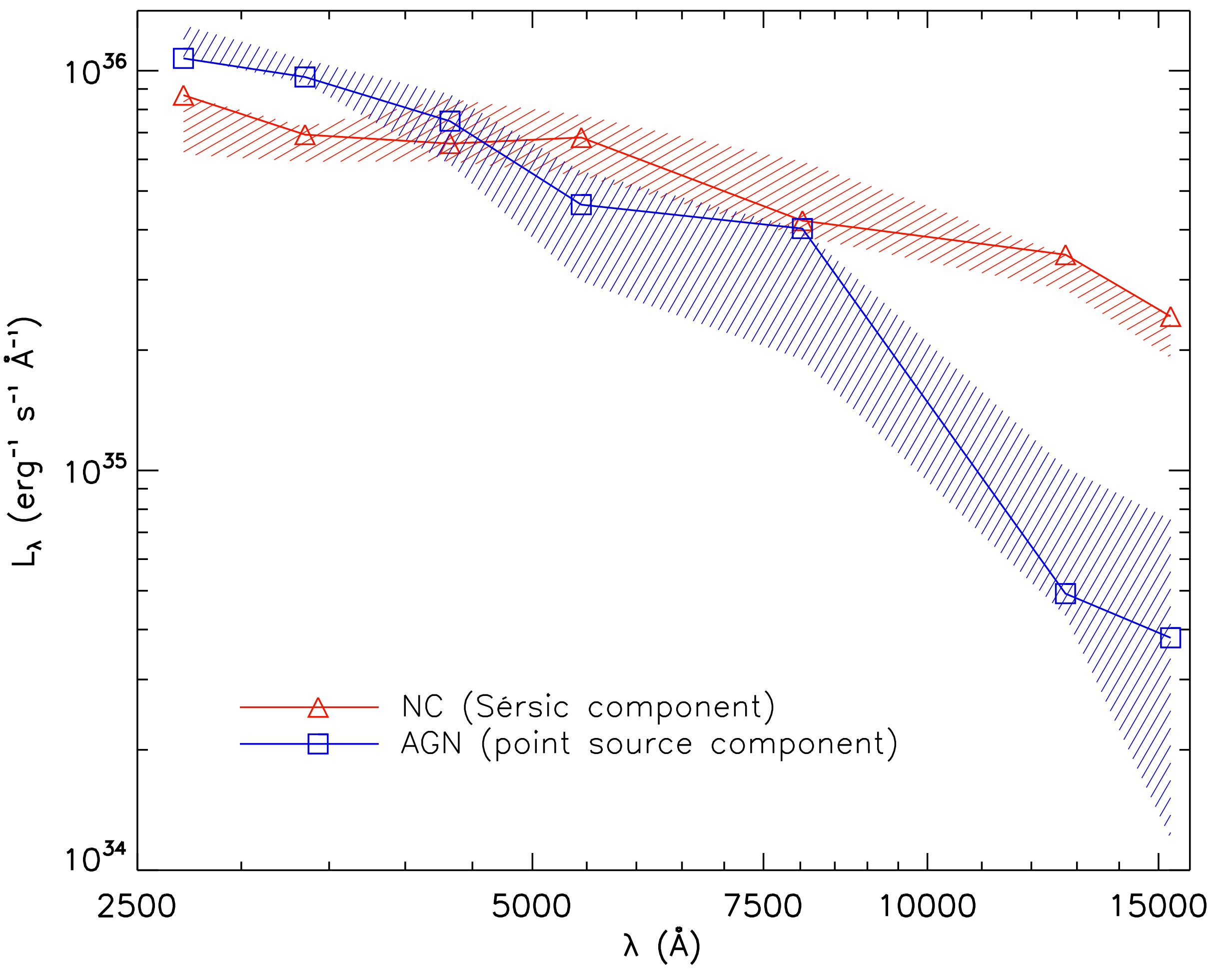

Figure 3.18 SEDs of the individual fit components for NGC 4395. A point source component (shown in blue) was used to model the AGN and a Sérsic component (shown in red) was used to model the NC. The solid lines correspond to the SEDs resulting from fits performed with no constraints. In addition to the fit with no constraints, fits were performed with the effective radius fixed at 4.56 pc and the Sérsic index fixed at 1.42, and with the effective radius fixed at 1.80 pc and the Sérsic index fixed at 3.01. The shaded regions are bounded by the SEDs resulting from taking the minimum and maximum magnitude of all three fits in each band.

3.3.10 NGC 7793

At a distance of 3.4 Mpc (Pietrzyński et al., 2010), the nearly face-on galaxy NGC 7793 is one of the brightest galaxies in the Sculptor Group. Walcher et al. (2005) measured a stellar velocity dispersion of 24.6 km s^{-1} and a mass of $10^{6.89}$ $M_{\odot}$ for the NC. NGC 7793 was included in the Böker et al. (2002) *HST*/WFPC2 NC imaging survey, where an I-band absolute magnitude of -13.64 ± 0.03 mag was measured. Correcting for the slightly different distances used, this corresponds to a WFC3 F814W absolute magnitude of -13.61 ± 0.03 mag, which is in very good agreement with our measurement of $-13.59^{+0.06}_{-0.05}$ mag. We fit a flat sky to the host galaxy and a single Sérsic component to the cluster in each band. The cluster has a larger extent in the UV than the IR, with an effective radius that monotonically decreases from $12.45^{+1.83}_{-1.83}$ pc in F275W to $7.94^{+2.73}_{-1.02}$ pc in F153M. The color gradient is obvious from inspection of the color composite image of the cluster shown in Figure 2.3. The Sérsic index monotonically increases from $1.39^{+0.24}_{-0.27}$ in F275W to $3.29^{+1.18}_{-0.56}$ in F153M. Although a single Sérsic component gives a reasonable fit in all bands, a closer inspection of the images reveals a ring-like gap in the stellar density, which is particularly prominent in the UV bands. This structure can also be seen in the residuals of the F814W fit (Figure 3.2).

Chapter 4

Analysis of Stellar Population Properties

4.1 Global SED Fits

Stellar population modeling is a well-established method of interpreting the integrated light observed from unresolved collections of stars, where the objective is to determine the properties of the stars that give rise to the observed emission. Fitting model SEDs that cover a wide range in parameter space to observed SEDs is the most common technique for deriving estimates of the stellar mass, star formation history, metallicity, and dust extinction of galaxies and other stellar systems. High-resolution spectra as well as broadband SEDs constructed from multi-band imaging have been widely used for stellar population modeling.

The parameters inferred from stellar population modeling are highly sensitive to the assumptions that go into producing the model SEDs. For instance, models may vary in the assumed initial mass function (IMF), stellar evolutionary tracks, and the dispersion of stellar ages within the model (e.g., single-burst, multiple-burst, exponentially declining star formation histories). In addition, different models vary in their treatment of thermally pulsating asymptotic branch stars, whose contribution is likely significant, but highly uncertain (Conroy et al., 2009). All of these factors can impact the observable parameters inferred from SED fitting. For example, Mobasher et al. (2015) found that the differences between various widely used population synthesis codes affect stellar mass estimates of galaxies by ~ 0.2 dex.

Even if a single population synthesis code is used, stellar population synthesis modeling can lead to significant degeneracies, as various combinations of parameters can lead to equally good fits to the observed SED. A well-known example is the age-metallicity degeneracy, which arises because the optical colors of young, metal-rich stellar populations are indistinguishable from old, metal-poor populations (Worthey, 1994). This degeneracy can be partially broken with the addition of near-UV and far-UV photometry (Kaviraj et al., 2007). Similarly, the degeneracy between age and dust extinction can be broken with observations that extend into the IR (Pozzetti & Mannucci, 2000). Both of these degeneracies can in turn affect mass estimates, because the mass-to-light ratio (M/L) of a stellar population strongly depends on its age. Broad wavelength coverage is therefore crucial for breaking degeneracies and more accurately measuring stellar masses and ages.

We used the broadband SEDs constructed from *HST*/WFC3 imaging to perform stellar population synthesis modeling on our sample of NCs. This section details the SED fitting method we have developed, and presents the basic results of this analysis.

We used the broadband SEDs constructed from *HST* imaging to perform stellar population synthesis modeling on our sample of NCs. This section details the SED fitting method we have developed, and presents the basic results of this analysis.

4.1.1 Global SED Fitting Method

NCs are not generally well described by single-age models, as shown in spectroscopic studies by Sarzi et al. (2005), Walcher et al. (2006), Rossa et al. (2006), and Seth et al. (2006). These studies have taken advantage of the fact that an arbitrarily complex star formation history can be modeled as a superposition of instantaneous bursts of star formation. We adopt a similar approach, and model each NC using a linear combination of Bruzual & Charlot (2003a, BC03 hereafter) simple stellar population (SSP) templates with a Calzetti et al. (2000) extinction curve applied (in order to account for internal reddening). Deriving constraints on the internal reddening of the NCs is possible because our WFC3 observations extend into the near-IR.

The model SEDs are constructed from a set of 300 BC03 SSP templates, each of which has a single, instantaneous-burst star formation history. This set contains templates with 50 log-spaced ages ranging from 1 Myr to the age of the Universe (13.7 Gyr) and 6 different metallicities, $Z = 0.0001, 0.0004, 0.004, 0.008, 0.02$, and 0.05. The SSP templates were computed using the Padova 1994 evolutionary tracks, assuming a Chabrier (2003) IMF with a lower mass cutoff of 0.1 $M_{\odot}$ and an upper mass cutoff of 100 $M_{\odot}$. The subset of solar-metallicity ($Z = 0.02$) templates is shown at full resolution in Figure 4.1, along with the throughput curves of our seven *HST* filters. In order to make direct comparisons with the observed SEDs, we simulated WFC3 observations of the entire set of 300 BC03 SSP templates using `Calcphot`, constructing broadband SEDs with seven photometric data points.

Fitting weighted sums of SSP model spectra to the observed spectra of NCs is an effective way to quantify their stellar population properties, but this requires that the models have enough SSP components to describe the complex star formation histories of NCs. The observed SEDs of our sample of NCs contain only seven photometric data points, which limits the number of SSP components that we can include in our models. Consequently,

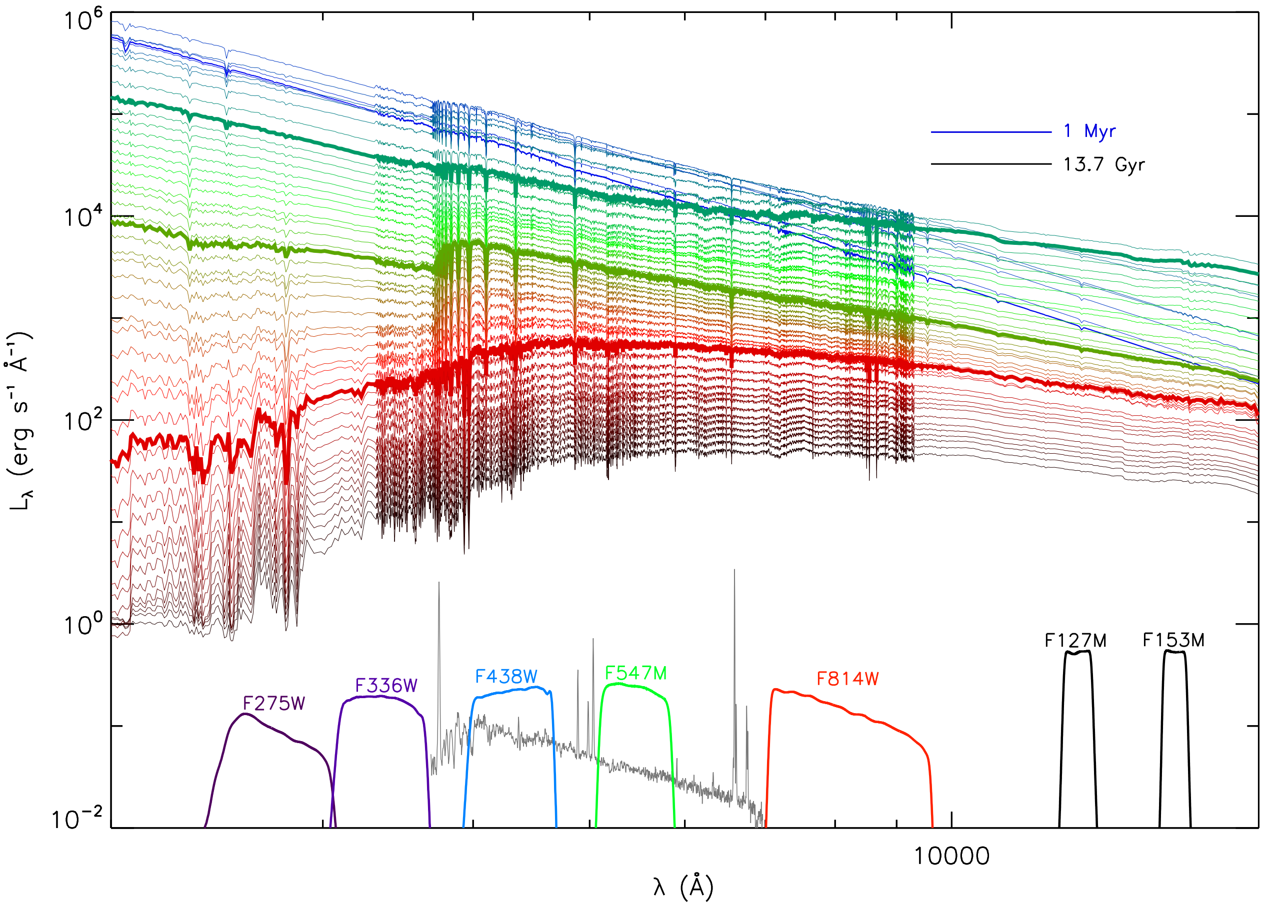

Figure 4.1 Spectra of SSPs with solar metallicity and total stellar mass $1M_\odot$. SSP ages range from 1 Myr to 13.7 Gyr in 50 log-spaced time steps, and the 10 Myr, 100 Myr, and 1 Gyr models are shown in bold. In gray, we plot an optical spectrum of the starburst galaxy NGC 3395 obtained by Moustakas & Kennicutt (2006) to show that our WFC3 filters avoid strong emission lines. Also included in the plot are throughput curves of the seven *HST* filters.

the precision with which we can infer the star formation histories of the NCs limited. We only attempt to describe NC star formation histories with coarse time resolution, because our models must account for the possibility of ongoing star formation over cosmological timescales with a small number of free parameters. The BC03 SSP templates were divided into four log-spaced age bins: 1–10 Myr, 10–100 Myr, 100 Myr–1 Gyr, and 1–13.7 Gyr. We model each NC using a linear combination of four SSP templates, one randomly drawn from each age bin, with a Calzetti et al. (2000) reddening curve applied. The models have five free parameters: the linear weight applied to each SSP template (i.e., the stellar mass in each age bin) and the amount of internal reddening. Optimizing these parameters via SED fitting provides a rough account of the star formation history, as well as the total stellar mass of each NC.

We adopt a Monte Carlo method to determine the range of weights and reddening combinations that are consistent with the data. In each realization of the fit, one SSP template is randomly drawn from each of the four age bins to construct the model SED. A χ^2 fit to the data is performed using the penalized pixel-fitting code (*pPXF*; Cappellari & Emsellem, 2004), which computes the best-fit weight for each SSP template and the best-fit internal reddening. The total stellar mass is simply the sum of the weights. The value of χ^2, the four best-fit weights, w_1, w_2, w_3, and w_4, and the best-fit internal reddening, $E(B-V)$, are all recorded. This process is repeated for 10^5 realizations, which allows us to sample the individual likelihood distributions of w_1, w_2, w_3, w_4, and $E(B-V)$.

The fiducial value and uncertainty of a given parameter θ is determined from its cumulative likelihood distribution, which is computed as follows. First, the best-fit values of θ from the 10^5 Monte Carlo realizations of the fit are sorted in ascending order $(\theta_1, \theta_2, ...\theta_k, ...)$. The list of unnormalized likelihoods associated with these parameter values is given by

$(e^{-\chi_1^2/2}, e^{-\chi_2^2/2}, ...e^{-\chi_k^2/2}, ...)$. Dividing this list by a normalizing constant,

$$N \equiv \sum_{i=1}^{10^5} e^{-\chi_i^2/2}, \tag{4.1}$$

results in the likelihood distribution for θ. The *cumulative* likelihood distribution, $F(< \theta_k)$, is then computed by summing over the first k elements of the list of likelihoods.

$$F(< \theta_k) = \frac{1}{N} \sum_{i=1}^{k} e^{-\chi_i^2/2} \tag{4.2}$$

Our fiducial estimate of a given parameter of interest (θ) is taken to be the median of the cumulative likelihood distribution, or the value of θ where $F(< \theta) = 0.5$. The 1σ confidence interval, $(\theta_{\rm lower}, \theta_{\rm upper})$, is the range that encompasses 68% of the likelihood, which corresponds to $F(< \theta_{\rm lower}) = 0.16$ and $F(< \theta_{\rm upper}) = 0.84$. For illustrative purposes, we plot the cumulative likelihood distribution of the total stellar mass of IC 342's nuclear cluster in Figure 4.2.

In order to simplify our models and to mitigate degeneracies between age and metallicity, we assumed a single, uniform metallicity for each NC. To determine the optimal metallicity for each cluster, we applied the SED fitting method described above at a fixed metallicity for $Z = 0.0001, 0.0004, 0.004, 0.008, 0.02$, and 0.05. We performed 10^5 realizations of the fit at each value of Z. The metallicity that resulted in the smallest median value of χ^2 among the 10^5 realizations of the fit was selected. Two NCs in our sample, NGC 300 and NGC 7793, were also included in the sample of Walcher et al. (2006), wherein NC metallicities were determined spectroscopically. For NGC 7793, our assumed metallicity ($Z = 0.02$) is slightly higher than the value of $Z = 0.008$ derived by Walcher et al. (2006), while for NGC 300, our assumed metallicity of $Z = 0.004$ is in agreement. The mean for our sample is $\langle Z \rangle = 0.018$, which is consistent with spectroscopic studies of the nuclei of late-type galaxies by Walcher et al. (2006), who found $\langle Z \rangle = 0.015$ for a sample of nine NCs, and Rossa et al.

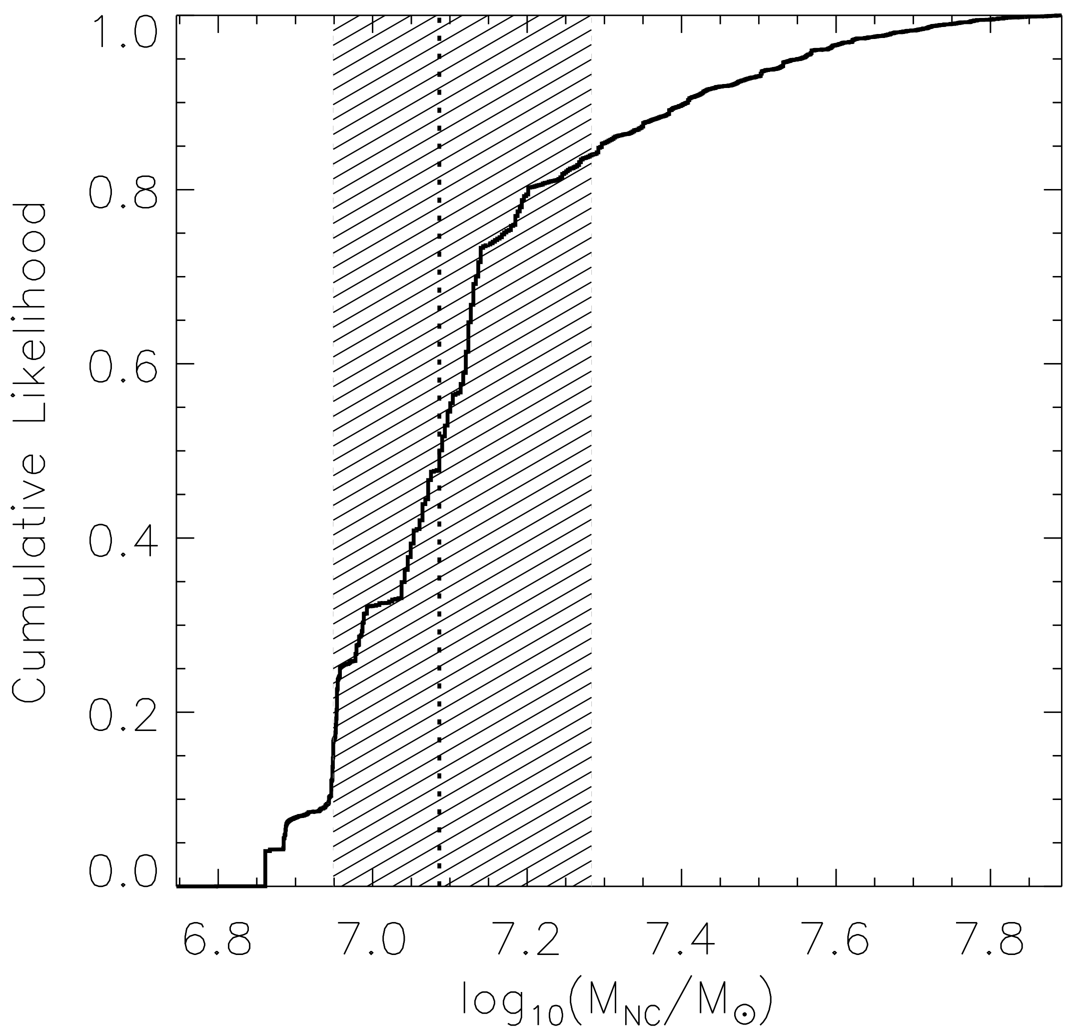

Figure 4.2 Cumulative likelihood distribution of the total stellar mass for IC 342. The shaded region denotes the 1σ confidence interval, and the vertical dashed line denotes the median of the likelihood distribution.

(2006), who found $\langle Z \rangle = 0.018$ for a sample of 25 NCs.

The broad agreement with previous spectroscopic studies gives us confidence that our method for assigning a metallicity to each NC is robust. Nonetheless, the stellar mass estimates we derive will depend on the assumed metallicity. In order to assess this effect, we computed the likelihood-weighted mean, $\langle M \rangle$, and dispersion, σ_M, of the mass estimates we derived assuming $Z = 0.0001, 0.0004, 0.004, 0.008, 0.02$, and 0.05. The average fractional dispersion, $\sigma_M / \langle M \rangle$, is 0.45 for the entire sample. If extremely metal poor populations are excluded, and the metallicity is restricted to the range $Z = 0.004 - 0.05$, $\sigma_M / \langle M \rangle$ falls to 0.25. For comparison, the average fractional uncertainty on the total stellar mass is 0.55 from our SED fitting procedure. The assumed metallicity only has a sub-dominant effect on our stellar mass estimates, and we therefore do not include it in our error budget.

Our models assume that none of the mass lost in supernovae explosions or stellar winds is reprocessed into new stars in the NC. Although this is an oversimplification, it makes the problem of fitting multi-age models to SEDs with only seven photometric data points more tractable. Moreover, it is unlikely to have much of an effect on our mass estimates. In a comprehensive study of the uncertainties associated with measuring observable parameters from SED fitting, Mobasher et al. (2015) showed that stellar mass estimates of galaxies only weakly depend on the specific treatment of stellar mass recycling (e.g., ignoring stellar mass recycling, using the instantaneous recycling approximation, or using more detailed models of stellar mass recycling).

The Appendix describes a series of tests we performed to determine the optimal number of age bins to use in our models and to assess the limitations of the SED fitting method. In brief, our method produces mass, age, and reddening estimates with little bias for mock SEDs typical of NCs containing multi-age populations. Our method fails to reliably recover the correct stellar mass and age when the input SED is completely dominated by a young population, because the fits become highly insensitive to the amount of mass in the oldest age bin. However, it is unlikely that any of the NCs in our sample are affected by this failure mode because their colors are not sufficiently blue to be dominated by such young populations.

4.1.2 Results

We performed a fit to the SED of each cluster using the method outlined in Section 4.1.1. The observed and best-fit model SEDs are shown in Figure 4.3. Parameters derived from the global SED fits are shown in Table 4.1. We quote the assumed metallicity, the mass, the I-band mass-to-light ratio, and the internal reddening for each cluster. To quantify the NC ages, we used the average of the logarithm of the SSP ages that compose the model. This statistic is $\langle \log_{10}\tau \rangle$, where τ is the SSP age in years. Since the SSPs in our models span over four orders of magnitude in age, $\langle \log_{10}\tau \rangle$ more clearly reflects the presence of young populations than $\log_{10}\langle \tau \rangle$, as noted by Rossa et al. (2006). Subscripts are used to denote the weighting used in the calculation of $\langle \log_{10}\tau \rangle$. For instance, $\langle \log_{10}\tau \rangle_{\mathrm{M}}$ indicates a mass weighted average, while $\langle \log_{10}\tau \rangle_{\mathrm{L}_B}$ indicates a B-band luminosity weighted average. Luminosity-weighted age estimates are younger than mass-weighted age estimates due to the lower M/L of younger populations. For example, M/L_B increases from 0.001 to 6.7 as a solar-metallicity SSP evolves from 1 Myr to 13.7 Gyr in age. A more detailed discussion of the mix of populations present in the NCs is given in the .

The clusters in our sample span over an order of magnitude in stellar mass, with a mean of $\overline{\log_{10}(M/M_{\odot})} = 6.44$ and scatter of 0.47 dex (the bar denotes a sample average). Since the SEDs were corrected for reddening within the Milky Way, the $E(B-V)$ values derived from the fits represent the internal reddening due to dust within each galaxy. Of the nine clusters in the sample, seven have $E(B-V) < 0.1$, and four have $E(B-V)$ consistent with zero. In contrast, IC 342 and NGC 2976 are highly reddened, with internal reddenings of

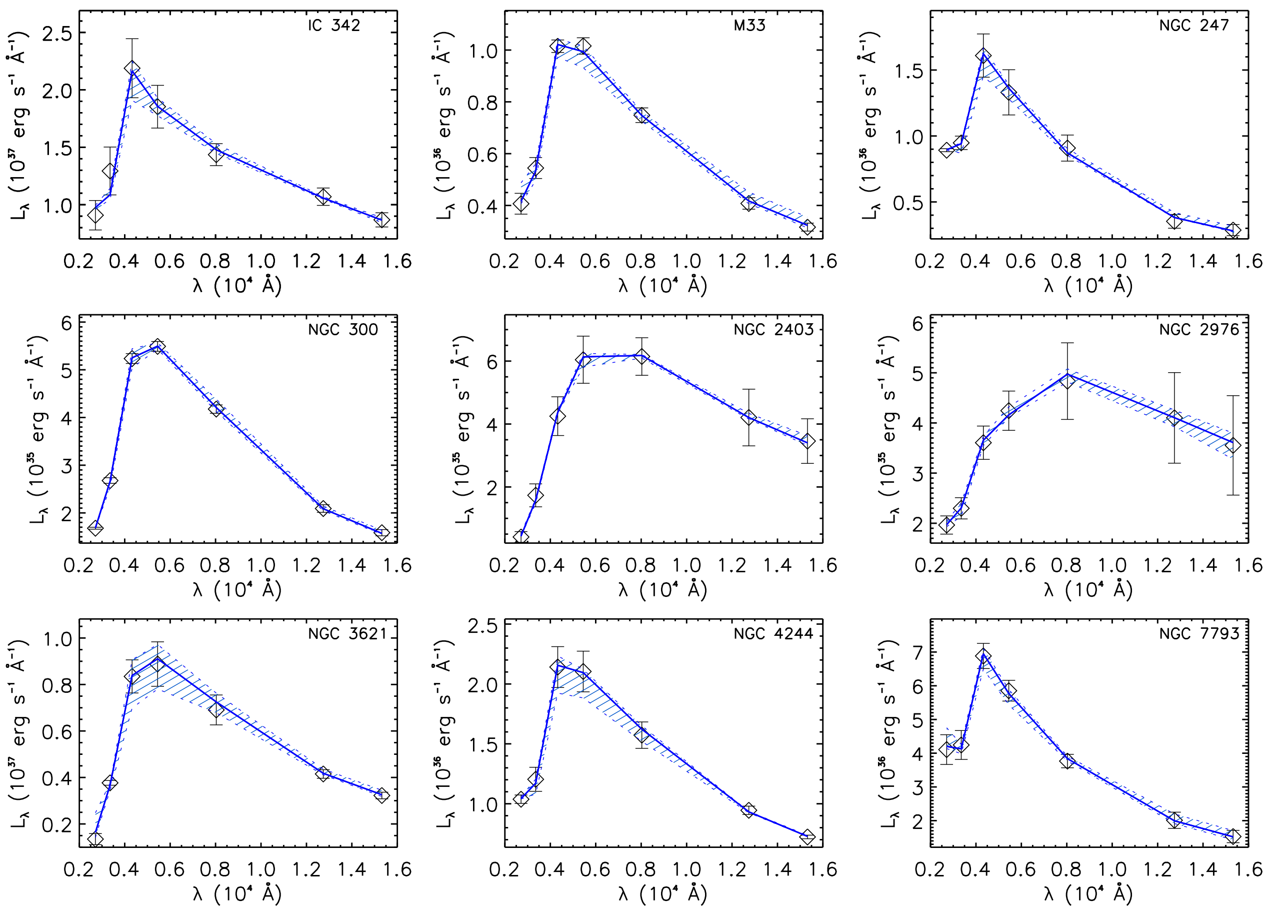

Figure 4.3 Best-fit model SEDs are shown with a solid blue line and the associated 1σ confidence intervals are indicated by the blue shaded regions. The diamond points and error bars denote the observed photometric SEDs used in the fits, which have had Milky Way extinction removed.

Table 4.1. Parameters Derived From Global SED Fits

Object (1)	Z (2)	$M_{\rm NC}$ ($M_\odot$) (3)	M/L_I ($M_\odot/L_{I,\odot}$) (4)	$E(B-V)$ (5)	$\langle\log_{10}\tau\rangle_{\rm M}$ (6)	$\langle\log_{10}\tau\rangle_{{\rm L}_B}$ (7)
IC 342	0.05	$1.22^{+0.70}_{-0.33} \times 10^7$	$0.18^{+0.10}_{-0.05}$	$0.24^{+0.07}_{-0.08}$	$8.63^{+0.45}_{-0.39}$	$8.29^{+0.23}_{-0.14}$
M33	0.02	$1.30^{+1.07}_{-0.39} \times 10^6$	$0.56^{+0.46}_{-0.17}$	$0.00^{+0.01}_{-0.00}$	$9.40^{+0.37}_{-0.27}$	$9.08^{+0.11}_{-0.07}$
NGC 247	0.004	$1.25^{+0.79}_{-0.44} \times 10^6$	$0.44^{+0.28}_{-0.16}$	$0.00^{+0.00}_{-0.00}$	$9.46^{+0.38}_{-0.31}$	$9.00^{+0.09}_{-0.08}$
NGC 300	0.004	$9.10^{+5.80}_{-3.09} \times 10^5$	$0.67^{+0.42}_{-0.23}$	$0.03^{+0.02}_{-0.03}$	$9.54^{+0.34}_{-0.25}$	$9.40^{+0.23}_{-0.17}$
NGC 2403	0.02	$2.31^{+1.39}_{-0.94} \times 10^6$	$1.05^{+0.63}_{-0.43}$	$0.08^{+0.13}_{-0.06}$	$9.63^{+0.34}_{-0.42}$	$9.63^{+0.33}_{-0.42}$
NGC 2976	0.008	$7.99^{+5.41}_{-3.77} \times 10^5$	$0.13^{+0.09}_{-0.06}$	$0.83^{+0.08}_{-0.15}$	$8.33^{+0.90}_{-0.69}$	$7.32^{+0.31}_{-0.29}$
NGC 3621	0.02	$1.36^{+1.24}_{-0.57} \times 10^7$	$0.63^{+0.58}_{-0.27}$	$0.00^{+0.03}_{-0.00}$	$9.39^{+0.44}_{-0.26}$	$9.26^{+0.08}_{-0.14}$
NGC 4244	0.02	$3.36^{+2.79}_{-1.20} \times 10^6$	$0.67^{+0.56}_{-0.24}$	$0.01^{+0.06}_{-0.01}$	$9.51^{+0.38}_{-0.37}$	$9.08^{+0.13}_{-0.21}$
NGC 7793	0.02	$5.60^{+4.70}_{-2.30} \times 10^6$	$0.48^{+0.40}_{-0.20}$	$0.00^{+0.02}_{-0.00}$	$9.40^{+0.41}_{-0.35}$	$8.79^{+0.06}_{-0.08}$

Note. — Col. (1): Galaxy name. Col. (2): Assumed metallicity. Cols. (3) and (4): Best-fit stellar mass and I-band mass-to-light ratio. Mass-to-light ratios are corrected for internal extinction within the cluster. Col. (5): Best-fit internal reddening. Cols. (6) and (7): Mass-weighted and B-band luminosity-weighted average of $\log_{10}(\tau)$, where τ is the population age in years.

$E(B-V) = 0.24^{+0.07}_{-0.08}$ and $E(B-V) = 0.83^{+0.08}_{-0.15}$, respectively. In addition to being highly reddened, IC 342 and NGC 2976 are also considerably younger than the other clusters in the sample, and are the only clusters in the sample with $\langle \log_{10}\tau \rangle_{\mathrm{M}} < 9$.

To check the robustness of the exceptionally large reddening value derived for NGC 2976, we repeated the SED fit *without* first applying a correction for Galactic reddening, and obtained $M = 7.97^{+5.03}_{-3.84} \times 10^5 M_\odot$, $E(B-V) = 0.91^{+0.09}_{-0.17}$, $\langle \log_{10}\tau \rangle_{\mathrm{M}} = 8.24^{+0.96}_{-0.68}$, $\langle \log_{10}\tau \rangle_{\mathrm{L}_B} = 7.16^{+0.36}_{-0.22}$. The mass and age are consistent with our original results, while the enhancement in reddening, $\Delta E(B-V) = 0.08$, is consistent with the foreground reddening (0.064), indicating that the fits are in fact sensitive to the true internal reddening.

Star Formation Histories

The star formation histories of the NCs were inferred from the weights applied to the SSP templates in the best-fit models. We computed the average star formation rate within each of the four broad age bins from which SSP templates were drawn (1–10 Myr, 10–100 Myr, 100 Myr–1 Gyr, 1–13.7 Gyr). The fiducial estimate for the weight in a given age bin corresponds to the median of the likelihood distribution which is sampled in the 10^5 Monte Carlo realizations of the fit. The average star formation rate is then computed by dividing this weight by the width of the age bin. Similarly, the corresponding 1σ confidence interval is the range of weights that encompasses 68% of the likelihood, divided by the width of the age bin. The star formation rate as a function of time for each cluster is displayed in Figure 4.4. The horizontal dashed lines in this figure show the star formation rate averaged over the Hubble time ($t_{\mathrm{H}} = 13.7$ Gyr), which is simply $M_{\mathrm{NC}}/t_{\mathrm{H}}$. None of the clusters are adequately described by a single, constant star formation rate over cosmic time.

The star formation histories we infer are generally extended and not consistent with a single burst of star formation. With the exception of NGC 2403, all of the clusters in the sample have nonzero star formation rates in at least two age bins. Nonzero star formation rates in multiple age bins generally indicate repeated bursts of star formation throughout a cluster's lifetime; however, a single declining burst can also lead to nonzero star formation rates in two neighboring age bins, provided that the burst straddles both age bins in time. Because we have divided the SSP templates into 4 discrete age bins, our method is not sensitive to multiple bursts of star formation that may occur within a single age bin. For example, it is entirely possible that multiple bursts occurred between 1 and 13.7 Gyr ago in the nucleus of NGC 2403, but no additional star formation has occurred since then. Our age resolution is simply too coarse to determine whether this is the case. However, there is good reason to think that multiple, discrete bursts do occur within our broad age bins. Based on the age of the youngest burst in 10 NCs in late-type galaxies derived from stellar population synthesis fits to Very Large Telescope/Ultraviolet and Visual Echelle Spectrograph (VLT/UVES) spectra, Walcher et al. (2006) found that a typical NC has experienced 25 bursts throughout its lifetime, with an average of $1.6 \times 10^5 M_\odot$ in new stars being formed in each burst. The nuclei of IC 342 and NGC 2976 have undergone significant star formation in the last 100 Myr, so it is likely that multiple bursts have occurred within the two broadest age bins (100 Myr-1 Gyr and 1-13.7 Gyr), generally speaking. The peaks in star formation rate in Figure 4.4, particularly in the broadest age bins, should therefore not be interpreted as discrete bursts of star formation, but rather an average over multiple bursts.

NGC 2976 is the only cluster in the sample that has undergone any significant star formation in the last 10 Myr. As discussed in Chapter 3, the nucleus of NGC 2976 has a complex morphology and contains a compact blue component (see Figure 4.5), which is clearly driving the fit towards younger ages. The long-slit spectrum of the nucleus presented by Lira et al. (2007) contains strong nebular emission lines. Based on line ratio measurements, they classified the nucleus as a star forming region, not an AGN. This is consistent with the elevated star formation rate that we measure in the 1–10 Myr age bin, and suggests that our models

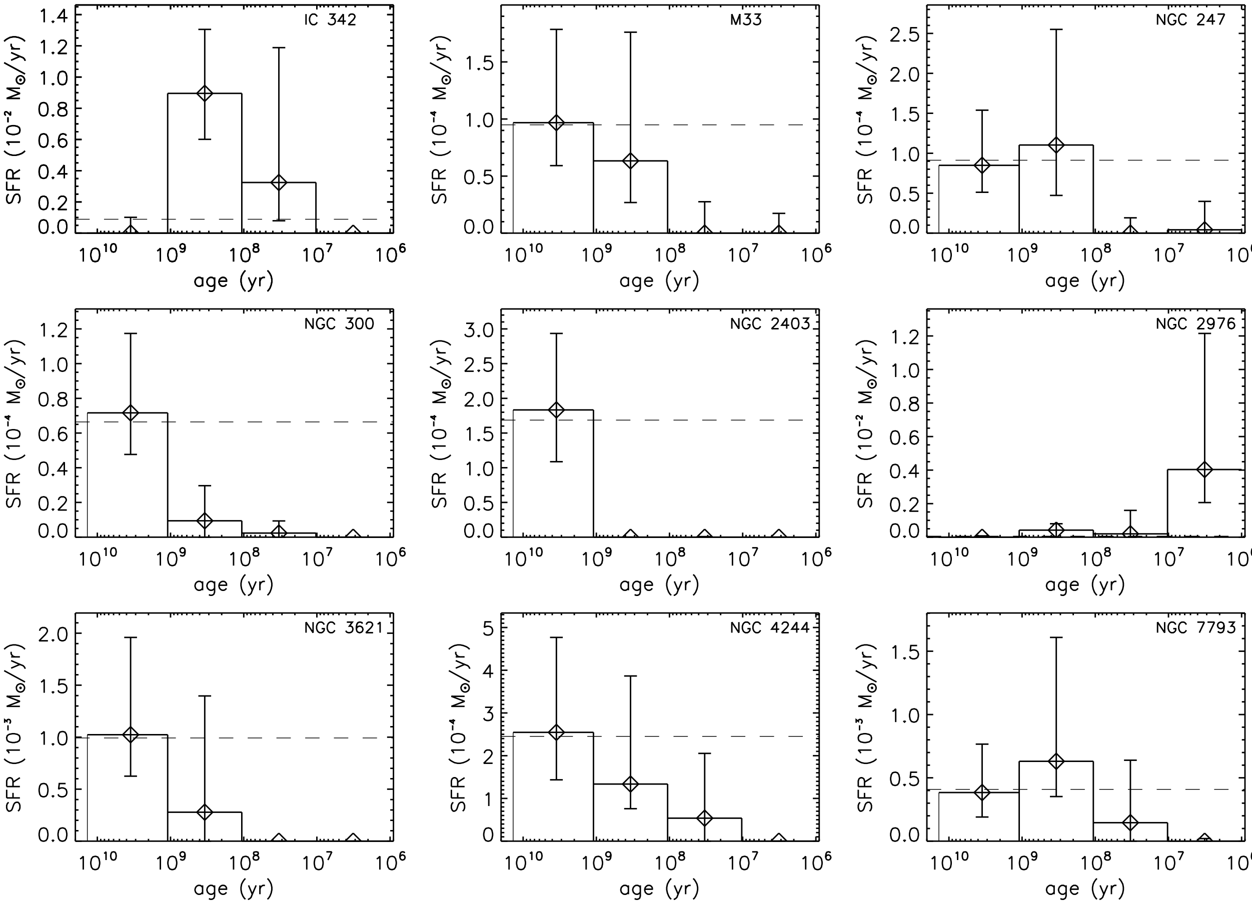

Figure 4.4 Average star formation rate in each age bin. The horizontal dashed line shows the average star formation rate over the age of the Universe (i.e., the total mass divided by 13.7 Gyr).

are correct. We also note that the WFC3 filters used in our study were selected to avoid strong emission lines.

Table 4.2 shows the fraction of the total present-day mass in each age bin, as well as the fraction of the total B-band luminosity in each age bin. For all clusters in the sample, populations younger than 100 Myr account for less that 15% of the total mass. However, it is important to emphasize that a small contribution to the mass does not necessarily imply a small contribution to the luminosity. That is, young populations with negligible mass fractions can still strongly affect the observed spectral shape of the clusters. A good fit to the data therefore requires that the models allow for multi-age populations and include very young SSPs.

On average, populations younger than 100 Myr only contribute 1.8% of the total stellar mass, but 10.4% of the total B-band luminosity. These averages are highly skewed by the presence of the exceptionally young nucleus of NGC 2976 in the sample. Excluding this object, these averages are 0.5% and 3.7%, respectively. For comparison, populations younger than 100 Myr would constitute only 0.73% of the total stellar mass in a cluster that has been forming stars at a constant rate throughout the lifetime of the universe.

As a consistency check, we compared results from Walcher et al. (2006) to the fractional weights derived from our SED fits. In this study, linear combinations of a set of 14 BC03 SSP templates were fit to VLT/UVES spectra of a sample of nine nuclear clusters residing in late-type galaxies. This sample contains two objects that overlap with our sample, NGC 300 and NGC 7793. In order to make a proper comparison of the weights, we rebinned the 14 SSP templates used in Walcher et al. (2006) to the four broad age bins used in our analysis. The fractional mass weights derived by Walcher et al. (2006) for NGC 300 and NGC 7793 are quoted in Table 4.2. The weights are in good agreement with our results.

Table 4.2: The weights quoted in this table are the fraction of the total present-day mass formed in each broad age bin, and the fraction of the total B-band luminosity contributed by SSPs in each age bin. Fractional mass weights derived by Walcher et al. (2006) for NGC 300 and NGC 7793 are shown in parenthesis.

	fractional mass weights				fractinal B-band luminosity weights			
Object	1–10 Myr	10–100 Myr	100 Myr–1 Gyr	1–13.7 Gyr	1–10 Myr	10–100 Myr	100 Myr–1 Gyr	1–13.7 Gyr
IC 342	0.0000	0.0327	0.9673	0.0000	0.0000	0.1305	0.8695	0.0000
M33	0.0000	0.0003	0.0542	0.9454	0.0021	0.0117	0.3711	0.6151
NGC 247	0.0000	0.0000	0.0970	0.9029	0.0026	0.0000	0.5053	0.4921
NGC 300	0.0000	0.0003	0.0124	0.9874	0.0000	0.0118	0.1323	0.8559
	(0.000)	(0.000)	(0.030)	(0.970)	...	...	...	...
NGC 2403	0.0000	0.0000	0.0000	1.0000	0.0000	0.0000	0.0000	1.0000
NGC 2976	0.0833	0.0372	0.8795	0.0000	0.5744	0.0568	0.3688	0.0000
NGC 3621	0.0000	0.0000	0.0249	0.9751	0.0000	0.0000	0.1897	0.8103
NGC 4244	0.0000	0.0016	0.0406	0.9578	0.0000	0.0624	0.3516	0.5860
NGC 7793	0.0000	0.0027	0.1163	0.8809	0.0000	0.0731	0.5793	0.3476
	(0.000)	(0.012)	(0.226)	(0.762)	...	...	...	...

Comparison With Previous Dynamical Mass Estimates

Fitting dynamical models of varying complexity to observed kinematic data is a means to measure the stellar masses of NCs and place constraints on the masses of central black holes residing within them. Six of the clusters in our sample have been the targets of previous dynamical studies, and our stellar mass estimates are generally in good agreement with these studies. Table 4.3 lists the masses and I-band mass-to-light ratios derived in this work for IC 342, M33, NGC 300, NGC 3621, NGC 4244, and NGC 7793, and compares them to results from dynamical studies by Böker et al. (1999), Hartmann et al. (2011), Walcher et al. (2005), and Barth et al. (2009). Böker et al. (1999) adopted a distance of 1.8 Mpc for IC 342 from McCall (1989), and found $M_{\rm NC} = (6.0 \pm 2.4) \times 10^6 M_\odot$ and $M/L_K = 0.05$. We adopt a distance of 3.3 Mpc based on more recent observations of Cepheid variable stars in the disk by Saha et al. (2002). The dynamical mass is proportional to the distance, while the dynamical mass-to-light ratio is inversely proportional to the distance. Correcting for the different adopted distances, the Böker et al. (1999) estimates become $M_{\rm NC} = (1.1 \pm 0.4) \times 10^7 M_\odot$ and $M/L_K = 0.03$. For all other galaxies in Table 4.3, the adopted distances agree within 10%, so we make no correction for the difference. NGC 4244 is the only cluster for which we find a serious disagreement between our mass estimate and a previous dynamical estimate. In this case, the discrepancy in mass estimates is primarily driven by the discrepancy in M/L. For the other clusters, we find good agreement in both the stellar mass and mass-to-light ratio. Since none of the galaxies in Table 4.3 appear to host central black holes with masses comparable to that of the NC, the broad agreement between masses derived from SED fitting and dynamical modeling indicates that our method for estimating the stellar mass is robust.

Table 4.3: Col. (1): Galaxy name. Col. (2): Reference for dynamical mass and mass-to-light ratio. Col. (3): Dynamical mass ratio from previous study. Col. (4): Mass from global SED fits described in this section. Col. (5): Band used for mass-to-light ratio estimates. Col. (6): Mass-to-light ratio from a previous study. Col. (7): Mass-to-light ratio from global SED fits described in this section. For IC 342, the dynamical mass and mass-to-light ratio were corrected for the different distance used in the Böker et al. (1999) study. We used the $H-K$ color of a 500 Myr BC03 SSP spectrum to obtain our estimate of the K-band mass-to-light ratio of IC 342. The mass-to-light ratio of NGC 4244 was re-determined from the JAM model in Hartmann et al. (2011). Dynamical mass and mass-to-light ratio measurements were obtained from the following sources: (a) Böker et al. (1999); (b) Hartmann et al. (2011); (c) Walcher et al. (2005); (d) Barth et al. (2009)

Object (1)	Reference (2)	$M_{\rm NC}$ ($M_\odot$), dynamical (3)	$M_{\rm NC}$ ($M_\odot$), this work (4)	M/L band (5)	M/L, dynamical (6)	M/L, this work (7)
IC 342	a	$(1.1 \pm 0.4) \times 10^7$	$1.22^{+0.70}_{-0.33} \times 10^7$	K	0.03	$0.06^{+0.04}_{-0.02}$
M33	b	$(1.4 \pm 0.2) \times 10^6$	$1.30^{+1.07}_{-0.39} \times 10^6$	$\cdots$	$\cdots$	$0.56^{+0.46}_{-0.17}$
NGC 300	c	$(1.0 \pm 0.4) \times 10^6$	$9.10^{+5.80}_{-3.09} \times 10^5$	I	0.65 ± 0.20	$0.67^{+0.42}_{-0.23}$
NGC 3621	d	$(1-3) \times 10^7$	$1.36^{+1.24}_{-0.57} \times 10^7$	V	1.4	$0.78^{+0.71}_{-0.33}$
NGC 4244	b	$(1.1 \pm 0.2) \times 10^7$	$3.36^{+2.79}_{-1.20} \times 10^6$	I	2.1	$0.67^{+0.56}_{-0.24}$
NGC 7793	c	$(7.8 \pm 2.8) \times 10^6$	$5.60^{+4.70}_{-2.30} \times 10^6$	I	0.64 ± 0.19	$0.48^{+0.40}_{-0.20}$

4.2 Spatially Resolved SED Fits

The technique of SED fitting at each resolution element in a set of images has been widely used to study the spatially resolved properties of galaxies (e.g., Lanyon-Foster et al., 2007; Welikala et al., 2008; Zibetti et al., 2009; Welikala et al., 2009; Wuyts et al., 2012; Hemmati et al., 2014). Although more computationally expensive than SED fitting using the integrated light of galaxies, this method allows for substructures within galaxies to be studied and reduces the uncertainties associated with averaging the star formation history and dust attenuation over an entire galaxy. Such a study has not previously been carried out for a sample of nuclear star clusters; however, our *HST* data set is suitable for this purpose because the NCs are well resolved in the images, as demonstrated in Chapter 3. This section details the techniques we have developed to perform spatially resolved stellar population synthesis modeling on the NCs and presents the basic results of this analysis.

4.2.1 Spatially Resolved SED Fitting Method

For each NC, we constructed a data cube consisting of a stack of seven *HST* images, spanning the near-UV (F275W) to the near-IR (F153M) in wavelength. Before the data cubes can be used for pixel-by-pixel SED fitting, the images must be aligned, cropped, PSF matched, converted to luminosity units, and corrected for Galactic extinction. In this subsection, we explain the step-by-step method we used to construct the data cube for each NC.

First, the seven *HST* images were aligned with each other. Due to a lack of bright point sources that are detectable in every filter, the NCs themselves were used for image alignment. We computed the centroid of the NC in each image, then, in order to make the NC exactly coincide with the central pixel of each image, shifts were applied using the IDL routine `shift_frac2d`. This routine uses a fast Fourier transform method to apply shifts with sub-pixel precision. To verify that the sub-pixel shifts do not compromise the quality of the images, we selected a bright point source in the F275W image of IC 342 and applied 1000 random sub-pixel shifts. We then fit a 2D Gaussian profile to the original image and each of the shifted images. We find that on average, the total flux agrees with within 0.4% between the original and shifted images and the width of the Gaussian agrees within 1.1%.

With typical effective radii well under $1''$, the NCs in our sample only occupy a small fraction of the $20'' \times 20''$ field of view of the MS512C UVIS subarray. In order to reduce computing time and to exclude the outer edges of the images corrupted by the image alignment step, it is necessary to crop the images down to a smaller field of view. To this end, we produced $2'' \times 2''$ (51×51 pixel) image cutouts centered around the NC centroid.

In order to match the PSFs of the images across the wavelength range of the seven *HST* filters, we degraded all of the UVIS images and the F127M images to the resolution of F153M. As explained Chapter 3, 2D models of the *HST* PSFs in each band were generated using version 7.4 of the `TinyTim` software package (Krist, 1993; Krist et al., 2011). PSF matching was achieved by convolving each UVIS and F127M image with a Gaussian broadening kernel. To determine the broadening kernel needed to degrade the UVIS and F127M images to the resolution of the F153M images, we used `GALFIT` to fit a Gaussian profile convolved with each PSF model to the F153M PSF model.

To correct for extinction due to Galactic dust along the line of sight to each galaxy, we used `Calcphot` to simulate *HST* observations of an F star, with and without the Galactic reddening applied. We then multiplied each image by the ratio of the simulated electron counts from the unreddened spectrum to the simulated electron counts from the reddened spectrum. We assumed a single, uniform value for the Galactic reddening along the line of sight to each galaxy, because the field of view of our image cutouts is much smaller than the resolution of the Schlafly & Finkbeiner (2011) dust maps. Finally, we used `Calcphot` to convert the images from units of electron counts to flux units (erg s^{-1} $Å^{-1}$ cm^{-2}), then converted to luminosity units (erg s^{-1} Å^{-1}) using the best available distance measurement for each galaxy.

Each spatial pixel in the data cube contains a broadband SED with 7 data points, and there are 2601 spatial pixels in each data cube. We performed 10^3 Monte Carlo realizations of the fit described in Section 4.1.1 at each spatial pixel. We assumed a single, uniform metallicity for each cluster, adopting the same Z values listed Table 4.1. Reddening is a positive-biased quantity, which can be driven towards unrealistically large values in regions where S/N is low. On the other hand, spatially inhomogeneous dust complexes can not be accurately modeled if the reddening is not allowed to vary between pixels. Due to the presence of dust lanes in the nuclei of IC 342 and NGC 2976, we placed no constraints on the reddening in the pixel-by-pixel SED fits. For the rest of the sample, global best-fit $E(B-V)$ values are all below 0.1 and there are no obvious dust lanes in the image cutouts. For these objects, we fixed the reddening at the value listed in Table 4.1.

4.2.2 Results

The pixel-by-pixel SED fits produce 2D maps of $\langle \log_{10}\tau \rangle_{\rm M}$, $\langle \log_{10}\tau \rangle_{{\rm L}_B}$, and stellar surface density (Σ) at the resolution of the *HST*/WFC3 UVIS channel (004 pix^{-1}), as well as maps of the corresponding 1σ uncertainties. Figure 4.5 shows the resulting maps for each cluster. We also display the reddening maps for IC 342 and NGC 2976 in Figure 4.6. For these objects, the reddening maps trace the dust lanes in the images, indicating that our method is sensitive to spatially inhomogeneous dust complexes in highly reddened regions.

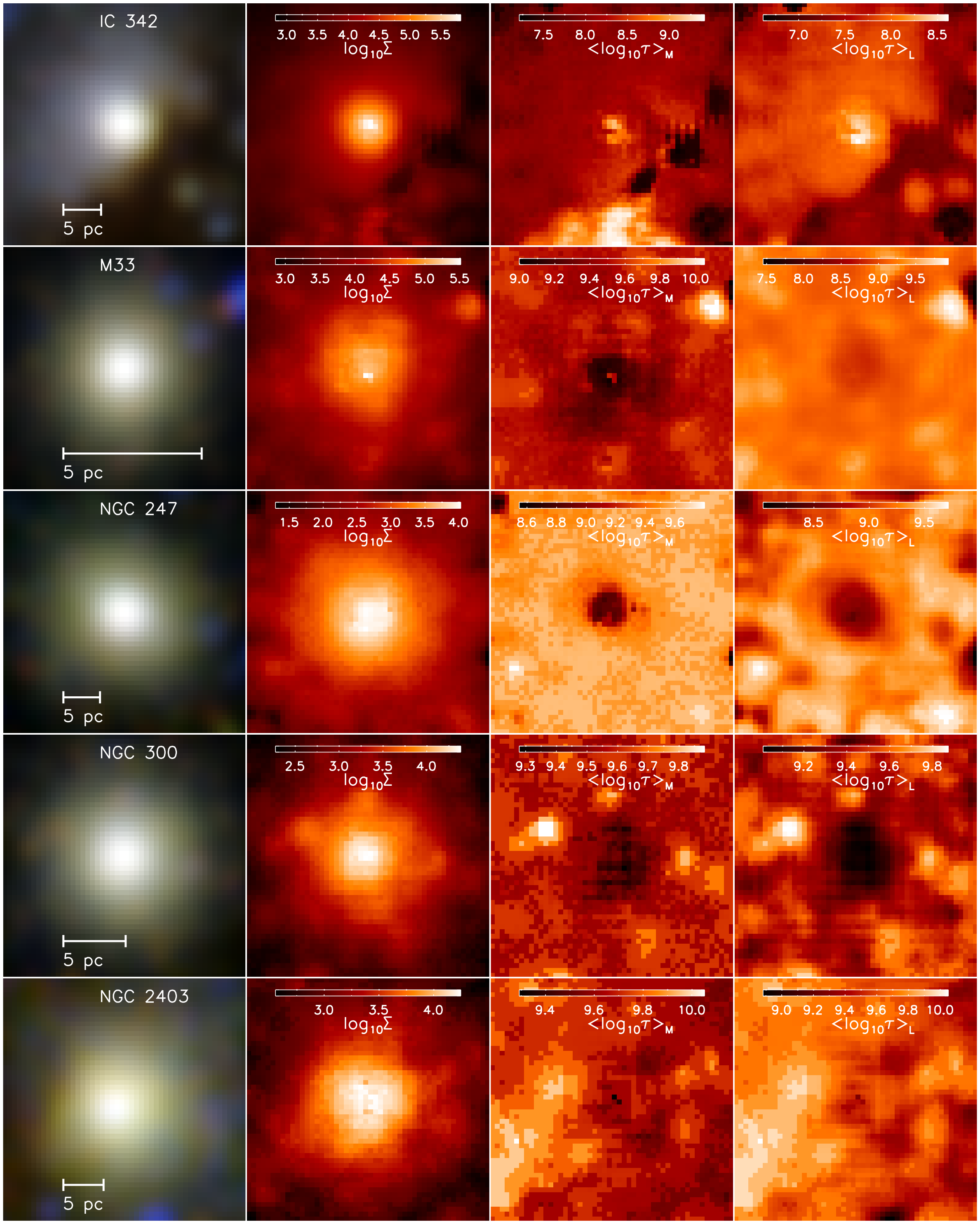

Figure 4.5 Results of pixel-by-pixel SED fits. From left to right, the panels show a color composite image, $\log_{10}\Sigma$, where Σ is the surface density in $M_\odot\ pc^{-2}$, the mass-weighted average value of $\log_{10}\tau$, where τ is the population age in years, and the B-band luminosity-weighted average value of $\log_{10}\tau$. In the color composite images, the F275W, F547M, and F814W filters populate the blue, green and red color channels, respectively. The image cutouts are $2''$ on each side. The scale bars denote a projected distance of 5 pc.

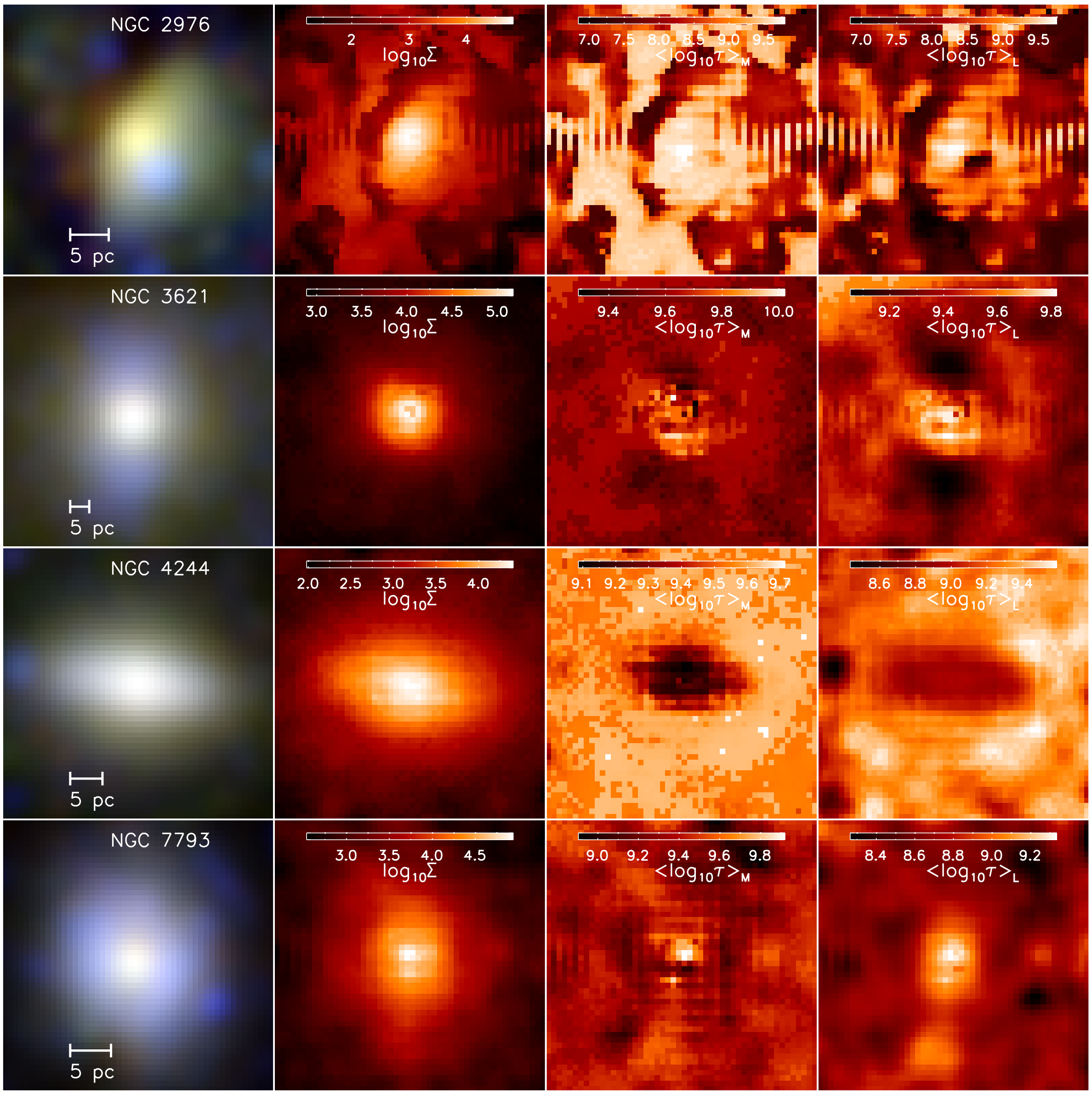

Figure 4.5 Results of pixel-by-pixel SED fits (continued).

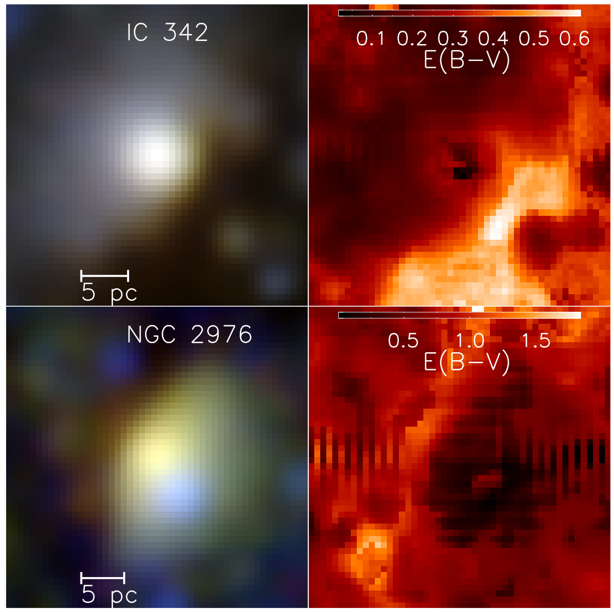

Figure 4.6 The left panels show the color composite images and the right panels show the reddening maps produced by the pixel-by-pixel fits for IC 342 and NGC 2976. For all other objects, the reddening was fixed at the global best-fit value.

Stellar Surface Density Profiles

In this subsection, we outline the procedure for characterizing the 2D surface density profiles as well as the intrinsic 3D density profiles of the clusters. We adopt a method similar to den Brok et al. (2015), first employing `GALFIT` to fit PSF-convolved surface density profiles to the density maps generated in the pixel-by-pixel SED fits, then using code from Cappellari (2002) to create a Multi-Gaussian Expansion (MGE) model of the surface density. The reason that we perform the surface density profile fits in two steps is that GALFIT provides the best way to disentangle the intrinsic surface density profiles from the effects of PSF blurring, while MGE models are more useful for dynamical modeling and can be deprojected analytically.

`GALFIT` is ideal for extracting deconvolved surface brightness profiles from images because the user can input a 2D image of the PSF, allowing non-axisymmetric features of the PSF such as diffraction spikes to be accounted for. PSF models for each *HST* filter were computed using the `TinyTim` software package (see Chapter 3 for model PSFs). We first fit a model surface density profile consisting of a Sérsic component and a flat sky component to the surface density map, enforcing constraints on the Sérsic index ($n < 10$) and the sky level (sky > 0). The flat sky level represents the background mass surface density of the host galaxy disk. We then computed the sum of the residuals over the sum of the input surface density map (f_r). To ensure that most of the stellar mass was accounted for in the `GALFIT` model, we ran the fit again with an additional Sérsic component in cases where $f_r > 0.05$. NGC 4244 required two Sérsic components to achieve $f_r < 0.05$, while all other NCs only required a single Sérsic component. As noted in Chapter 3 and Seth et al. (2008b), the nucleus of NGC 4244 has two distinct morphological components, a red spheroidal structure, and a blue disk structure.

The spatial resolution of the surface density maps produced by the pixel-by-pixel SED fits will ultimately determine the innermost slopes of the best-fit surface density profiles. Since the spatial resolution of the data cubes was degraded to match the F153M PSF, the surface density maps output by the code are at the resolution of F153M. We also produced mass maps at the resolution of F814W by multiplying the M/L_I map by the F814W image. This results in a significantly higher resolution surface density map, as the full width at half maximum (FWHM) is 0196 for the F153M PSF and 0102 for the F814W PSF. We apply the `GALFIT` modeling procedure described in the previous paragraph on both surface density maps.

The shape of the surface density profiles will also depend on the choice of function used to model the NC. In order to assess the model dependence of our surface density profiles, we also fit a modified King profile (Elson, 1999) plus a flat sky level to the surface density maps. Thus, we produce four different models of the stellar surface density of each NC, which we will hereafter refer to as Model 1, Model 2, Model 3, and Model 4. Definitions for these models are given in table 4.4. For illustrative purposes, we plot the radial profiles of Models 1-4 for NGC 300 in Figure 4.7.

Table 4.4. Definitions of Surface Density Models

Name	Definition
Model 1	Sérsic model fit to F153M surface density map
Model 2	King model fit to F153M surface density map
Model 3	Sérsic model fit to F814W surface density map
Model 4	King model fit to F814W surface density map

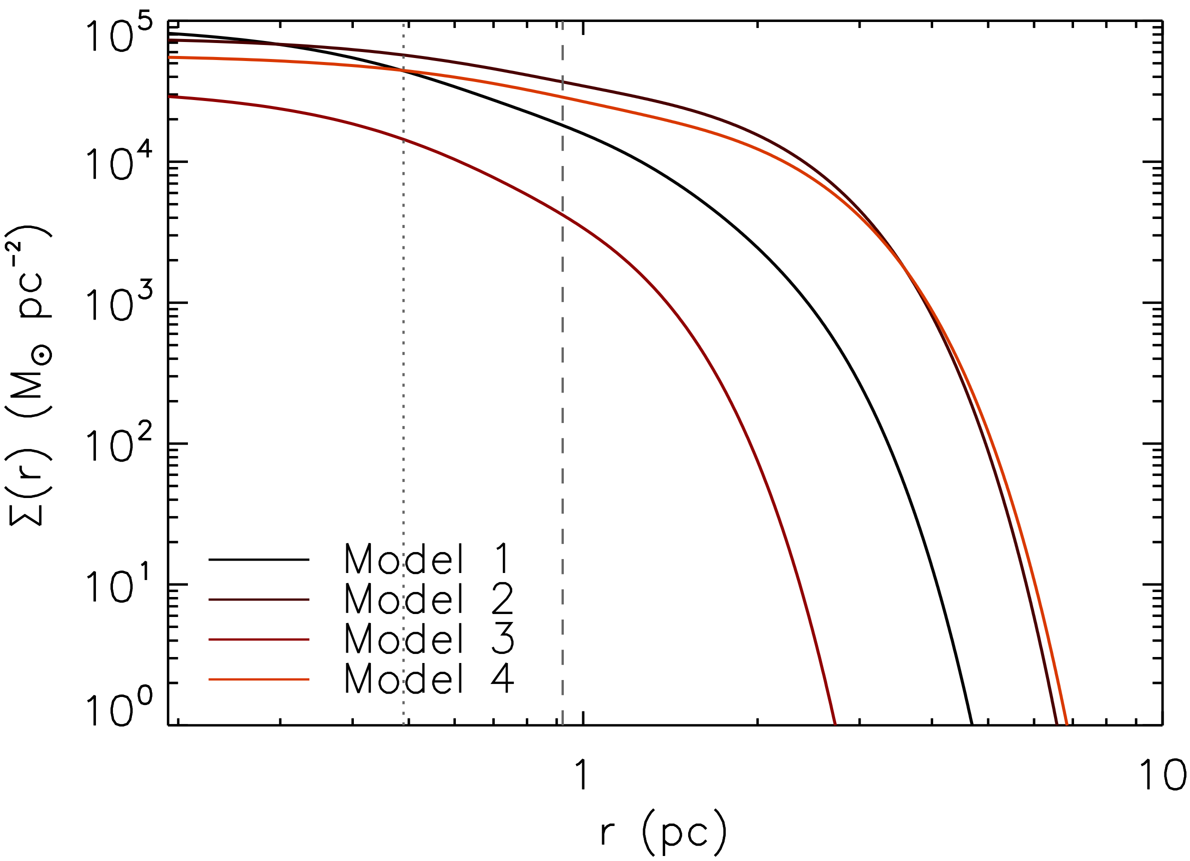

Figure 4.7 Radial profiles of stellar surface density for NGC 300. The short-dashed gray line denotes the half width at half maximum (HWHM) of the F814W PSF, while the long-dashed gray line denotes the HWHM of the F153M PSF.

We adopt the MGE formalism described in Cappellari (2002) in order to express the 2D surface density profiles of the nuclear clusters as a sum of Gaussian components. The reasons for this are twofold. First, Gaussian surface density profiles can be deprojected analytically, which allows us to describe the intrinsic 3D density profiles of the clusters assuming a specific inclination angle and geometry. Second, MGE stellar surface density profiles are needed to construct improved dynamical models of the NCs. With the addition of high-resolution IFU stellar kinematic data, these dynamical models may be able to uncover a previously unseen population of IMBHs within the clusters. MGEs are general enough to describe the surface brightness profile of a galaxy with an arbitrary triaxial shape (Emsellem et al., 1994). In the MGE formalism, (x', y', z') is a set of rectangular coordinates centered on the nuclear cluster, where the y' is the major axis of the Gaussian and the z' axis points along the line-of-sight towards the observer. We assume all Gaussian components have the same center and position angle (i.e., the y' axis is aligned for all components), which allows us to write the surface density as

$$\Sigma(x', y') = \sum_{j=1}^{N} \frac{M_j}{2\pi\sigma_j'^2 q_j'} \exp\left[-\frac{1}{2\sigma_j'^2}\left(x'^2 + \frac{y'^2}{q'^2}\right)\right], \tag{4.3}$$

where N is the total number of Gaussian components in the best-fit model. Each component is assumed to have elliptical geometry, with a total mass M_j, an observed axial ratio q_j', and an observed dispersion σ_j' along the major axis. We used the IDL package `MGE_FIT_SECTORS` to implement the MGE fitting algorithm described by Cappellari (2002), with the nuclear cluster component(s) of the `GALFIT` model as the input image. Since the `GALFIT` models are *not* PSF-convolved (i.e., they are already disentangled from the effects of PSF blurring), we do not convolve the MGE with the PSF before fitting it to the `GALFIT` model. We performed an MGE fit to Models 1-4 for each NC. The Multi-Gaussian Expansion, along with the corresponding `GALFIT` reduced χ^2 of Models 1-4 are listed in Table 4.5.

Table 4.5: Multi-Gaussian Expanisions of the surface density models. The corresponding reduced χ^2 of each `GALFIT` model is also included.

Object	Model 1				Model 2				Model 3				Model 4			
	χ^2	M ($M_\odot$)	$\sigma\prime$ (pc)	$q\prime$	χ^2	M ($M_\odot$)	$\sigma\prime$ (pc)	$q\prime$	χ^2	M ($M_\odot$)	$\sigma\prime$ (pc)	$q\prime$	χ^2	M ($M_\odot$)	$\sigma\prime$ (pc)	$q\prime$
IC 342	0.097	3.13×10^6	0.29	0.93	0.072	7.56×10^5	0.69	1.00	0.133	1.52×10^6	0.24	0.93	0.696	4.35×10^6	0.38	0.87
		2.64×10^5	0.64	0.60		1.90×10^5	1.03	0.75		1.44×10^6	0.58	0.90		6.80×10^6	1.01	0.54
		1.22×10^6	0.79	0.81		1.45×10^6	1.19	0.93		1.48×10^6	1.12	0.86		4.30×10^6	1.92	0.52
		1.22×10^6	1.41	0.76		1.69×10^6	1.76	0.93		1.37×10^6	1.85	0.87		3.15×10^6	3.29	0.51
		1.13×10^6	2.39	0.75		1.96×10^6	2.68	0.92		1.33×10^6	2.86	0.86		1.75×10^6	5.66	0.50
		1.03×10^6	3.92	0.75		1.76×10^6	4.29	0.92		1.39×10^6	4.41	0.86		6.45×10^5	9.29	0.51
		1.13×10^6	6.81	0.75		1.23×10^6	7.19	0.92		1.52×10^6	7.34	0.86		...	...	...
		1.40×10^6	15.31	0.75		...	...	...		1.62×10^6	15.21	0.87		...	...	...
M33	0.118	3.55×10^4	0.11	0.99	0.111	3.58×10^2	0.07	0.40	0.209	6.39×10^3	0.12	0.39	0.216	8.50×10^4	0.24	0.82
		4.28×10^4	0.23	0.83		2.77×10^4	0.21	0.83		3.53×10^4	0.16	0.91		4.30×10^5	0.74	0.82
		2.40×10^4	0.28	0.94		1.07×10^5	0.35	0.82		5.23×10^4	0.31	0.80		5.59×10^1	4.26	1.00
		8.85×10^4	0.42	0.87		9.19×10^4	0.57	0.86		5.85×10^4	0.47	0.83		...	...	...
		1.46×10^5	0.68	0.86		1.02×10^5	0.65	0.77		1.41×10^5	0.78	0.80		...	...	...
		1.71×10^4	0.82	0.96		2.68×10^5	1.14	0.82		1.25×10^5	1.37	0.89		...	...	...
		2.08×10^5	1.17	0.85		4.21×10^5	2.62	0.80		1.98×10^5	1.71	0.75		...	...	...
		2.69×10^5	1.98	0.87		...	...	...		1.01×10^6	4.22	0.82		...	...	...
		3.32×10^5	4.17	0.84		...	...	...		...	...	...		...	...	...
NGC 247	0.038	2.05×10^4	0.61	0.92	0.036	2.68×10^5	1.50	0.95	0.043	1.87×10^3	0.53	0.78	0.102	8.55×10^4	0.76	0.95
		7.43×10^4	1.19	0.93		5.65×10^5	4.08	1.00		6.30×10^3	0.69	1.00		4.16×10^5	2.44	0.95
		1.43×10^5	1.95	0.93		2.50×10^4	6.43	0.16		3.82×10^4	1.27	0.94		5.74×10^1	15.91	1.00
		1.32×10^5	2.76	0.92		2.52×10^1	16.23	0.37		1.18×10^5	2.14	0.95		...	...	...
		1.88×10^5	3.54	0.93		...	...	...		1.24×10^5	3.09	0.92		...	...	...
		2.07×10^5	5.06	0.92		...	...	...		1.52×10^5	3.67	0.96		...	...	...
		8.56×10^4	7.62	0.92		...	...	...		2.13×10^5	4.88	0.94		...	...	...
		3.74×10^3	16.22	0.94		...	...	...		1.32×10^5	6.52	0.95		...	...	...
		...	...	...		...	...	...		1.94×10^4	9.22	0.93		...	...	...

		⋯	⋯	⋯		⋯	⋯	⋯		2.27×10^{2}	16.55	0.18		⋯	⋯	⋯
NGC 300	0.048	2.96×10^{4}	0.29	1.00	0.049	3.81×10^{4}	0.42	0.98	0.046	7.27×10^{2}	0.29	0.35	0.086	3.47×10^{4}	0.47	0.94
		5.49×10^{4}	0.64	0.92		4.03×10^{5}	1.43	0.87		6.24×10^{3}	0.31	0.98		3.76×10^{5}	1.51	0.94
		7.75×10^{4}	1.08	0.92		5.50×10^{0}	9.12	1.00		2.56×10^{4}	0.63	0.94		5.32×10^{0}	9.02	1.00
		1.02×10^{5}	1.66	0.92		⋯	⋯	⋯		6.21×10^{4}	1.11	0.97		⋯	⋯	⋯
		1.49×10^{5}	2.57	0.92		⋯	⋯	⋯		1.09×10^{4}	1.40	0.75		⋯	⋯	⋯
		2.27×10^{5}	4.28	0.92		⋯	⋯	⋯		1.35×10^{5}	1.90	0.94		⋯	⋯	⋯
		3.38×10^{5}	9.06	0.91		⋯	⋯	⋯		2.00×10^{5}	3.00	0.94		⋯	⋯	⋯
		⋯	⋯	⋯		⋯	⋯	⋯		2.34×10^{5}	4.76	0.94		⋯	⋯	⋯
		⋯	⋯	⋯		⋯	⋯	⋯		1.46×10^{5}	8.40	0.93		⋯	⋯	⋯
NGC 2403	0.073	4.82×10^{2}	0.23	1.00	0.064	1.07×10^{5}	1.44	0.94	0.097	9.88×10^{3}	0.62	1.00	0.090	8.73×10^{4}	1.78	0.95
		5.84×10^{3}	0.47	1.00		1.67×10^{6}	3.79	0.94		1.30×10^{4}	1.13	0.84		3.53×10^{5}	2.63	0.95
		3.65×10^{4}	0.93	0.95		1.46×10^{2}	14.51	1.00		6.52×10^{4}	1.43	0.97		4.12×10^{5}	3.57	0.95
		1.40×10^{5}	1.63	0.93		⋯	⋯	⋯		1.95×10^{5}	2.32	0.93		5.46×10^{5}	4.90	0.94
		3.31×10^{5}	2.56	0.93		⋯	⋯	⋯		3.64×10^{5}	3.32	0.95		4.08×10^{5}	7.47	0.95
		3.88×10^{5}	3.54	0.94		⋯	⋯	⋯		2.45×10^{5}	4.63	0.94		3.55×10^{4}	14.38	0.91
		5.50×10^{5}	4.79	0.93		⋯	⋯	⋯		4.35×10^{5}	4.96	0.94		⋯	⋯	⋯
		3.15×10^{5}	6.85	0.94		⋯	⋯	⋯		5.50×10^{5}	7.26	0.94		⋯	⋯	⋯
		1.18×10^{4}	14.73	0.87		⋯	⋯	⋯		4.42×10^{4}	14.58	0.92		⋯	⋯	⋯
NGC 2976	0.127	1.63×10^{5}	0.28	1.00	0.180	1.30×10^{5}	0.31	1.00	0.147	7.23×10^{4}	0.59	1.00	0.149	2.35×10^{5}	0.92	0.91
		4.05×10^{5}	0.83	0.65		1.10×10^{5}	0.79	0.85		4.18×10^{4}	0.94	0.79		5.57×10^{5}	1.90	0.91
		1.20×10^{5}	1.02	0.86		5.52×10^{5}	1.13	0.48		1.79×10^{5}	1.22	0.91		6.53×10^{5}	4.83	0.91
		5.26×10^{5}	1.29	0.44		4.76×10^{5}	2.06	0.48		2.76×10^{5}	1.90	0.89		1.35×10^{4}	17.28	0.14
		2.85×10^{5}	1.90	0.48		3.00×10^{5}	3.13	0.48		3.36×10^{5}	2.82	0.90		⋯	⋯	⋯
		4.08×10^{4}	2.53	0.50		2.60×10^{5}	4.82	0.47		1.19×10^{5}	3.82	0.89		⋯	⋯	⋯
		1.37×10^{3}	3.33	0.49		1.64×10^{5}	7.50	0.48		1.99×10^{5}	4.51	0.89		⋯	⋯	⋯
		4.15×10^{0}	4.18	0.50		9.99×10^{2}	10.14	1.00		1.26×10^{5}	6.44	0.90		⋯	⋯	⋯
		1.78×10^{-9}	4.20	0.98		7.33×10^{4}	12.13	0.47		2.41×10^{4}	9.93	0.89		⋯	⋯	⋯
		9.88×10^{-3}	4.79	0.51		⋯	⋯	⋯		⋯	⋯	⋯		⋯	⋯	⋯
NGC 3621	0.145	1.72×10^{5}	0.53	0.40	0.160	1.19×10^{5}	0.53	0.39	0.309	2.93×10^{6}	1.07	0.96	0.305	3.84×10^{6}	1.18	0.96

		1.76×10^{6}	0.92	0.96		2.87×10^{6}	0.89	0.92		3.50×10^{6}	2.03	0.96		3.76×10^{6}	2.14	0.95
		4.22×10^{6}	1.75	0.80		3.97×10^{6}	1.62	0.81		2.99×10^{6}	3.23	0.95		2.72×10^{6}	3.49	0.95
		5.24×10^{5}	2.27	1.00		3.30×10^{6}	2.48	0.81		2.20×10^{6}	4.68	0.95		1.96×10^{6}	5.12	0.95
		5.16×10^{6}	2.64	0.79		2.52×10^{6}	3.56	0.80		1.15×10^{6}	6.33	0.94		1.62×10^{6}	7.30	0.95
		3.28×10^{6}	3.70	0.79		2.72×10^{6}	5.13	0.80		6.89×10^{5}	7.90	0.96		1.44×10^{6}	10.84	0.95
		7.86×10^{5}	4.77	0.79		2.07×10^{6}	7.76	0.79		5.17×10^{5}	10.40	0.95		1.01×10^{6}	17.58	0.95
		1.17×10^{5}	5.90	0.79		1.54×10^{6}	11.73	0.80		1.66×10^{5}	15.44	0.95		2.82×10^{5}	31.76	0.95
		5.70×10^{3}	7.20	0.79		8.87×10^{5}	18.81	0.79		8.68×10^{3}	34.18	0.93		...	...	...
		4.98×10^{1}	8.90	0.78		1.84×10^{5}	28.30	0.83		...	...	...		...	...	...
		7.38×10^{-3}	9.43	1.00		...	...	...		...	...	...		...	...	...
NGC 4244	0.015	1.50×10^{5}	0.84	1.00	0.016	2.08×10^{5}	1.01	1.00	0.016	9.39×10^{4}	1.39	0.79	0.018	1.75×10^{5}	2.46	0.32
		1.77×10^{5}	2.06	0.40		8.30×10^{5}	2.89	0.50		4.13×10^{5}	2.95	0.70		2.41×10^{5}	2.60	0.60
		2.67×10^{5}	2.61	1.00		1.69×10^{6}	6.72	0.48		3.07×10^{5}	4.07	1.00		3.99×10^{5}	5.19	0.28
		7.78×10^{5}	4.23	0.37		2.33×10^{5}	20.17	0.15		1.68×10^{5}	4.32	0.31		8.45×10^{5}	5.22	0.56
		4.09×10^{5}	6.00	1.00		5.54×10^{0}	20.17	1.00		8.77×10^{5}	6.39	0.49		8.45×10^{5}	10.10	0.59
		8.82×10^{5}	7.85	0.35		...	...	...		6.63×10^{5}	7.95	0.76		...	...	...
		8.57×10^{5}	16.31	1.00		...	...	...		6.92×10^{4}	11.01	1.00		...	...	...
		...	...	...		...	...	...		1.90×10^{5}	15.22	0.29		...	...	...
NGC 7793	0.059	4.32×10^{5}	0.47	0.94	0.064	8.98×10^{5}	0.85	0.72	0.056	2.50×10^{4}	0.31	0.69	0.119	5.91×10^{5}	0.78	0.83
		1.39×10^{5}	0.88	0.51		2.08×10^{6}	3.08	0.68		9.09×10^{4}	0.62	1.00		1.93×10^{6}	2.57	0.81
		4.59×10^{5}	1.37	0.70		5.64×10^{0}	15.69	1.00		1.13×10^{5}	0.95	0.72		5.73×10^{0}	16.00	1.00
		4.40×10^{5}	2.27	0.66		...	...	...		3.57×10^{5}	1.50	0.83		...	...	...
		7.07×10^{5}	3.56	0.67		...	...	...		5.74×10^{5}	2.51	0.82		...	...	...
		1.08×10^{6}	6.70	0.65		...	...	...		5.50×10^{4}	2.59	0.56		...	...	...
		1.81×10^{6}	15.67	0.68		...	...	...		7.46×10^{5}	3.92	0.78		...	...	...
		...	...	...		...	...	...		9.15×10^{5}	5.71	0.80		...	...	...
		...	...	...		...	...	...		1.05×10^{6}	9.26	0.77		...	...	...
		...	...	...		...	...	...		5.89×10^{5}	16.16	0.86		...	...	...

Deprojected Stellar Density Profiles

In general, the deprojection of a 2D surface density profile is not unique, and will depend on assumptions about the inclination and intrinsic geometry of the NC (e.g., oblate spheroidal, prolate spheroidal, etc.). For the purposes of deprojection, we will assume that all NCs in our sample are oblate spheroids. Under this assumption, $\sigma_j = \sigma'_j$. In the unprimed coordinate system (x,y,z) which is centered on the NC and aligned with the its principal axes, the intrinsic 3D density profile is written

$$\rho(x, y, z) = \sum_{j=1}^{N} \frac{M_j}{(\sqrt{2\pi}\sigma_j)^3 q_j} \exp\left[-\frac{1}{2\sigma_j^2}\left(x^2 + y^2 + \frac{z^2}{q_j^2}\right)\right], \tag{4.4}$$

where q_j is the intrinsic axial ratio, given by

$$q_j = \frac{q_j'^2 - \cos^2 i}{\sin^2 i}, \tag{4.5}$$

and i is the inclination angle (i.e., the angle between the z axis and the line of sight to the observer). Figure 4.8 shows the deprojected central density vs. the assumed inclination for Model 1 of each NC. Host galaxy inclinations (denoted by a vertical dashed line in Figure 4.8) were taken from 2MASS (Jarrett et al., 2003), calculated from isophotal fits to the K-band images. From equation 4.5, it is clear that the deprojection is only defined if $\cos^2 i < q_j'^2$ for all Gaussians, thus it is not always possible to assume the same inclination for the NC and the host galaxy. Since we have no *a priori* information about the inclination of the NCs, we assume $i = 90°$ for the whole sample. This results in the minimum possible deprojected 3D density.

Figure 4.9 shows the deprojected density as a function of distance from the center (r) in the $z = 0$ plane of each cluster. To produce the curves in this plot, we computed a weighted average of the four deprojected MGE models at each radius, where $e^{-\chi^2}$ is the weighting

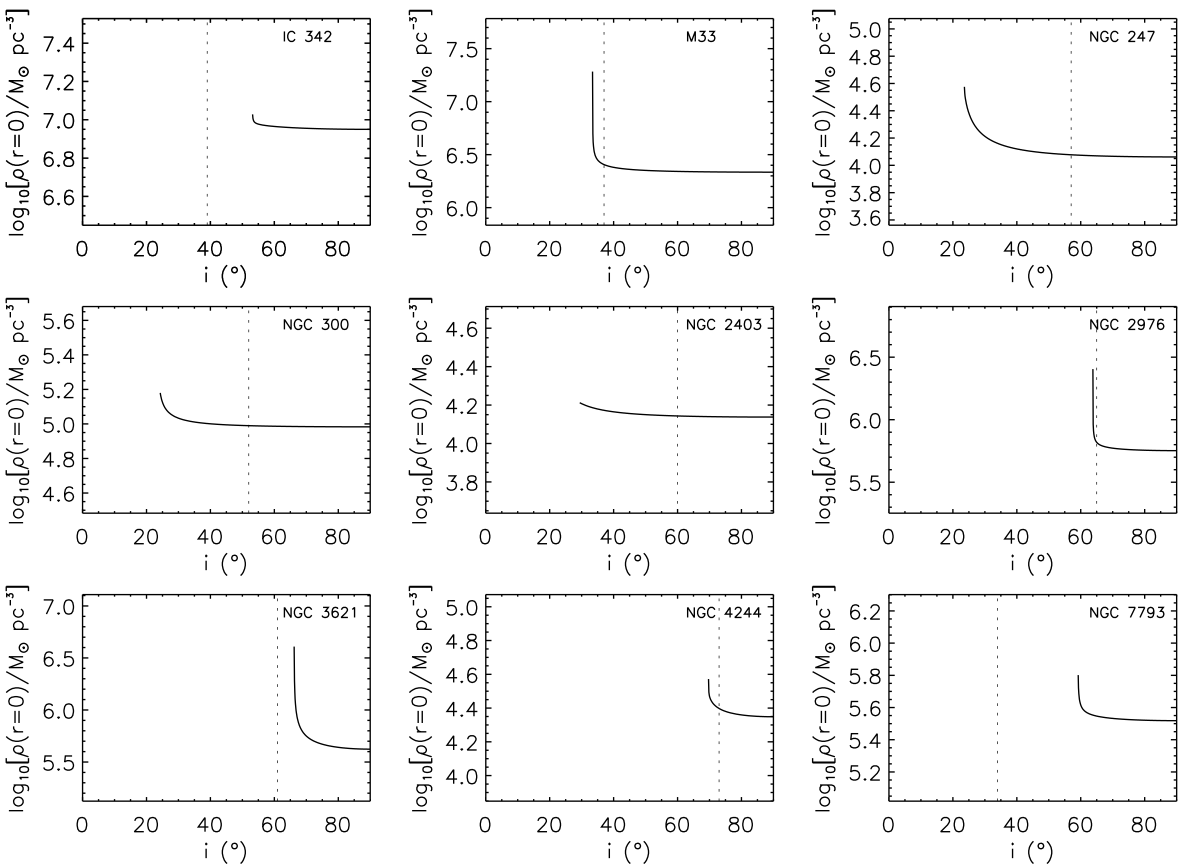

Figure 4.8 Deprojected central density vs. the assumed inclination for Model 1 of each cluster. Since the deprojection is only defined when $\cos^2 i < q_j'^2$ for all Gaussians, the central density diverges at the value of i where $\cos^2 i = \min(q_j'^2)$. The vertical dashed line on each plot denotes the host galaxy inclination.

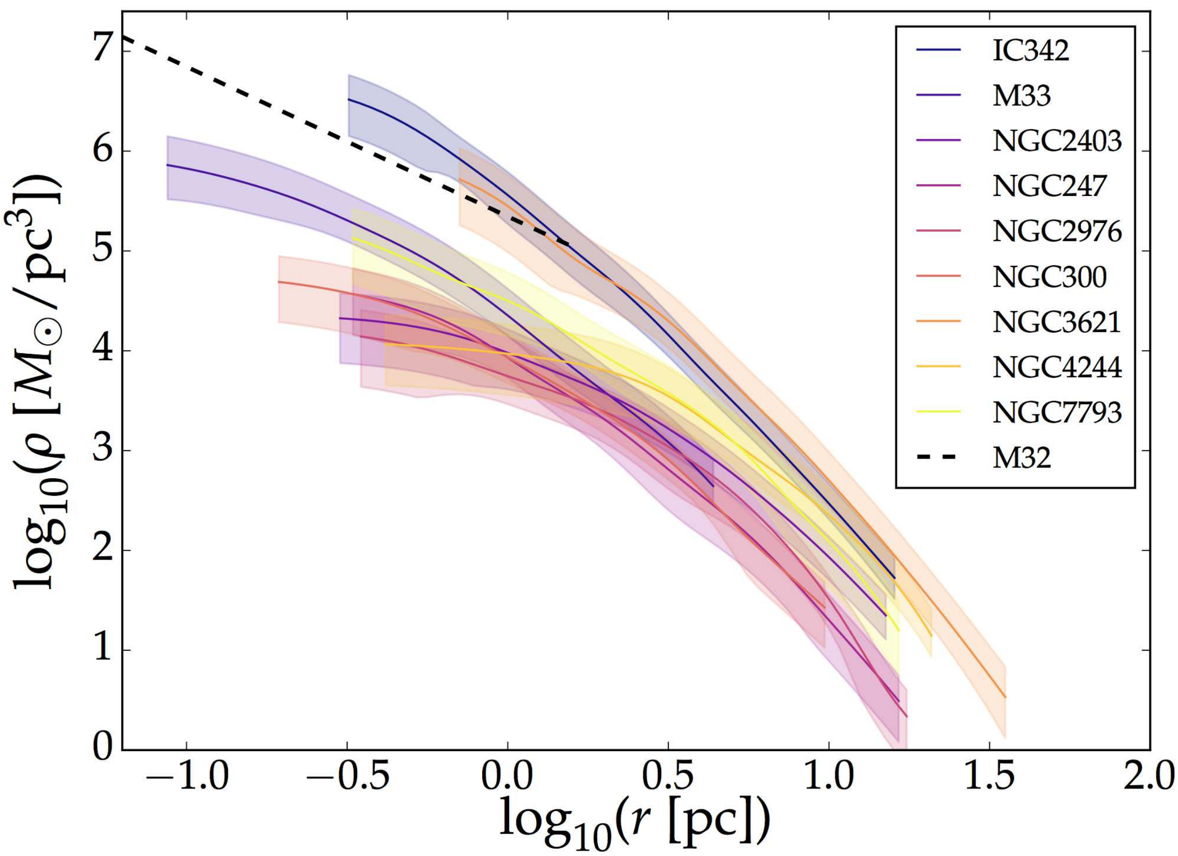

Figure 4.9 Deprojected density profiles in the $z = 0$ plane, assuming oblate spheroidal geometry and an inclination of 90°. We also include the best-fit power-law profile of M32 from Lauer et al. (1998).

factor. We also computed the spread of the four models at each radius using the same weighting scheme. This spread was added in quadrature to the overall uncertainty on the density due to uncertainty on the global mass-to-light ratio, producing the error bands in Figure 4.9.

Radial Age Gradients

Recent imaging studies of NCs have revealed evidence for radially varying stellar populations. In a study of a large *HST*/WFPC2 archival sample of NCs, Georgiev & Böker (2014) found that the effective radii of NCs tend to be smaller when measured in bluer filters, suggesting that young stellar populations are generally more concentrated than the bulk of the stars. We also found a wavelength dependence of the effective radius in some of the clusters in Chapter 3. For M33, NGC 247 and NGC 300, the effective radius monotonically increases from F275W to F153M. In contrast, the effective radius monotonically decreases with wavelength for NGC 3621 and NGC 7793. We used the $\langle \log_{10}\tau \rangle_{\mathrm{M}}$ and $\langle \log_{10}\tau \rangle_{\mathrm{L}_B}$ maps (shown in Figure 4.5) to search for corresponding radial gradients in age.

Radial profiles of $\langle \log_{10}\tau \rangle_{\mathrm{M}}$ and $\langle \log_{10}\tau \rangle_{\mathrm{L}_B}$ for each cluster were produced by performing aperture photometry on the $\langle \log_{10}\tau \rangle_{\mathrm{M}}$ and $\langle \log_{10}\tau \rangle_{\mathrm{L}_B}$ maps, using concentric elliptical annuli. The center, axial ratio, and position angle of the elliptical annulus was determined from the best-fit F814W `GALFIT` surface brightness profile (see Chapter 3 for best-fit parameters). The width of each elliptical annulus was fixed at 1 UVIS pixel, while the major axis was increased in steps of 1 UVIS pixel until the edge of the age map was reached. The average values of $\langle \log_{10}\tau \rangle_{\mathrm{M}}$ and $\langle \log_{10}\tau \rangle_{\mathrm{L}_B}$ within each annulus were computed to construct their respective radial profiles. The corresponding 1σ error bars are computed by adding two terms in quadrature: the mean uncertainty in age among the pixels within the elliptical annulus, and the scatter in the best-fit value of age among the pixels within the elliptical annulus. The first term accounts for uncertainties in the age estimates computed by the SED fitting code, while the second term reflects the fact that there will be a range of best-fit ages within each annulus. We fit a linear function to each radial profile using the IDL routine `linmix_err` (Kelly, 2007). Although the radial profiles are not strictly linear, the intention is simply to determine whether or not we can measure statistically significant age gradients within the NCs. The best-fit slopes for the $\langle \log_{10}\tau \rangle_{\mathrm{M}}$ radial profiles (α_{M}) and the $\langle \log_{10}\tau \rangle_{\mathrm{L}_B}$ radial profiles (α_{L_B}) are given in Table 4.6.

We find statistically significant $\langle \log_{10}\tau \rangle_{\mathrm{M}}$ gradients in four of the nine clusters in our sample. The slope α_{M} is positive for M33, NGC 247, and NGC 4244, indicating a trend of increasing mass-weighted ages with radius; while the α_{M} is negative for NGC 2976, corresponding to a

Table 4.6. Age Radial Profile Slopes

Object	α_{M} (dex pc^{-1})	α_{L_B}(dex pc^{-1})
IC 342	-0.028 ± 0.030	-0.057 ± 0.018
M33	0.083 ± 0.058	0.100 ± 0.019
NGC 247	0.035 ± 0.017	0.054 ± 0.009
NGC 300	0.022 ± 0.025	0.062 ± 0.014
NGC 2403	0.007 ± 0.016	0.012 ± 0.012
NGC 2976	-0.059 ± 0.026	-0.109 ± 0.022
NGC 3621	-0.006 ± 0.007	-0.007 ± 0.005
NGC 4244	0.025 ± 0.012	0.025 ± 0.005
NGC 7793	-0.009 ± 0.018	-0.039 ± 0.007

Note. — Best-fit slopes from linear fits to the $\langle \log_{10}\tau \rangle_{\mathrm{M}}$ and $\langle \log_{10}\tau \rangle_{\mathrm{L}_B}$ radial profiles.

trend of younger mass-weighted ages at larger radii. For all other NCs, α_{M} is consistent with zero. Gradients in $\langle \log_{10}\tau \rangle_{\mathrm{L}_B}$ are found in eight NCs: α_{L_B} is positive for M33, NGC 247, NGC 300, and NGC 4244, and negative for IC 342, NGC 2976, NGC 3621, and NGC 7793. NGC 2403 is the only cluster in the sample with no detectable gradient in $\langle \log_{10}\tau \rangle_{\mathrm{L}_B}$. For every NC that exhibited a wavelength dependent effective radius, a corresponding $\langle \log_{10}\tau \rangle_{\mathrm{L}_B}$ radial gradient was detected; however, we also detect $\langle \log_{10}\tau \rangle_{\mathrm{L}_B}$ gradients in the clusters for which no such wavelength dependence was found. The positive age gradient in M33 is consistent with the strong $V-I$ and $B-R$ color gradients observed by Lauer et al. (1998). We also note that the slope α_{L_B} is nearly always steeper than α_{M}, indicating that gradients in luminosity-weighted age are more readily detected than gradients in mass-weighted age.

Menezes et al. (2016) recently detected a compact source of emission lines 214 from the nucleus of NGC 3621. Since the line ratios are consistent with those of a Seyfert 2 galaxy, they proposed that this emission if a light echo from a spike in AGN activity ~ 200 years ago. Although the blob of line emission they observed is outside of the $2'' \times 2''$ field-of-view

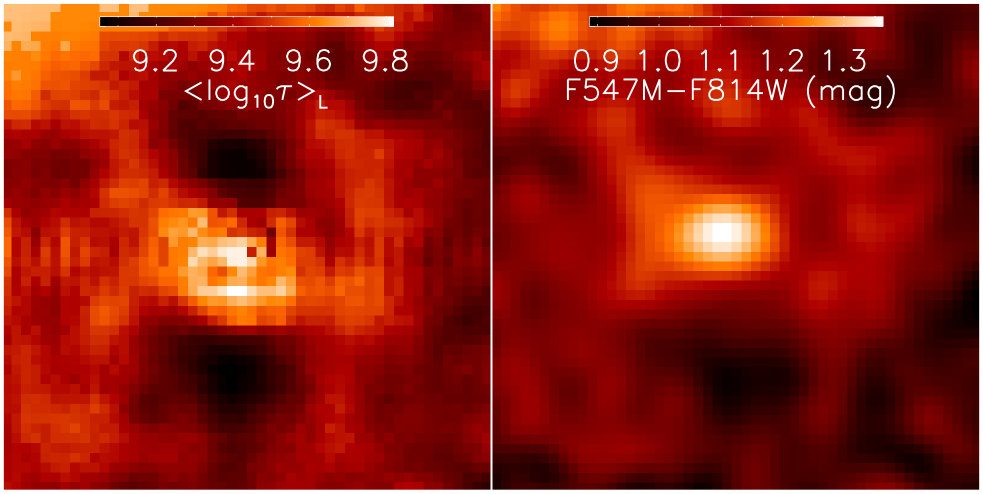

Figure 4.10 The panel on the left shows the luminosity-weighted age map of the nucleus of NGC 3621, and the panel on the right shows the F547M−F814W. The color map traces the double-lobed feature in the $\langle \log_{10}\tau \rangle_{L_B}$ map, which indicates that emission line contamination is not driving the trend of decreasing $\langle \log_{10}\tau \rangle_{L_B}$ with radius.

of our data cubes, it is conceivable that there are other light echos from other clouds within our field of view. However, the *HST* filters used in our study were selected to avoid strong emission lines, so it is unlikely that the radial $\langle \log_{10}\tau \rangle_{L_B}$ gradient in the nucleus of NGC 3621 is driven by contamination from emission lines. The F547M−F814W color map (displayed in Figure 4.10) traces the features of the $\langle \log_{10}\tau \rangle_{L_B}$map, indicating that the radial age gradient is driven by stellar emission, rather than AGN emission.

4.3 Discussion

4.3.1 Comparison of Results from Global and Pixel-by-Pixel SED Fitting

In this subsection, we make a direct comparison between the results of the global SED fits described in Section 4.1 and the pixel-by-pixel SED fits described in Section 4.2. These methods are known to yield different stellar mass estimates in galaxies, as dust lanes and star

Table 4.7. Comparison of Resolved and Unresolved Mass and Age Estimates

Object	Mass ($M_\odot$) unresolved	Mass ($M_\odot$) resolved	$\langle \log_{10} \tau \rangle_{\rm M}$ unresolved	$\langle \log_{10} \tau \rangle_{\rm M}$ resolved	$\langle \log_{10} \tau \rangle_{{\rm L}_B}$ unresolved	$\langle \log_{10} \tau \rangle_{{\rm L}_B}$ resolved
IC 342	$1.22^{+0.70}_{-0.33} \times 10^7$	1.20×10^7	$8.63^{+0.45}_{-0.39}$	8.40	$8.29^{+0.23}_{-0.14}$	8.01
M33	$1.30^{+1.07}_{-0.39} \times 10^6$	1.08×10^6	$9.40^{+0.37}_{-0.27}$	9.44	$9.08^{+0.11}_{-0.07}$	9.11
NGC 247	$1.25^{+0.79}_{-0.44} \times 10^6$	7.58×10^5	$9.46^{+0.38}_{-0.31}$	9.42	$9.00^{+0.09}_{-0.08}$	9.10
NGC 300	$9.10^{+5.80}_{-3.09} \times 10^5$	6.65×10^5	$9.54^{+0.34}_{-0.25}$	9.53	$9.40^{+0.23}_{-0.17}$	9.33
NGC 2403	$2.31^{+1.39}_{-0.94} \times 10^6$	1.83×10^6	$9.63^{+0.34}_{-0.42}$	9.71	$9.63^{+0.33}_{-0.42}$	9.67
NGC 2976	$7.99^{+5.41}_{-3.77} \times 10^5$	1.61×10^6	$8.33^{+0.90}_{-0.69}$	9.47	$7.32^{+0.31}_{-0.29}$	8.98
NGC 3621	$1.36^{+1.24}_{-0.57} \times 10^7$	1.68×10^7	$9.39^{+0.44}_{-0.26}$	9.67	$9.26^{+0.08}_{-0.14}$	9.54
NGC 4244	$3.36^{+2.79}_{-1.20} \times 10^6$	2.94×10^6	$9.51^{+0.38}_{-0.37}$	9.43	$9.08^{+0.13}_{-0.21}$	9.11
NGC 7793	$5.60^{+4.70}_{-2.30} \times 10^6$	3.79×10^6	$9.40^{+0.41}_{-0.35}$	9.44	$8.79^{+0.06}_{-0.08}$	8.90

forming regions are averaged over in pixel-by-pixel fits. For instance, Zibetti et al. (2009) found that stellar mass estimates of galaxies based on global fluxes can be biased low by up to 40% compared to estimates based on spatially resolved SED fitting, due to the fact that dusty regions are under-represented in the global fluxes. However, these effects have not been investigated on parsec-scale objects such as NCs. A comparison of masses derived from global SED fitting and pixel-by-pixel SED fitting is given in Table 4.7.

The total mass in a given surface density model is the sum of the masses of the individual Gaussian components. We compute the spatially resolved stellar mass estimate, $M_{\rm resolved}$, by taking a weighted average of the total mass of the four MGE models listed in Table 4.5 (as before, the weighting factor is $e^{-\chi^2}$). Averaged over the entire sample, the ratio of the resolved and unresolved stellar mass estimates ($M_{\rm resolved}/M_{\rm unresolved}$) is 0.99, which is not consistent with the enhancement in the spatially resolved stellar mass estimate demonstrated by Zibetti et al. (2009). There is however a crucial difference between our method and that of Zibetti et al. (2009), namely that $E(B-V)$ was fixed at the global best-fit value in the pixel-by-pixel SED fits (with the exception of IC 342 and NGC 2976). NGC 2976 is by far the dustiest cluster in our sample, and also shows the largest deviation between $M_{\rm resolved}$ and

$M_{\mathrm{unresolved}}$, with a factor of 2.0 enhancement in the spatially resolved estimate. The regions obscured by dust in this cluster contribute only a small fraction of the total flux, but contain a significant amount of stellar mass.

We also compared the age estimates derived from global and pixel-by-pixel SED fits. For each NC, we calculated the mean of the $\langle \log_{10}\tau \rangle_{\mathrm{M}}$ and $\langle \log_{10}\tau \rangle_{\mathrm{L}_B}$ maps displayed in Figure 4.5, weighted by the total stellar mass in each pixel. The ages derived from global SED fitting and pixel-by-pixel SED fitting are also generally consistent. The average difference between the resolved and unresolved age estimates is 0.13 dex for $\langle \log_{10}\tau \rangle_{\mathrm{M}}$ and 0.21 dex for $\langle \log_{10}\tau \rangle_{\mathrm{L}_B}$, while the average symmetrized uncertainties from the global SED fits are 0.41 dex for $\langle \log_{10}\tau \rangle_{\mathrm{M}}$ and 0.17 dex for $\langle \log_{10}\tau \rangle_{\mathrm{L}_B}$.

4.3.2 Comparison With Mass-to-Light Ratio vs. Color Relations

Quasi-linear relations between stellar M/L and broadband colors (known as mass-to-light ratio vs. color relations, or MLCRs), are often used to estimate the stellar mass of galaxies when multi-band photometry or spectroscopy are unavailable. Estimating stellar masses from MLCRs is convenient because it is computationally inexpensive, and requires only two bands of photometry at minimum. Use of MLCRs is widespread, and several different calibrations have been formulated (e.g., Bell & de Jong, 2001; Bell et al., 2003; Zibetti et al., 2009; Roediger & Courteau, 2015).

In this Section, we compute NC stellar masses from MLCRs developed by Bell et al. (2003) and Zibetti et al. (2009), and compare them with stellar mass estimates derived from global SED fits (as outlined in Section 4.1.1). For both sets of MLCRs, we computed the B, V, and I-band mass-to-light ratios of each NC from the observed $B-V$ color. Each mass-to-light ratio was multiplied by the corresponding luminosity to obtain a stellar mass estimate. The mean and scatter of the three mass estimates were computed. To compute the uncertainties, we added the scatter in quadrature to the propagated photometric errors. In Table 4.8, we list mass estimates computed from the Bell et al. (2003) and Zibetti et al. (2009) MLCRs, as well as the ratio of mass estimates obtained from MLCRs and SED fitting ($M_{\mathrm{Bell}}/M_{\mathrm{SEDfit}}$ and $M_{\mathrm{Zibetti}}/M_{\mathrm{SEDfit}}$).

Table 4.8: Comparison With Mass Estimates Derived From MLCRs

Object	Global SED Fit Mass Estimate ($M_\odot$)	Bell et al. (2003) MLCR Mass Estimate ($M_\odot$)	$M_{\rm Bell}/M_{\rm SEDfit}$	Zibetti et al. (2009) MLCR Mass Estimate ($M_\odot$)	$M_{\rm Zibetti}/M_{\rm SEDfit}$
IC 342	$1.22^{+0.70}_{-0.33} \times 10^7$	$(3.90 \pm 1.01) \times 10^7$	3.19	$(2.41 \pm 0.57) \times 10^7$	1.97
M33	$1.30^{+1.07}_{-0.39} \times 10^6$	$(3.39 \pm 0.29) \times 10^6$	2.60	$(2.68 \pm 0.44) \times 10^6$	2.06
NGC 247	$1.25^{+0.79}_{-0.44} \times 10^6$	$(2.49 \pm 0.71) \times 10^6$	2.00	$(1.50 \pm 0.44) \times 10^6$	1.20
NGC 300	$9.10^{+5.80}_{-3.09} \times 10^5$	$(2.12 \pm 0.15) \times 10^6$	2.33	$(1.79 \pm 0.29) \times 10^6$	1.97
NGC 2403	$2.31^{+1.39}_{-0.94} \times 10^6$	$(6.20 \pm 1.94) \times 10^6$	2.68	$(8.00 \pm 2.68) \times 10^6$	3.46
NGC 2976	$7.99^{+5.41}_{-3.77} \times 10^5$	$(2.62 \pm 0.80) \times 10^6$	3.28	$(2.57 \pm 0.71) \times 10^6$	3.22
NGC 3621	$1.36^{+1.24}_{-0.57} \times 10^7$	$(3.59 \pm 0.91) \times 10^7$	2.64	$(3.09 \pm 0.89) \times 10^7$	2.28
NGC 4244	$3.36^{+2.79}_{-1.20} \times 10^6$	$(6.68 \pm 0.64) \times 10^6$	1.99	$(5.14 \pm 0.82) \times 10^6$	1.53
NGC 7793	$5.60^{+4.70}_{-2.30} \times 10^6$	$(1.16 \pm 0.16) \times 10^7$	2.08	$(7.32 \pm 1.42) \times 10^6$	1.31

The mass estimates derived from MLCRs are significantly larger than mass estimates derived from SED fitting. The sample averages of $M_{\rm Bell}/M_{\rm SEDfit}$ and $M_{\rm Zibetti}/M_{\rm SEDfit}$ are 2.53 and 2.11 (or 0.40 dex and 0.32 dex), respectively. Bell et al. (2003) derived their MLCRs from PEGASE (Fioc & Rocca-Volmerange, 1997) stellar population synthesis models, assuming a "diet" Salpeter (1955) IMF. Estimates of M/L based on a Salpeter (1955) IMF are enhanced by 0.3 dex compared to estimates based on a Chabrier (2003) IMF, which explains most, but not all of the discrepancy between $M_{\rm Bell}$ and $M_{\rm SEDfit}$. Zibetti et al. (2009) used a Chabrier (2003) IMF, and computed their set of MLCRs from the unpublished 2007 version of the BC03 models, which differ from the original models in their treatment of thermally-pulsating asymptotic giant branch (TP-AGB) stars. The Zibetti et al. (2009) study showed that the treatment of the TP-AGB phase of stellar evolution can affect optical M/L estimates by as much as 0.1 dex, which may account for some of the discrepancy between $M_{\rm Zibetti}$ and $M_{\rm SEDfit}$. More importantly however, optical-band MLCRs systematically overestimate M/L by ~ 0.2 dex for intermediate-age populations with a bursty star formation history (Gallazzi & Bell, 2009). Nuclear clusters are likely to be affected by this bias. While the NC stellar mass estimates derived from SED fitting are in good agreement with dynamical studies (see Table 4.3), the stellar mass estimates derived from MLCRs are all systematically higher, with the exception of NGC 4244. NGC 4244 is also the only NC for which the MLCR mass estimate is in better agreement with the dynamical mass estimate than the mass estimate derived from SED fitting. We conclude that multi-band SED fitting is a more accurate method of estimating NC stellar masses than mass-to-light ratio vs. color relations.

4.3.3 Central Densities

The innermost stellar densities of NCs are of key interest. The expected rate of tidal disruptions of stars by SMBHs in galactic nuclei is determined by the central stellar densities of NCs (e.g., Wang & Merritt, 2004; Merritt, 2009; Brockamp et al., 2011). Hopkins et al.

(2010) proposed a universal maximum stellar surface density of $\Sigma_{\mathrm{max}} \sim 10^5\ M_\odot\ \mathrm{pc}^{-2}$, based on the fact that the observed stellar surface density profiles of a wide range of dense stellar systems seem to asymptote towards this value in their central regions. The explanation they propose for this limit is feedback from massive stars, which produces radiation pressure that regulates the growth of these systems. Measurements of the innermost stellar densities for our NC sample are therefore important for constraining the role of tidal disruption and stellar feedback in the evolution of NCs.

Due to the pixel scale of WFC3, we have no information about the shape of the NC density profiles on angular scales finer than 004, and we will therefore not attempt to extrapolate inwards of half of a UVIS pixel in radius. In Table 4.9, we list $\Sigma(r_{\mathrm{min}})$, the surface density at r_{min}, a projected distance subtending half of a UVIS pixel and the effective surface density, defined as

$$\Sigma_{\mathrm{eff}} \equiv \frac{M(< R_{\mathrm{eff}})}{\pi R_{\mathrm{eff}}^2}, \tag{4.6}$$

where R_{eff} encloses half of the total stellar mass of the cluster. $\Sigma(r_{\mathrm{min}})$ represents a lower limit on the central surface density (Σ_0). The densities quoted in this table were computed by taking a weighted average of MGE Models 1-4 at the radius stated (as before, the weighting factor is $e^{-\chi^2}$). The corresponding uncertainties were computed by adding the weighted spread of the four models in quadrature to the overall uncertainty on the density due to uncertainty on the global mass-to-light ratio. Note that the surface densities listed in this table are larger than the central surface densities in Figure 4.5, because they are *intrinsic* surface density profiles, disentangled from the effects of PSF blurring. We also list $\rho(r_{\mathrm{min}})$, the deprojected 3D density at a radius of r_{min} in this table.

Table 4.9: Col. (1): Galaxy name. Col. (2): Projected distance subtending 0.5 UVIS pixels. Col. (3): Surface density at $r_{\rm min}$. Col. (4): Effective (half-mass) radius. Col. (5): Effective surface density. Col. (6): Deprojected 3D density at $r_{\rm min}$.

Object (1)	$r_{\rm min}$ (pc) (2)	$\Sigma(r_{\rm min})$ ($M_\odot$ pc^{-2}) (3)	$R_{\rm eff}$ (pc) (4)	$\Sigma_{\rm eff}$ ($M_\odot$ pc^{-2}) (5)	$\rho(r_{\rm min})$ ($M_\odot$ pc^{-3}) (6)
IC 342	0.32	$3.27^{+2.72}_{-2.17} \times 10^6$	1.98 ± 0.61	$6.65^{+6.33}_{-1.81} \times 10^5$	$3.29^{+2.50}_{-1.87} \times 10^6$
M33	0.09	$5.50^{+4.69}_{-2.06} \times 10^5$	1.48 ± 0.49	$8.71^{+8.06}_{-4.51} \times 10^4$	$7.24^{+6.82}_{-3.96} \times 10^5$
NGC 247	0.33	$2.68^{+1.81}_{-1.14} \times 10^4$	4.08 ± 1.74	$9.17^{+7.00}_{-5.08} \times 10^3$	$3.70^{+2.98}_{-2.26} \times 10^4$
NGC 300	0.19	$6.36^{+4.44}_{-2.82} \times 10^4$	2.72 ± 1.30	$1.83^{+1.46}_{-1.08} \times 10^4$	$4.89^{+3.96}_{-2.96} \times 10^4$
NGC 2403	0.30	$2.99^{+1.88}_{-1.34} \times 10^4$	5.95 ± 0.00	$8.22^{+4.95}_{-3.36} \times 10^3$	$2.12^{+1.66}_{-1.36} \times 10^4$
NGC 2976	0.35	$2.34^{+2.25}_{-1.11} \times 10^5$	2.26 ± 0.80	$7.63^{+8.04}_{-3.60} \times 10^4$	$1.39^{+1.17}_{-0.96} \times 10^4$
NGC 3621	0.70	$7.33^{+6.91}_{-3.56} \times 10^5$	3.08 ± 0.41	$2.93^{+2.77}_{-1.43} \times 10^5$	$5.21^{+5.42}_{-3.41} \times 10^5$
NGC 4244	0.41	$5.86^{+5.22}_{-2.82} \times 10^4$	7.99 ± 0.54	$7.43^{+6.30}_{-2.96} \times 10^3$	$1.16^{+1.13}_{-0.71} \times 10^4$
NGC 7793	0.33	$2.76^{+2.49}_{-1.46} \times 10^5$	4.47 ± 2.38	$4.61^{+4.81}_{-3.42} \times 10^4$	$1.35^{+1.32}_{-0.87} \times 10^5$

These are among the largest stellar densities ever measured, and the effective surface densities of IC 342 and NGC 3621 both exceed the upper limit proposed by Hopkins et al. (2010). With $\Sigma_{\text{eff}} = 6.65^{+6.33}_{-1.81} \times 10^5\ M_\odot\ \text{pc}^{-2}$, IC 342 has the highest stellar surface density observed to date. The NC sample has a median Σ_{eff} of $4.61 \times 10^4\ M_\odot\ \text{pc}^{-2}$, similar to the highest-density UCDs. For instance, the Virgo Cluster galaxy M60-UCD1 ($\Sigma_{\text{eff}} = 5.4 \times 10^4\ M_\odot\ \text{pc}^{-2}$) is the densest galaxy ever observed (Strader et al., 2013). Sandoval et al. (2015) discovered the remarkably dense stellar system M85-HCC1, which is thought to be the remnant nucleus of a tidally-stripped UCD. This hyper-compact cluster has an effective surface density of 5.8×10^5 $M_\odot\ \text{pc}^{-2}$, making it the densest free-floating stellar system known. The similarities between the stellar densities observed in NCs and UCDs is consistent with the idea that UCDs start off as nucleated dwarf elliptical galaxies, but are stripped of gas and outlying stars by tidal interactions in galaxy clusters (Phillipps et al., 2001; Bekki et al., 2003; Mieske et al., 2013; Seth et al., 2014).

4.3.4 Old, Metal-Poor Populations

In the analysis described thus far, we have assumed a single, uniform metallicity for each nuclear cluster. However, the accretion of globular clusters (GCs) likely plays a role in the formation and growth of NCs (e.g., Lotz et al., 2001; Capuzzo-Dolcetta & Miocchi, 2008). In addition to containing very old (> 10 Gyr) Population II stars, GCs are generally very metal-poor compared to the NCs in our sample, although the metallicity distribution of GCs is bimodal, as discussed by Zepf & Ashman (1993) and Muratov & Gnedin (2010). It is therefore of interest to determine the maximum mass of old, metal-poor stars allowed by our data in each cluster.

To answer this question, we re-ran the global SED fits described in Section 4.1.1 with an additional SSP template of age 13.7 Gyr and metallicity $Z = 0.0004$ in the model to account for a possible population of old, metal-poor stars. That is, each model SED is a linear combination of five SSPs: a 1–10 Myr SSP, a 10–100 Myr SSP, a 100 Myr–1 Gyr SSP, a 1–13.7 Gyr SSP and an SSP with a fixed age of 13.7 Gyr and a fixed metallicity $Z = 0.0004$. We performed 10^5 Monte Carlo realizations for each NC, computing the fraction of the total stellar mass ($f_{M,\mathrm{omp}}$) and the fraction of the total B-band luminosity ($f_{L_B,\mathrm{omp}}$) contributed by the old, metal-poor SSP for each realization. Table 4.10, lists $f_{M,\mathrm{omp}}$ and $f_{L_B,\mathrm{omp}}$, as well as change in $\log_{10}(M/M_\odot)$, $\langle \log_{10} \tau \rangle_{\mathrm{M}}$, and $\langle \log_{10} \tau \rangle_{\mathrm{L}_B}$ upon adding the old, metal-poor population to the model. With the exception of NGC 247, our estimates of $f_{M,\mathrm{omp}}$ and $f_{L_B,\mathrm{omp}}$ are consistent with zero contribution from the old, metal-poor stars. However, the confidence intervals are quite wide, and the addition of the old, metal-poor SSP increases our stellar mass estimate by 0.13 dex on average. The sample-averaged upper limits on the mass contribution and B-band luminosity contribution of old, metal-poor stars are 42% and 17%, respectively.

This result is similar to the upper limit obtained for spectral synthesis fits by Seth et al. (2010), who found a maximum mass fraction of 35% for the old metal-poor population in early-type galaxy NGC 404 using spectra synthesis. Our results suggest that none of the nuclei in our sample are similar to M54, the nucleus of the Sagittarius dwarf spheroidal galaxy, which from its resolved population is clearly dominated in luminosity and mass by a metal-poor component (Monaco et al., 2005; Siegel et al., 2007). It appears that the inspiral of old globular clusters is typically a subdominant process in late-type galaxies, and that NCs in late-type galaxies are likely dominated by stars formed in situ or from the inspiral of younger clusters (Agarwal & Milosavljević, 2011; Hartmann et al., 2011; Antonini et al., 2015).

Table 4.10. Old, Metal-Poor Fractions

Object (1)	$f_{M,\mathrm{omp}}$ (2)	$f_{L_B,\mathrm{omp}}$ (3)	$\Delta\log_{10}M$ (4)	$\Delta\langle\log_{10}\tau\rangle_{\mathrm{M}}$ (5)	$\Delta\langle\log_{10}\tau\rangle_{\mathrm{L}_B}$ (6)
IC 342	$0.00^{+0.00}_{-0.00}$	$0.00^{+0.00}_{-0.00}$	0.02	0.05	0.00
M33	$0.34^{+0.10}_{-0.34}$	$0.11^{+0.10}_{-0.11}$	0.23	0.38	0.15
NGC 247	$0.90^{+0.07}_{-0.22}$	$0.41^{+0.10}_{-0.12}$	0.42	0.59	0.25
NGC 300	$0.00^{+0.60}_{-0.00}$	$0.00^{+0.21}_{-0.00}$	0.08	0.17	0.02
NGC 2403	$0.00^{+0.06}_{-0.00}$	$0.00^{+0.04}_{-0.00}$	0.00	0.00	0.00
NGC 2976	$0.00^{+0.73}_{-0.00}$	$0.00^{+0.04}_{-0.00}$	0.05	0.16	0.06
NGC 3621	$0.39^{+0.12}_{-0.39}$	$0.23^{+0.12}_{-0.23}$	0.28	0.46	0.26
NGC 4244	$0.00^{+0.15}_{-0.00}$	$0.00^{+0.05}_{-0.00}$	0.01	0.02	0.00
NGC 7793	$0.08^{+0.26}_{-0.08}$	$0.01^{+0.08}_{-0.01}$	0.08	0.18	0.02

Note. — Col. (1): Galaxy name. Col. (2): Fraction of the stellar mass contributed by the old, metal-poor SSP. Col. (3): Fraction of the B-band luminosity contributed by the old, metal-poor SSP. Col. (4): Change in stellar mass estimate after adding the old, metal-poor SSP, Col (5): Change in $\langle\log_{10}\tau\rangle_{\mathrm{M}}$. Col. (6): Change in $\langle\log_{10}\tau\rangle_{\mathrm{L}_B}$.

4.3.5 Scaling Relations

In order to investigate relations between NC and host galaxy properties, we computed the total stellar mass of the host galaxies in our sample. Although photometric stellar mass estimates are generally highly uncertain due to the age-metallicity degeneracy, $B-V$ color has been demonstrated to be a good mass-to-light ratio indicator for both late-type and early-type galaxies (McGaugh & Schombert, 2014). The extinction-corrected B-band magnitude and $B-V$ color of each galaxy were obtained from HyperLEDA[1] (Makarov et al., 2014). We computed the B-band mass-to-light ratio from the $B-V$ color according to the M/L-color relations from Bell et al. (2003), and multiplied by the B-band luminosity to obtain the total stellar mass. The uncertainty in the stellar mass was computed by propagating the photometric uncertainties. We also computed host galaxy masses for the Rossa et al. (2006) sample (nine late-types and ten early types) and the Walcher et al. (2005) sample (nine late-types).

Tight correlations between supermassive black hole (SMBH) masses and large scale properties of their host galaxies, such as the $M_{\rm BH} - \sigma_*$ relation (Ferrarese & Merritt, 2000; Gebhardt et al., 2000), suggest a strong link between processes that grow SMBHs and their host galaxies. It was later discovered that similar correlations between the masses of NCs and their host galaxies (Ferrarese et al., 2006; Wehner & Harris, 2006) also hold. These findings have led to the classification of NCs and SMBHs as central massive objects (CMOs Ferrarese et al., 2006), which suggests that NCs and SMBHs are both generic by-products of galaxy formation, and their growth mechanisms are somehow related. A recent study by Georgiev et al. (2016) explored scaling relations between the sizes and masses of NCs and the stellar mass of their host galaxies, and the dependence of these relations on the morphology of the host galaxy. Here, we briefly compare our results to scaling relations from Georgiev et al. (2016).

[1] http://leda.univ-lyon1.fr/

In Figure 4.11, we plot the stellar mass of the NC against the stellar mass of the host galaxy. We also plot the effective radius of the NC (measured from `GALFIT` modeling of the F814W image) against the stellar mass of the NC in Figure 4.12. The best-fit scaling relations from Georgiev et al. (2016) are shown in Figures 4.11 and 4.12 with a solid line for late-types and a dotted line for early-types. These plots illustrate the remarkable compactness of the NC in IC 342. Although the nucleus of IC 342 is somewhat under-massive given its host galaxy mass (i.e., it sits slightly below the $M_{\rm NC}$-$M_{\rm gal}$ relation), the NC is extremely small, given its mass. The F814W effective radius is 1.4 pc, which corresponds to a mass of $2.6 \times 10^5\ M_\odot$, as predicted by the NC size-mass relation. The actual mass is $1.2 \times 10^7\ M_\odot$, indicating that IC 342 is an extreme outlier in terms of its compactness (the scatter in the NC size-mass relation is only 0.14 dex).

4.3.6 Mass-Metallicity Relation

In this section, we investigate the relation between NC metallicities and the masses of their host galaxies (using the mass estimates outlined in Section 5.5). We plot NC metallicity against host galaxy stellar mass in Figure 4.13, incorporating data from Walcher et al. (2005) and Rossa et al. (2006). NC metallicity appears to increase with host galaxy stellar mass, but there is significant scatter in NC metallicity at a fixed galaxy stellar mass. There are NCs with solar metallicity residing in galaxies with stellar masses ranging from 10^9 to $10^{11} M_\odot$. The Gallazzi et al. (2005) stellar mass-stellar metallicity relation, computed for a sample of 170,000 local galaxies in the Sloan Digital Sky Survey, is also shown on this plot with a solid black line. The scatter in the relation is indicated by black dotted lines.

The NCs are systematically offset from the Gallazzi et al. (2005) relation, with larger metallicities at a fixed galaxy stellar mass. Although we do not have direct measurements of host galaxy metallicities, this result is consistent with NCs being more chemically enriched

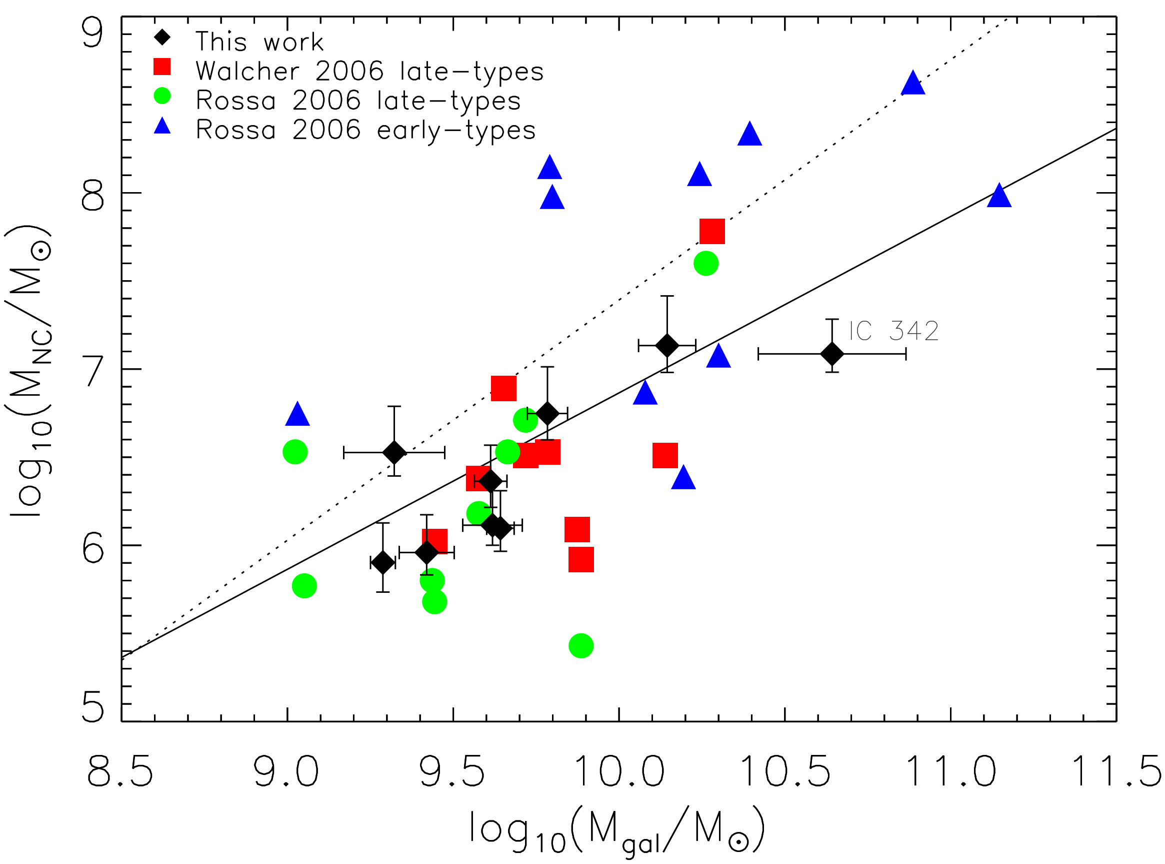

Figure 4.11 NC mass vs. host galaxy stellar mass. The solid line indicates the best-fit relation for late-type galaxies from Georgiev et al. (2016), while the dotted line denotes the best-fit relation for early-types.

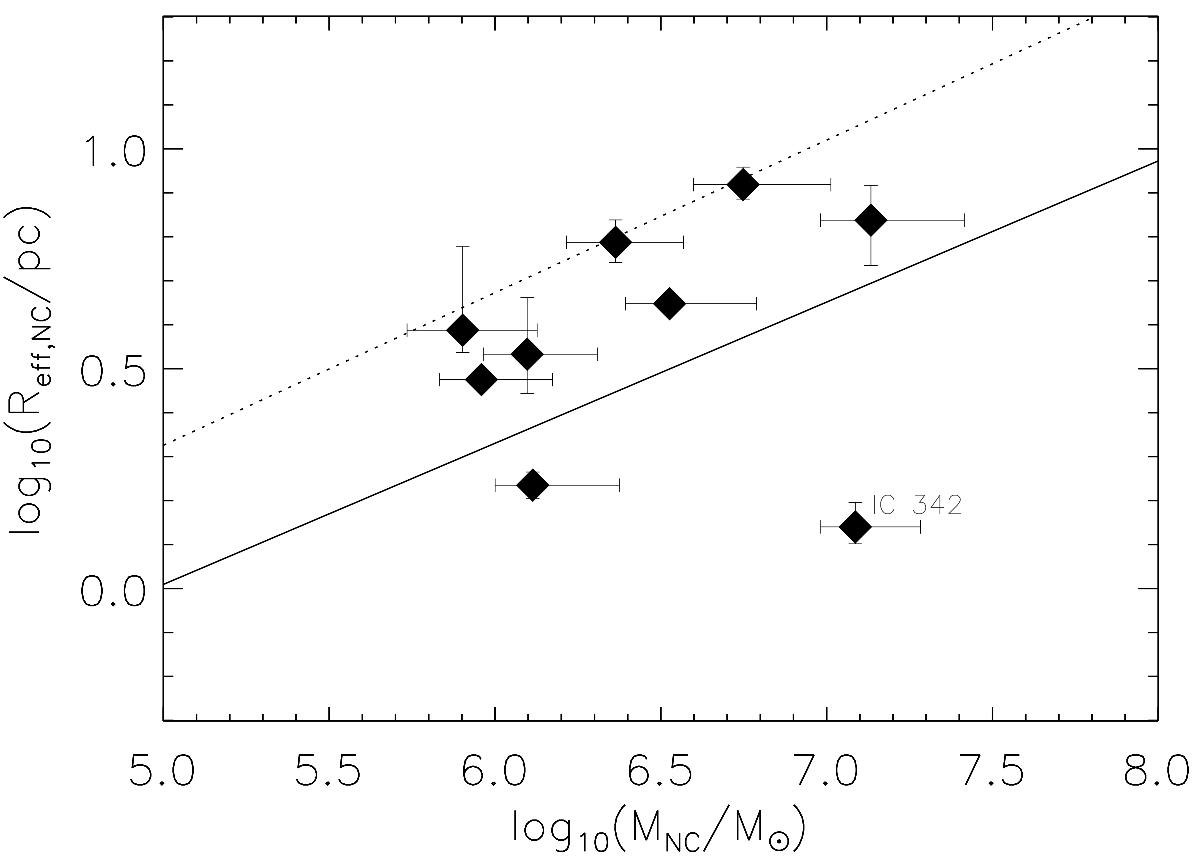

Figure 4.12 NC size vs. mass. The solid line indicates the best-fit relation for late-type galaxies from Georgiev et al. (2016), while the dotted line denotes the best-fit relation for early-types.

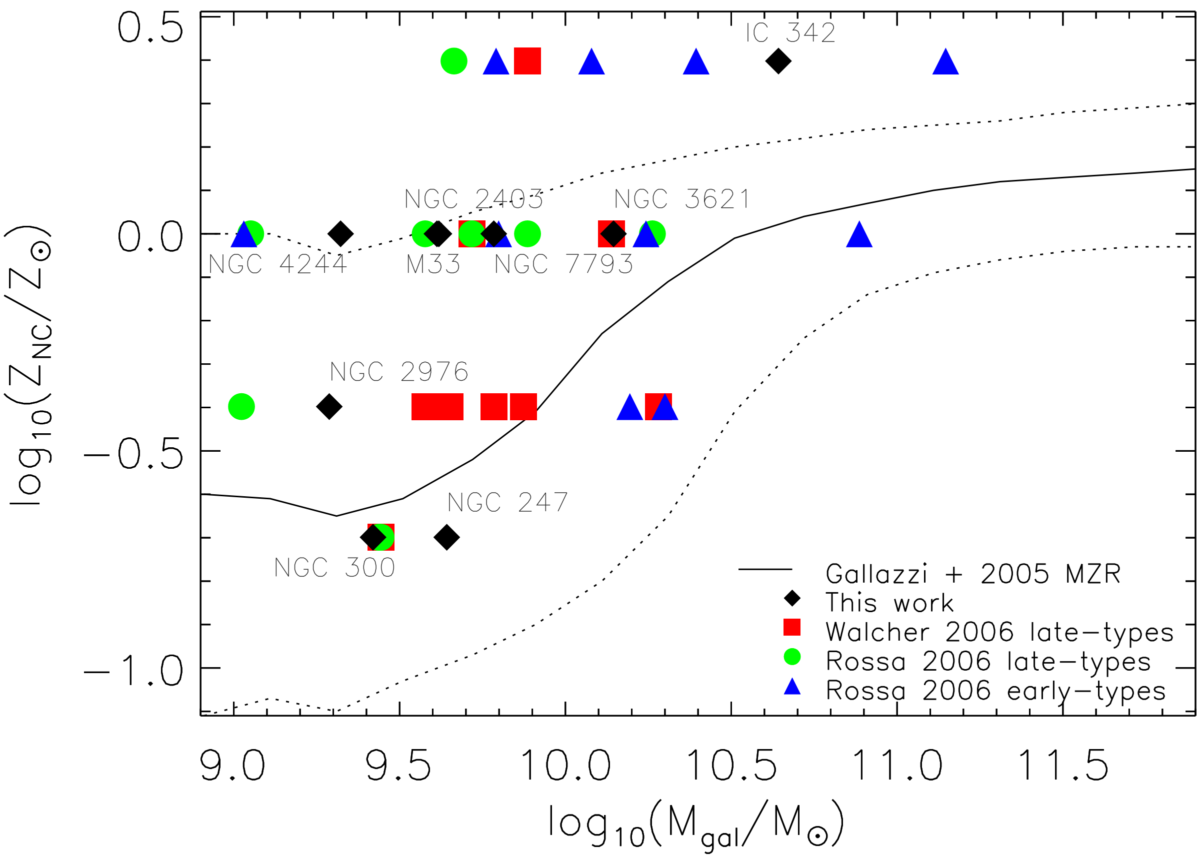

Figure 4.13 NC metallicity vs. host galaxy stellar mass. The Gallazzi et al. (2005) stellar mass-stellar metallicity relation is indicated by the solid black line, and the scatter in the relation is indicated by the dotted black lines.

than their host galaxies. In a study of nucleated dwarf elliptical (dE) galaxies in the Virgo cluster, Paudel et al. (2011) found that dE nuclei are younger (~ 3.5 Gyr) and more metal rich (~ 0.07 dex) than the main bodies of the dEs. Followup spectroscopic observations will be need to confirm that this is also the case for nucleated spiral galaxies. The enhanced chemical enrichment of NCs compared to their host galaxies favors a growth scenario either in which gas is continually accreted onto the nucleus and formed into new stars or younger clusters inspiral inwards and merge with the nucleus, and suggest that the inspiral of old, metal-poor GCs is not the dominant growth mechanism for NCs.

Chapter 5

Conclusions

5.1 Structural Properties

We have analyzed the structure of a sample of ten nuclear star clusters in bulgeless, late-type spiral galaxies by fitting PSF convolved 2D surface brightness models to *HST*/WFC3 images of the clusters in seven wavebands ranging from the near-UV to the near-IR. We find that most of the NCs are described remarkably well by a single Sérsic component, although some show clear evidence for multi-component substructure. NGC 2976 has a NC which consists of a compact, blue structure, which may be a young star cluster and an extended, red population. The NC in NGC 4244 contains a red, compact, spheroidal component and a blue, extended, flattened component. NGC 4395 hosts an unobscured AGN in its NC, which was modeled using a point source component. The main results of the surface brightness profile fits are as follows:

1. The clusters exhibit a wide range of structural properties. In the F814W filter, absolute magnitudes range from -11.20 mag to -15.02 mag, effective radii range from 1.38 to 8.28 pc, Sérsic indices range from 1.63 to 9.73, and axis ratios range from 0.57 to 0.94. We find a

much wider range of Sérsic indices than any previous study, which have generally measured $n \sim 1 - 3$. The highest Sérsic indices we measure (above 6) serve as useful indicators of the shape of the wings of the NC profile, but do not provide information about the core concentration due to the effects of PSF blurring.

2. We find evidence for spatially segregated stellar populations within some clusters. There are color gradients in six of the ten NCs in our sample, indicated by a dependence of the measured effective radius on wavelength. In M33, NGC 247, NGC 300 and NGC 4395, we find an increase in the effective radius with wavelength. This is consistent with general results found by Georgiev & Böker (2014) for a large *HST*/WFPC2 archival sample, and indicates the presence of a younger population which is more concentrated than the bulk of the NC stars. However, we find a general decrease in effective radius with wavelength in NGC 3621 and NGC 7793, which may indicate extended, circumnuclear star formation. For NGC 3621, the larger extent of the NC in UV bands may be due to scattered UV photons originating from the obscured Type 2 AGN.

3. We also find a general trend of increasing roundness of the NCs at longer wavelengths, indicated by larger best-fit axis ratios in redder bands. There is also a correlation between the axis ratios of the NCs and their host galaxies. We conclude that blue disk structures aligned with the host galaxy plane are a common feature of NCs in late-type galaxies, but are more easily detected in galaxies that are close to edge-on.

4. A comparison of the measured colors of the NCs with SSP evolutionary tracks clearly shows that in general, a mix of young and old SSPs is needed to describe their stellar populations, consistent with previous spectroscopic studies of NCs (Rossa et al., 2006; Walcher et al., 2006). The mix of ages is only seen when considering colors which span the UV to the IR, and is not apparent from optical colors alone. The wide wavelength coverage of our data provides sensitivity to stellar populations with a mix of ages.

5.2 Stellar Population Properties

We have developed a SED fitting code that has been demonstrated to accurately recover the mass of stellar systems with a wide range of colors. The code was employed to fit linear combinations of SSPs drawn from four broad age bins (1–10 Myr, 10–100 Myr, 100 Myr–1 Gyr, and 1–13.7 Gyr) to the observed broadband SEDs of a sample of nine nuclear star clusters residing in nearby late-type spiral galaxies. The uncertainties in the best-fit parameters are assessed through a Monte Carlo resampling of SSP templates from the four broad age bins. We have presented global estimates of stellar mass and star formation histories based on fits to the integrated SED of each cluster, as well as maps of stellar density and age based on SED fits performed on a pixel-by-pixel basis. The age and mass estimates derived from integrated SED fits and pixel-by-pixel SED fits are consistent. The primary results of this analysis are as follows:

1. Global star formation histories were derived from the integrated SED fits, none of which are consistent with a constant star formation rate over cosmic time. With the exception of NGC 2403, all NCs in the sample have nonzero star formation rates in at least two age bins. Populations younger than 100 Myr contribute an average of 1.8% of the total stellar mass and 10.4% of the total B-band luminosity. However, these percentages fall to 0.5% and 3.7% when NGC 2976, the only NC in the sample that has undergone any significant star formation in the last 10 Myr, is omitted from the calculation. Young populations with negligible mass fractions can still contribute a significant fraction of the light, and young SSPs are therefore required to fit the observed SEDs accurately. Our results add to a growing body of evidence that NCs experience ongoing star formation throughout their lifetimes.

2. Stellar mass estimates derived from SED fitting are in good agreement with previous dynamical studies. Stellar masses computed from the Bell et al. (2003) and Zibetti et al. (2009) MLCRs are higher than masses obtained via SED fitting by 0.40 dex and 0.32 dex,

respectively. We conclude that multi-band SED fitting is more accurate for estimating NC stellar masses than MLCRs.

3. The age maps produced by the pixel-by-pixel SED fits reveal radial age gradients within the clusters which correspond to the wavelength dependence on the effective radius found in Paper 1. However, radial age gradients were also detected in the NCs for which no wavelength dependence on the effective radius was previously found. We find positive mass-weighted age ($\langle \log_{10}\tau \rangle_{\rm M}$) gradients in M33, NGC 247, and NGC 4244, and a negative $\langle \log_{10}\tau \rangle_{\rm M}$ gradient in NGC 2976. Positive luminosity-weighted age ($\langle \log_{10}\tau \rangle_{{\rm L}_B}$) gradients are found in M33, NGC 247, NGC 300, and NGC 4244, while negative $\langle \log_{10}\tau \rangle_{{\rm L}_B}$ gradients are found in IC 342, NGC 2976, NGC 3621, NGC 7793.

4. We present the first measurements of stellar surface density profiles of nuclear star clusters from spatially resolved stellar population modeling. The measured effective surface densities of the nuclei of IC 342 and NGC 3621 exceed the maximum of $\sim 10^5\ M_\odot\ {\rm pc}^{-2}$ proposed by Hopkins et al. (2010). With an effective surface density of $\Sigma_{\rm eff} = 6.65^{+6.33}_{-1.81} \times 10^5\ M_\odot\ {\rm pc}^{-2}$ within its half-mass radius, the nucleus of IC 342 is the densest stellar system observed to date. The stellar surface density profiles presented in this paper, along with IFU data of the stellar kinematics will be key ingredients in future dynamical studies of nuclear star clusters. These studies will place tighter constraints on the masses of BHs potentially residing within NCs and may uncover a previously unknown population of intermediate-mass black holes. This work will be crucial to progressing our understanding of the demographics of black holes in late-type spiral galaxies.

5. The presence of old, metal-poor populations from accreted globular clusters was investigated by re-running the global SED fits with an additional SSP of age 13.7 Gyr and metallicity $Z = 0.0004$. This increases our stellar mass estimates by 0.13 dex on average. We derive sample-averaged upper limits of 42% and 17% for the contribution of the old, metal-poor population to the total stellar mass and B-band luminosity, respectively. This is

consistent with previous studies by (Agarwal & Milosavljević, 2011; Hartmann et al., 2011; Antonini et al., 2015), which found that the inspiral of old globular clusters is typically a subdominant process in late-type galaxies.

6. We compared the relation between NC metallicities and the masses of their host galaxies to the Gallazzi et al. (2005) stellar mass-stellar metallicity relation for galaxies. NCs sit above the Gallazzi et al. (2005) relation, which is consistent with NCs being more chemically enriched than their host galaxies. This suggests that the inspiral of old, metal-poor GCs is not the dominant growth mechanism for NCs in late-type galaxies.

5.3 Future Work

The density profiles presented in this thesis will be used in conjunction with IFU kinematic data in future dynamical studies of the clusters. Although many of the clusters in our sample have already been targets of past dynamical studies, improvements on dynamical models can be made by incorporating results from spatially resolved stellar population modeling. Previous studies have typically assumed a uniform mass-to-light ratio for the NC, however, we have demonstrated that NCs can exhibit wavelength dependent effective radii, which correspond to age gradients within the clusters. These studies can therefore be improved by allowing for spatially varying mass-to-light ratios.

Dynamical studies of NCs in late-type galaxies will improve our understanding of black hole (BH) demographics in the local universe, and may uncover a previously unseen population of intermediate-mass black holes (IMBHs). An extrapolation of the $M_{\rm BH} - \sigma_*$ or $M_{\rm BH} - M_{\rm bulge}$ relation suggests that NCs in late-type spiral galaxies should harbor IMBHs, with masses $\sim 10^{4-6} M_\odot$. Central BHs in pure disk galaxies are unlikely to have experienced significant growth over cosmic time, and therefore represent a fossilized record of the seeds of present-day supermassive black holes (SMBHs). Constraints on the occupation fraction of IMBHs in late-type galaxies, as well as constraints on the shape of the $M_{\rm BH} - \sigma_*$ relation at the low $M_{\rm BH}$ end, will lead to a better understanding of how SMBHs are ultimately formed.

Nuclear star clusters will be prime targets for the nest generation of ground-based telescopes. The Thirty Meter Telescope (TMT) (Do et al., 2014) and the European Extremely Large Telescope (E-ELT) Gullieuszik et al. (2014) will be able to resolve the kinematics of stars within the sphere of influence of BHs as light as $10^4 M_\odot$, pushing the detection limits for IMBHs towards even lower masses. These telescopes will also be capable of resolving individual bright stars within the nearest NCs, which will help break degeneracies between age, metallicity, and reddening associated with fitting stellar population synthesis models to the integrated cluster light. This improved ability to characterize the stellar populations of NCs and age-date NCs will lead to a clearer picture how NCs form and grow.

With the advent of gravitational wave astronomy (Abbott et al., 2016), detecting the gravitational radiation from a tidal disruption event is now a real possibility. The centers of nearby galaxies hosting SMBHs are obvious places to search for such events. The expected rates of tidal disruption events strongly depend on the innermost stellar densities (e.g., Wang & Merritt, 2004; Merritt, 2009; Brockamp et al., 2011), which are highest in nuclear star clusters. The NC density profiles and central stellar densities presented in this work are therefore important for constraining the role of tidal disruption in the evolution of NCs.

Bibliography

Abbott, B. P., Abbott, R., Abbott, T. D., et al. 2016, Physical Review Letters, 116, 061102

Agarwal, M., & Milosavljević, M. 2011, ApJ, 729, 35

Antonini, F. 2013, ApJ, 763, 62

—. 2014, ApJ, 794, 106

Antonini, F., Barausse, E., & Silk, J. 2015, ApJ, 812, 72

Arca-Sedda, M., & Capuzzo-Dolcetta, R. 2014, MNRAS, 444, 3738

Baillard, A., Bertin, E., de Lapparent, V., et al. 2011, A&A, 532, A74

Barth, A. J., Strigari, L. E., Bentz, M. C., Greene, J. E., & Ho, L. C. 2009, ApJ, 690, 1031

Bekki, K., Couch, W. J., & Drinkwater, M. J. 2001, ApJS, 552, L105

Bekki, K., Couch, W. J., Drinkwater, M. J., & Shioya, Y. 2003, MNRAS, 344, 399

Bell, E. F., & de Jong, R. S. 2001, ApJ, 550, 212

Bell, E. F., McIntosh, D. H., Katz, N., & Weinberg, M. D. 2003, ApJL, 149, 289

Böker, T. 2008, ApJS, 672, L111

Böker, T., Laine, S., van der Marel, R. P., et al. 2002, AJ, 123, 1389

Böker, T., Sarzi, M., McLaughlin, D. E., et al. 2004, AJ, 127, 105

Böker, T., van der Marel, R. P., & Vacca, W. D. 1999, AJ, 118, 831

Bono, G., Caputo, F., Marconi, M., & Musella, I. 2010, ApJ, 715, 277

Brockamp, M., Baumgardt, H., & Kroupa, P. 2011, MNRAS, 418, 1308

Bruzual, G., & Charlot, S. 2003a, MNRAS, 344, 1000

—. 2003b, MNRAS, 344, 1000

Bushouse, H., & Simon, B. 1994, in Astronomical Society of the Pacific Conference Series, Vol. 61, Astronomical Data Analysis Software and Systems III, ed. D. R. Crabtree, R. J. Hanisch, & J. Barnes, 339

Calzetti, D., Armus, L., Bohlin, R. C., et al. 2000, ApJ, 533, 682

Cappellari, M. 2002, MNRAS, 333, 400

Cappellari, M., & Emsellem, E. 2004, PASP, 116, 138

Capuzzo-Dolcetta, R., & Miocchi, P. 2008, MNRAS, 388, L69

Cardelli, J. A., Clayton, G. C., & Mathis, J. S. 1989, ApJ, 345, 245

Carollo, C. M., Stiavelli, M., de Zeeuw, P. T., & Mack, J. 1997, AJ, 114, 2366

Carson, D. J., Barth, A. J., Seth, A. C., et al. 2015, AJ, 149, 170

Chabrier, G. 2003, PASP, 115, 763

Conroy, C., Gunn, J. E., & White, M. 2009, ApJ, 699, 486

Côté, P., Piatek, S., Ferrarese, L., et al. 2006, ApJL, 165, 57

Crowther, P. A., Schnurr, O., Hirschi, R., et al. 2010, MNRAS, 408, 731

De Lorenzi, F., Hartmann, M., Debattista, V. P., Seth, A. C., & Gerhard, O. 2013, MNRAS, 429, 2974

de Meulenaer, P., Narbutis, D., Mineikis, T., & Vansevičius, V. 2014, A&A, 569, A4

de Vaucouleurs, G., de Vaucouleurs, A., Corwin, Jr., H. G., et al. 1991, Third Reference Catalogue of Bright Galaxies. Volume I: Explanations and references. Volume II: Data for galaxies between 0^h and 12^h. Volume III: Data for galaxies between 12^h and 24^h.

den Brok, M., Seth, A. C., Barth, A. J., et al. 2015, ApJ, 809, 101

Do, T., Wright, S. A., Barth, A. J., et al. 2014, AJ, 147, 93

Dressel, L. 2012, Wide Field Camera 3 Instrument Handbook for Cycle 21 v. 5.0

Edri, H., Rafter, S. E., Chelouche, D., Kaspi, S., & Behar, E. 2012, ApJ, 756, 73

Elson, R. A. W. 1999, in Globular Clusters, ed. C. Martínez Roger, I. Perez Fournón, & F. Sánchez, 209–248

Emsellem, E., Monnet, G., & Bacon, R. 1994, A&A, 285

Feldmeier-Krause, A., Neumayer, N., Schödel, R., et al. 2015, A&A, 584, A2

Ferrarese, L., & Merritt, D. 2000, ApJS, 539, L9

Ferrarese, L., Côté, P., Dalla Bontà, E., et al. 2006, ApJS, 644, L21

Filippenko, A. V., & Ho, L. C. 2003, ApJS, 588, L13

Filippenko, A. V., Ho, L. C., & Sargent, W. L. W. 1993, ApJS, 410, L75

Filippenko, A. V., & Sargent, W. L. W. 1989, ApJS, 342, L11

Fioc, M., & Rocca-Volmerange, B. 1997, A&A, 326, 950

Fischer, T. C., Crenshaw, D. M., Kraemer, S. B., & Schmitt, H. R. 2013, ApJL, 209, 1

Foschini, L., Rodriguez, J., Fuchs, Y., et al. 2004, A&A, 416, 529

Freudling, W. 1993, in European Southern Observatory Conference and Workshop Proceedings, Vol. 47, European Southern Observatory Conference and Workshop Proceedings, ed. P. Grosbol & R. de Ruijsscher, 27

Gallazzi, A., & Bell, E. F. 2009, ApJL, 185, 253

Gallazzi, A., Charlot, S., Brinchmann, J., White, S. D. M., & Tremonti, C. A. 2005, MNRAS, 362, 41

Gebhardt, K., Bender, R., Bower, G., et al. 2000, ApJS, 539, L13

Gebhardt, K., Lauer, T. R., Kormendy, J., et al. 2001, AJ, 122, 2469

Georgiev, I. Y., & Böker, T. 2014, MNRAS, 441, 3570

Georgiev, I. Y., Böker, T., Leigh, N., Lützgendorf, N., & Neumayer, N. 2016, MNRAS, 457, 2122

Gil de Paz, A., Boissier, S., Madore, B. F., et al. 2007, ApJL, 173, 185

Gliozzi, M., Satyapal, S., Eracleous, M., Titarchuk, L., & Cheung, C. C. 2009, ApJ, 700, 1759

Graham, A. W., & Spitler, L. R. 2009, MNRAS, 397, 2148

Gullieuszik, M., Greggio, L., Falomo, R., Schreiber, L., & Uslenghi, M. 2014, A&A, 568, A89

Häring, N., & Rix, H.-W. 2004, ApJS, 604, L89

Hartmann, M., Debattista, V. P., Seth, A., Cappellari, M., & Quinn, T. R. 2011, MNRAS, 418, 2697

Hemmati, S., Miller, S. H., Mobasher, B., et al. 2014, ApJ, 797, 108

Ho, L. C., Li, Z.-Y., Barth, A. J., Seigar, M. S., & Peng, C. Y. 2011, ApJL, 197, 21

Hopkins, P. F., Murray, N., Quataert, E., & Thompson, T. A. 2010, MNRAS, 401, L19

Jacobs, B. A., Rizzi, L., Tully, R. B., et al. 2009, AJ, 138, 332

Jarrett, T. H., Chester, T., Cutri, R., Schneider, S. E., & Huchra, J. P. 2003, AJ, 125, 525

Jedrzejewski, R. I. 1987, MNRAS, 226, 747

Kaviraj, S., Rey, S.-C., Rich, R. M., Yoon, S.-J., & Yi, S. K. 2007, MNRAS, 381, L74

Kelly, B. C. 2007, ApJ, 665, 1489

Kormendy, J., Drory, N., Bender, R., & Cornell, M. E. 2010, ApJ, 723, 54

Kormendy, J., & Ho, L. C. 2013, ARA&A, 51, 511

Kormendy, J., & McClure, R. D. 1993, AJ, 105, 1793

Krist, J. 1993, in Astronomical Society of the Pacific Conference Series, Vol. 52, Astronomical Data Analysis Software and Systems II, ed. R. J. Hanisch, R. J. V. Brissenden, & J. Barnes, 536

Krist, J. E., Hook, R. N., & Stoehr, F. 2011, in Society of Photo-Optical Instrumentation Engineers (SPIE) Conference Series, Vol. 8127, Society of Photo-Optical Instrumentation Engineers (SPIE) Conference Series

Lanyon-Foster, M. M., Conselice, C. J., & Merrifield, M. R. 2007, MNRAS, 380, 571

Larsen, S. S. 1999, A&AS, 139, 393

Lauer, T. R., Faber, S. M., Ajhar, E. A., Grillmair, C. J., & Scowen, P. A. 1998, AJ, 116, 2263

Lauer, T. R., Ajhar, E. A., Byun, Y.-I., et al. 1995, AJ, 110, 2622

Lira, P., Johnson, R. A., Lawrence, A., & Cid Fernandes, R. 2007, MNRAS, 382, 1552

Lira, P., Lawrence, A., O'Brien, P., et al. 1999, MNRAS, 305, 109

Lotz, J. M., Telford, R., Ferguson, H. C., et al. 2001, ApJ, 552, 572

Lu, J. R., Do, T., Ghez, A. M., et al. 2013, ApJ, 764, 155

Lyubenova, M., van den Bosch, R. C. E., Côté, P., et al. 2013, MNRAS, 431, 3364

Makarov, D., Prugniel, P., Terekhova, N., Courtois, H., & Vauglin, I. 2014, A&A, 570, A13

Markwardt, C. B. 2009, in Astronomical Society of the Pacific Conference Series, Vol. 411, Astronomical Data Analysis Software and Systems XVIII, ed. D. A. Bohlender, D. Durand, & P. Dowler, 251

Matthews, L. D., & Gallagher, III, J. S. 1997, AJ, 114, 1899

Matthews, L. D., Gallagher, III, J. S., Krist, J. E., et al. 1999, AJ, 118, 208

McCall, M. L. 1989, AJ, 97, 1341

McGaugh, S. S., & Schombert, J. M. 2014, AJ, 148, 77

Menezes, R. B., Steiner, J. E., & da Silva, P. 2016, ApJ, 817, 150

Merritt, D. 2009, ApJ, 694, 959

Merritt, D., Ferrarese, L., & Joseph, C. L. 2001, Science, 293, 1116

Mieske, S., Frank, M. J., Baumgardt, H., et al. 2013, A&A, 558, A14

Milosavljević, M. 2004, ApJS, 605, L13

Minezaki, T., Yoshii, Y., Kobayashi, Y., et al. 2006, ApJS, 643, L5

Mobasher, B., Dahlen, T., Ferguson, H. C., et al. 2015, ApJ, 808, 101

Monaco, L., Bellazzini, M., Ferraro, F. R., & Pancino, E. 2005, MNRAS, 356, 1396

Monaco, L., Saviane, I., Perina, S., et al. 2009, A&A, 502, L9

Moustakas, J., & Kennicutt, Jr., R. C. 2006, ApJL, 164, 81

Muratov, A. L., & Gnedin, O. Y. 2010, ApJ, 718, 1266

Neumayer, N., & Walcher, C. J. 2012, Advances in Astronomy, 2012, arXiv:1201.4950

Paudel, S., Lisker, T., & Kuntschner, H. 2011, MNRAS, 413, 1764

Paumard, T., Genzel, R., Martins, F., et al. 2006, ApJ, 643, 1011

Peng, C. Y., Ho, L. C., Impey, C. D., & Rix, H.-W. 2002, AJ, 124, 266

—. 2010, AJ, 139, 2097

Peterson, B. M., Bentz, M. C., Desroches, L.-B., et al. 2005, ApJ, 632, 799

Phillipps, S., Drinkwater, M. J., Gregg, M. D., & Jones, J. B. 2001, ApJ, 560, 201

Phillips, A. C., Illingworth, G. D., MacKenty, J. W., & Franx, M. 1996, AJ, 111, 1566

Pietrzyński, G., Gieren, W., Hamuy, M., et al. 2010, AJ, 140, 1475

Pozzetti, L., & Mannucci, F. 2000, MNRAS, 317, L17

Roediger, J. C., & Courteau, S. 2015, MNRAS, 452, 3209

Rossa, J., van der Marel, R. P., Böker, T., et al. 2006, AJ, 132, 1074

Saha, A., Claver, J., & Hoessel, J. G. 2002, AJ, 124, 839

Saha, A., Thim, F., Tammann, G. A., Reindl, B., & Sandage, A. 2006, ApJL, 165, 108

Salpeter, E. E. 1955, ApJ, 121, 161

Sandoval, M. A., Vo, R. P., Romanowsky, A. J., et al. 2015, ApJS, 808, L32

Sarzi, M., Rix, H.-W., Shields, J. C., et al. 2005, ApJ, 628, 169

Satyapal, S., Vega, D., Heckman, T., O'Halloran, B., & Dudik, R. 2007, ApJS, 663, L9

Schlafly, E. F., & Finkbeiner, D. P. 2011, ApJ, 737, 103

Schödel, R., Feldmeier, A., Kunneriath, D., et al. 2014, A&A, 566, A47

Sérsic, J. L. 1968, Atlas de galaxias australes

Seth, A., Agüeros, M., Lee, D., & Basu-Zych, A. 2008a, ApJ, 678, 116

Seth, A. C., Blum, R. D., Bastian, N., Caldwell, N., & Debattista, V. P. 2008b, ApJ, 687, 997

Seth, A. C., Dalcanton, J. J., Hodge, P. W., & Debattista, V. P. 2006, AJ, 132, 2539

Seth, A. C., Cappellari, M., Neumayer, N., et al. 2010, ApJ, 714, 713

Seth, A. C., van den Bosch, R., Mieske, S., et al. 2014, Nature, 513, 398

Siegel, M. H., Dotter, A., Majewski, S. R., et al. 2007, ApJS, 667, L57

Skrutskie, M. F., Cutri, R. M., Stiening, R., et al. 2006, AJ, 131, 1163

Strader, J., Seth, A. C., Forbes, D. A., et al. 2013, ApJS, 775, L6

Thim, F., Hoessel, J. G., Saha, A., et al. 2004, AJ, 127, 2322

Tremaine, S. D., Ostriker, J. P., & Spitzer, Jr., L. 1975, ApJ, 196, 407

Trinchieri, G., Fabbiano, G., & Peres, G. 1988, ApJ, 325, 531

Volonteri, M., Lodato, G., & Natarajan, P. 2008, MNRAS, 383, 1079

Walcher, C. J., Böker, T., Charlot, S., et al. 2006, ApJ, 649, 692

Walcher, C. J., van der Marel, R. P., McLaughlin, D., et al. 2005, ApJ, 618, 237

Wang, J., & Merritt, D. 2004, ApJ, 600, 149

Wehner, E. H., & Harris, W. E. 2006, ApJS, 644, L17

Welikala, N., Connolly, A. J., Hopkins, A. M., & Scranton, R. 2009, ApJ, 701, 994

Welikala, N., Connolly, A. J., Hopkins, A. M., Scranton, R., & Conti, A. 2008, ApJ, 677, 970

Worthey, G. 1994, ApJL, 95, 107

Wuyts, S., Förster Schreiber, N. M., Genzel, R., et al. 2012, ApJ, 753, 114

Yukita, M., Swartz, D. A., Soria, R., & Tennant, A. F. 2007, ApJ, 664, 277

Zepf, S. E., & Ashman, K. M. 1993, MNRAS, 264, 611

Zibetti, S., Charlot, S., & Rix, H.-W. 2009, MNRAS, 400, 1181

Appendix A

Developing and Testing the SED Fitting Code

A.1 Model Fitting Procedure

Several spectroscopic studies of NCs (e.g., Sarzi et al., 2005; Walcher et al., 2006; Rossa et al., 2006; Seth et al., 2006) have demonstrated that NCs are not generally well described by single-age models. These studies have taken advantage of the fact that a stellar system with an arbitrarily complex star formation history can be modeled with a superposition of single-age stellar populations. Fitting linear combinations of SSP model spectra to the observed spectra of NCs is an effective way to infer their star formation histories, metallicities, and dust extinctions. However, this method requires that the models contain a sufficient number of SSP components to describe the extended star formation histories of NCs. For example, the Rossa et al. (2006) and Walcher et al. (2006) studies both used 14 SSP components. The SEDs we constructed from *HST* imaging data only contain seven photometric data points, which limits the number of SSP components that we can include in our models. As a consequence, the precision with which we can infer the star formation histories of the NCs in our sample is also limited. In order for our models to account for star formation episodes as old as 13.7 Gyr all the way to the present day while limiting the number of free parameters, it is necessary to bin the SSP templates by age.

We experimented with using different numbers of age bins in our Monte Carlo SED fitting code in order to determine the optimal number of SSP components to use in our models. First, we divided the ages of the BC03 SSP templates into n equally log-spaced bins, then performed 10^4 Monte Carlo realizations of the SED fit for each NC in our sample. In each realization, one SSP template is selected at random from each of the n age bins and a χ^2 fit to the observed SED is performed to determine the best-fit linear combination of SSP templates. To quantify the goodness-of-fit, we recorded the median value of χ^2 among the 10^4 Monte Carlo realizations for each NC. This process was carried out for $n = 1$–10 age bins (for $n = 1$, a *single* SSP template between 1 Myr and 13.7 Gyr is randomly drawn in each realization of the fit). In Figure A.1, we plot the median value of χ^2 among the 10^4 realizations against the number of age bins used in the fit. The dotted lines in this plot denote individual NCs in our sample, while the solid line denotes the median of the sample. The goodness-of-fit rapidly improves between $n = 1$ and $n = 4$. However, there are diminishing returns for adding complexity to the models beyond $n = 4$, since χ^2 only improves marginally after adding SSP components. In order to avoid over-fitting while still allowing for the possibility of complex star formation histories, we settled on $n = 4$ age bins.

Another way to assess the number of SSP templates needed in our models is to investigate how well the SSP templates can be differentiated from one another using our set of seven *HST* filters. As explained in Section 4.1.1, we simulated *HST*/WFC3 observations to construct broadband SEDs with seven photometric data points for each template. We first scaled the photometric SEDs of the full set of 300 BC03 SSP models so that they all have equal bolometric luminosity. One SSP is then selected as a comparison template, which will be

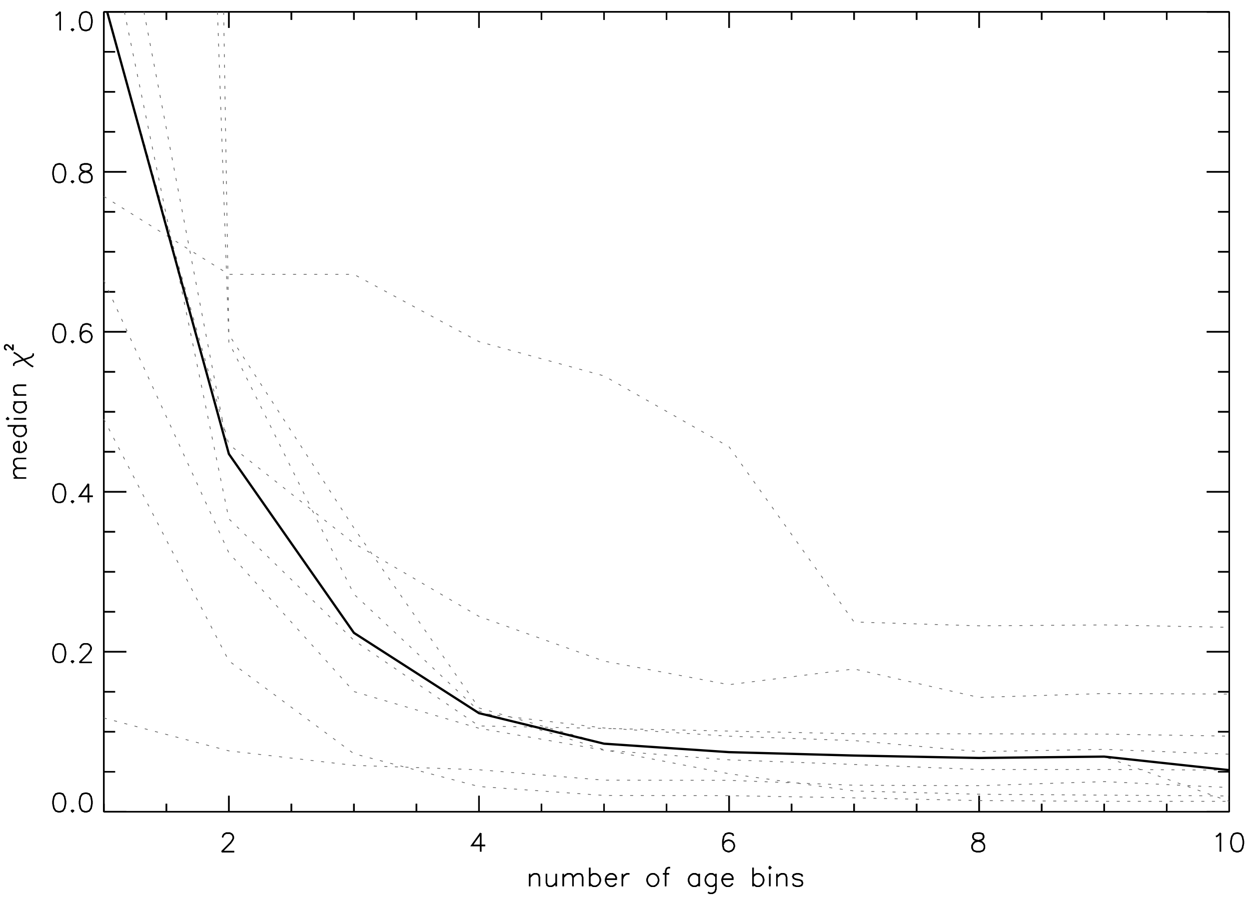

Figure A.1 The median value of χ^2 among the 10^4 Monte Carlo realizations of the SED fit vs. the number of age bins used in the fit. The dotted lines denote individual NCs, while the solid line denotes the median.

paired with all other SSPs in the set to assess their similarities. For each of the 300 SSP templates in the set, we counted the number of WFC3 bands for which there is a 3σ or greater discrepancy in L_λ with the comparison template. Here, σ represents the average photometric uncertainty in a given band. Figure A.2 shows a map of 3σ mismatches in the SSP age-metallicity plane, for four different comparison templates: a 3.5 Myr SSP, a 35 Myr SSP, a 350 Myr SSP, and a 3.5 Gyr SSP (all with $Z = 0.008$). The ages of these comparison templates correspond to the centers of the four log-spaced age bins used in our Monte Carlo SED fitting code (1–10 Myr, 10–100 Myr, 100 Myr–1 Gyr, and 1–13.7 Gyr). The black regions in Figure A.2, which indicate SSPs for which there is a perfect match with the comparison template at the 3σ confidence level, span ~ 1 dex in SSP age for each of the comparison templates. This demonstrates the fact that we can only infer star formation histories with coarse time resolution with our WFC3 filter set, and is consistent with our finding that the goodness-of-fit only marginally improves with the inclusion of additional SSP templates beyond $n = 4$.

A.2 Testing the SED Fitting Method

In order to verify that our method is capable of accurately recovering the masses, ages, and reddenings of NCs, we tested our code on a set of mock SEDs, a strategy employed by Mobasher et al. (2015). Comparing the known input masses to the mass estimates output by the code for a large set of mock SEDs with a wide range of spectral shapes is a good way to test the robustness of our SED fitting method and to identify potential failure modes. Our mock SEDs were created using linear combinations of BC03 SSP templates with reddening applied according to the Calzetti et al. (2000) reddening law.

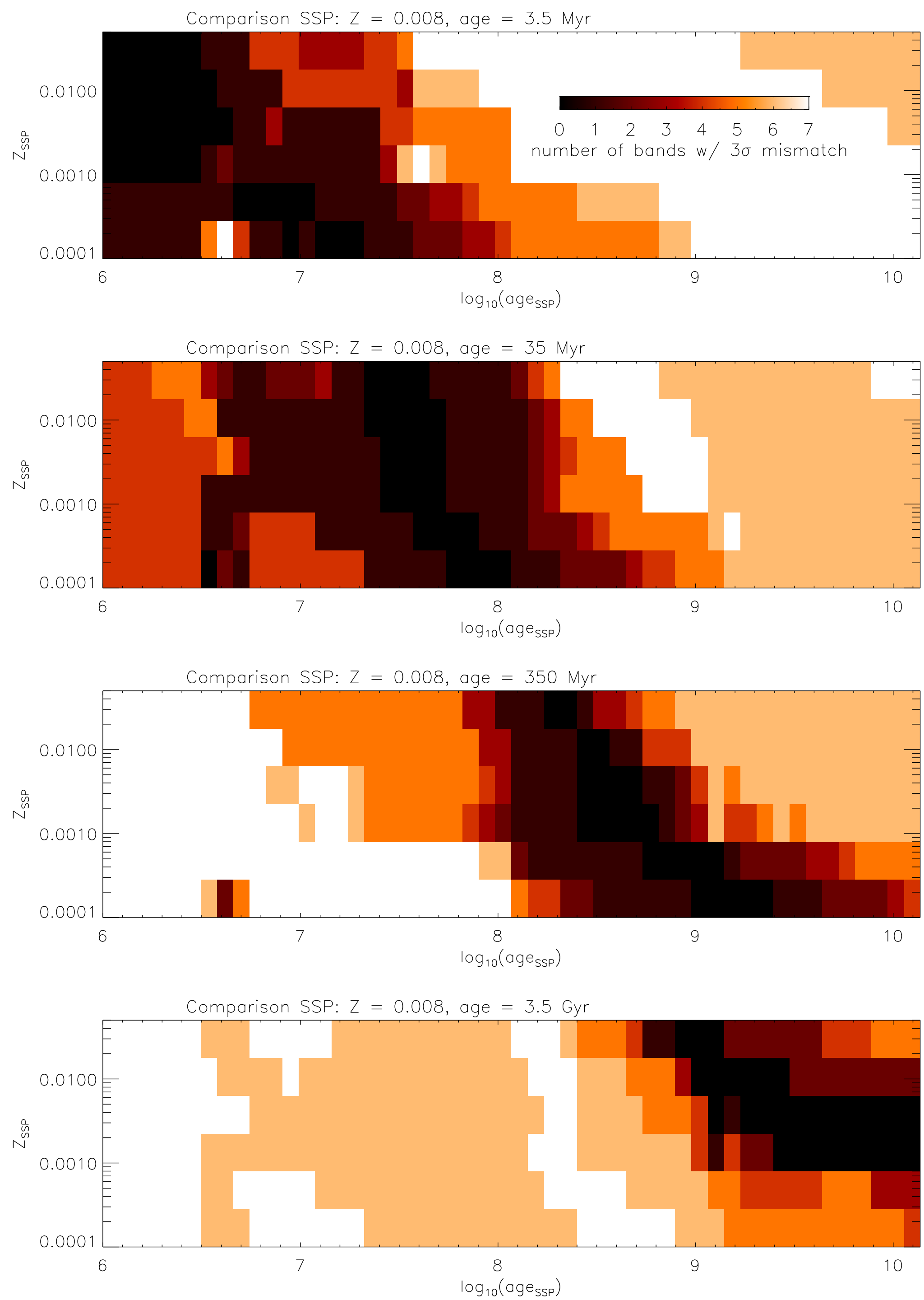

Figure A.2 Maps of 3σ mismatches with the comparison template in the SSP age-metallicity plane. For four different comparison templates with metallicity $Z = 0.008$ were used (from top to bottom): a 3.5 Myr SSP, a 35 Myr SSP, a 350 Myr SSP, and a 3.5 Gyr SSP. Black regions correspond to SSPs that match the comparison template at the 3σ confidence level in every filter. White regions correspond to SSPs for which there is a 3σ discrepancy with the comparison template in every filter.

A.2.1 Tests on Single-Age Models

We first tested our code on a set of 50 BC03 SSP templates with solar metallicity $Z = 0.02$, $E(B - V) = 0.1$, and ages ranging from 1 Myr to 13.7 Gyr (logarthimically spaced). To simulate real observations, we added Gaussian noise to each SSP, which was determined from the average uncertainty on the NC luminosity in each band. The typical uncertainty on NC luminosity, averaged over all NCs and all bands, is 10%. As discussed in Paper 1, the dominant source of uncertainty is not photon counting error, but rather the degeneracy between the host galaxy and NC light. For each SSP, we performed 10^5 iterations of the Monte Carlo fit described in Section 4.1.1 and computed the mass corresponding to the median of the likelihood distribution. In Figure A.3, we plot the ratio of the computed output mass and the known input mass, $\log_{10}(M_{\rm out}/M_{\rm in})$, against the age of the input SSP.

The $\log_{10}(M_{\rm out}/M_{\rm in}) = 0$ line almost always lies within the 1σ confidence interval for SSP ages > 20 Myr. However, the code clearly fails to reliably recover the known mass for SSPs younger than 20 Myr. In particular, there is a failure mode that occurs for SSP ages ~ 8 Myr that causes the code to overestimate the stellar mass by over an order of magnitude. The degeneracy responsible for this failure mode is illustrated in Figure A.4. Here we plot the full-resolution spectrum of a 8.5 Myr SSP (shown in blue), as well as a linear combination of a 3.5 Myr and a 3.5 Gyr SSP template, where the 3.5 Gyr template accounts for 99.5% of the total stellar mass (shown in red). The broadband SEDs of the NCs in our sample are also plotted. The spectra of the 8 Myr SSP and the 3.5 Myr/3.5 Gyr mix are remarkably similar, and would be indistinguishable if observed using broadband photometry. If the input SED is a ~ 8 Myr SSP, either one will give an equally good fit. However, these populations have vastly different mass-to-light ratios, and as a consequence the code tends to overestimate the total stellar mass. As shown in A.4, none of the NCs in our sample have sufficiently blue spectral shapes to be sensitive to this degenceracy. We conclude that our Monte Carlo SED fitting method fails to accurately recover the stellar mass for very young (< 20 Myr) stellar

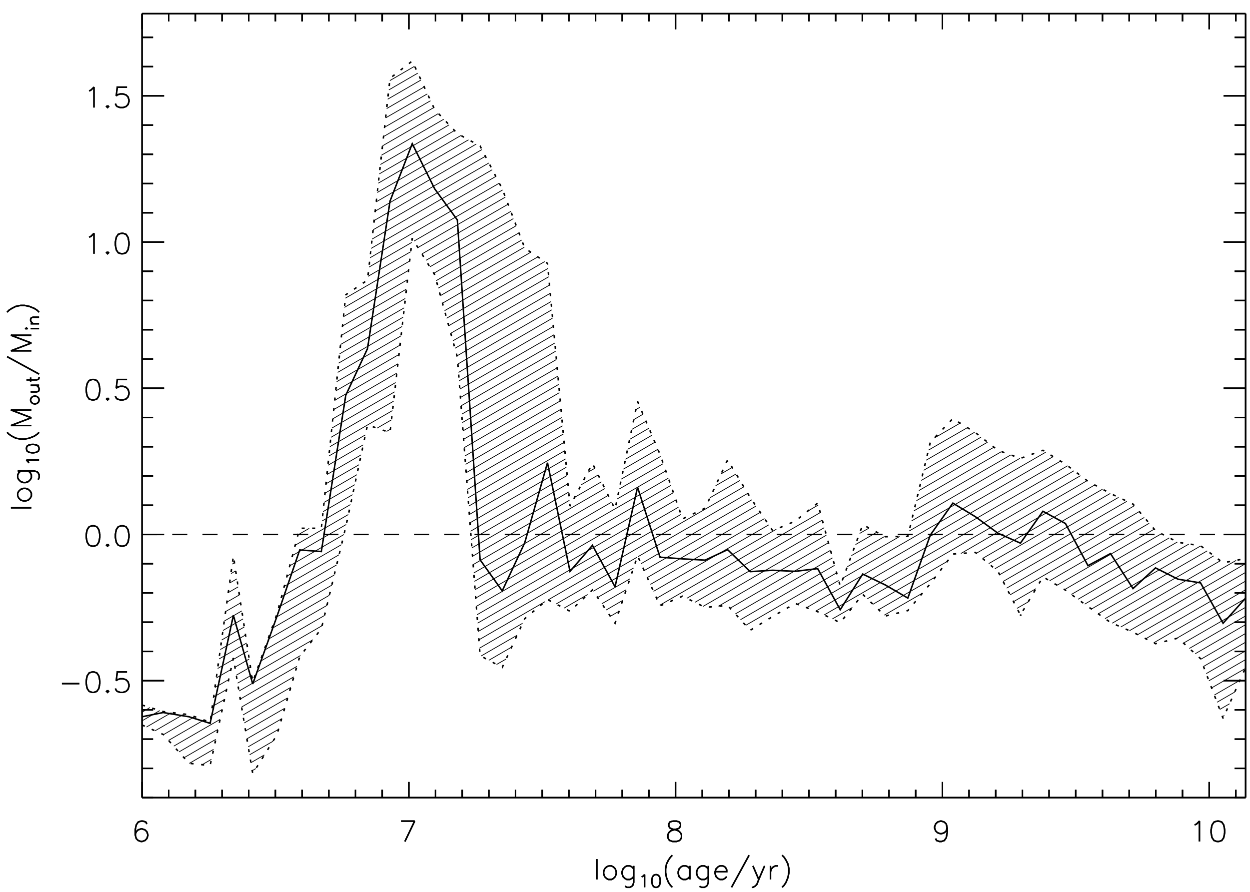

Figure A.3 Ratio of the output mass and input mass, $\log_{10}(M_{\rm out}/M_{\rm in})$, against the age of the input SSP. The shaded region denotes the 1σ confidence interval of the output mass.

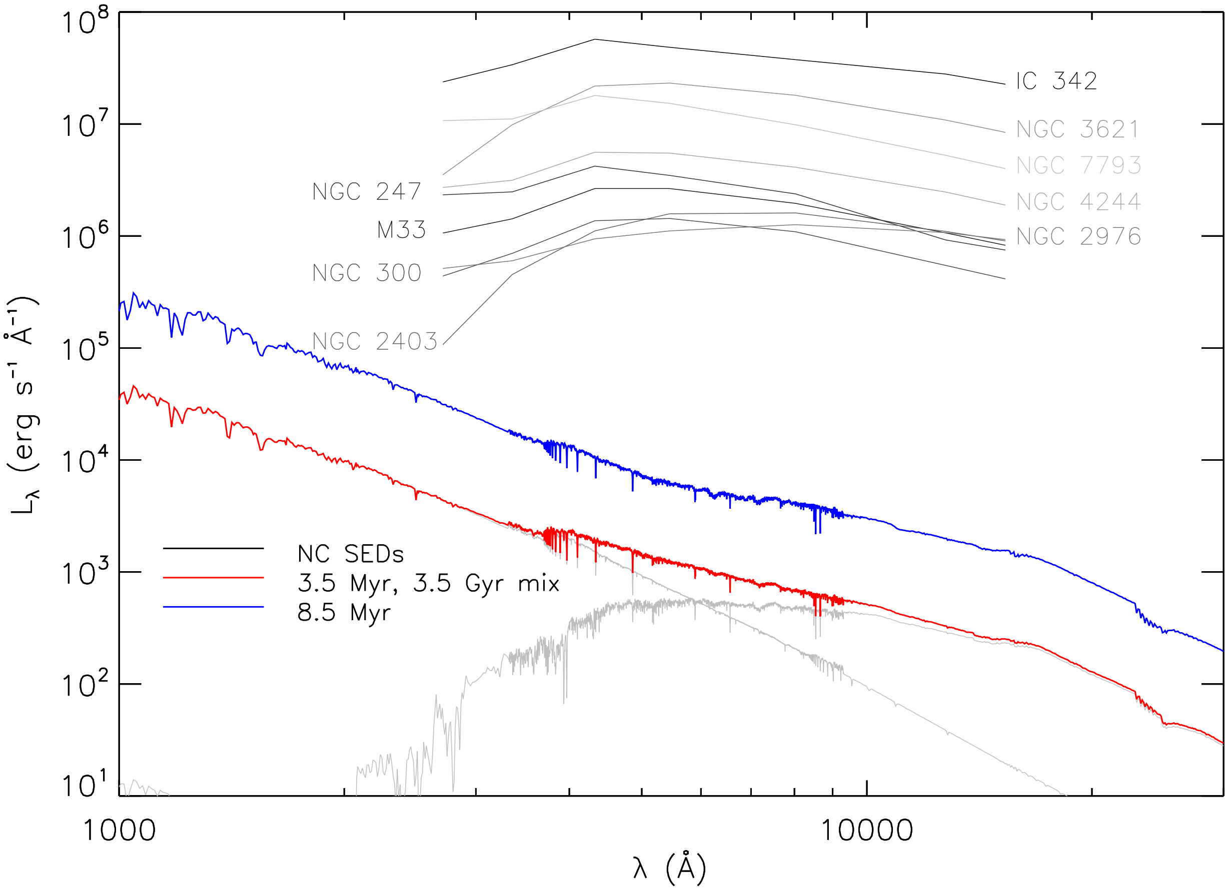

Figure A.4 In blue: full-resolution spectrum of a 8.5 Myr SSP. In red: mix of a 3.5 Myr and a 3.5 Gyr SSP (99.5% of the total stellar mass is in the 3.5 Gyr SSP). In gray: individual components of the 3.5 Myr/3.5 Gyr mix. We also plot the broadband SEDs of the NCs in our sample.

systems, but this is unlikely to have affected the results for our sample of NCs.

Figure A.3 also illustrates a less significant systematic bias, namely that our method underestimates the stellar mass for the oldest (> 4 Gyr) SSPs. This is simply an unavoidable consequence of drawing the SSP templates that compose the model SED from 4 broad age bins. In each iteration of the fit, an SSP template in the 1-13.7 Gyr age bin will be drawn at random. If the input SSP is older than the median age in the $1 - 13.7$ Gyr bin, the randomly drawn template is most likely to be younger than the input SSP. Even if the χ^2fit puts all of the weight in the oldest age bin, the mass will be underestimated, because M/L

monotonically increases across the 1-13.7 Gyr age bin. Similarly, our method underestimates the mass for the youngest (< 4 Myr) SSPs, because M/L monotonically *decreases* between 1 and 4 Myr.

A.2.2 Mock Catalog Based on Walcher 2006 Sample

To test the code on SEDs more representative of typical NCs containing multi-age populations, we created a catalog of mock SEDs based on the Walcher et al. (2006) study (the fractional linear mass weights of the SSPs in each composite fit are listed in Table 6). The procedure for creating the catalog is as follows: (1) A NC from the Walcher et al. (2006) sample is selected at random. (2) Without allowing the weight to go negative, each fractional linear mass weight in the composite SSP model (w_i) is modified by $w_i(1 + 0.1 \times N(0, 1))$, where $N(0, 1)$ is the normal distribution with a mean of 0 and a dispersion of 1. (3) The age of each SSP is shifted by $N(0, 4)$ time steps. (4) The reddening is modified by $E(B-V)(1 + 0.05 \times N(0, 1))$. (5) Gaussian random noise is applied to the mock SED. As before, the Gaussian random noise is determined from the average uncertainty on NC luminosity in each band. All mock SEDs in the catalog are assigned a single, uniform metallicity of $Z = 0.02$. We repeat this procedure to produce a catalog of 1000 mock SEDs. The resulting catalog is a good representation of observations of a diverse sample NCs in late-type spiral galaxies. We perform 10^4 iterations of the Monte Carlo fit on each mock SED.

In Figure A.5, we show histograms of the discrepancy between the input and output values of stellar mass, $\langle \log_{10}\tau \rangle_{\mathrm{M}}$, $\langle \log_{10}\tau \rangle_{\mathrm{L}_B}$, and $E(B-V)$ from the mock SED fits. For the mass, the discrepancy is defined as $\log_{10}(M_{\mathrm{out}}/M_{\mathrm{in}})$, while for the logarithmic quantities, the discrepancies are defined as $\langle \log_{10}\tau \rangle_{\mathrm{M,out}} - \langle \log_{10}\tau \rangle_{\mathrm{M,in}}$, $\langle \log_{10}\tau \rangle_{\mathrm{L}_B\mathrm{,out}} - \langle \log_{10}\tau \rangle_{\mathrm{L}_B\mathrm{,in}}$, and $E(B-V)_{\mathrm{out}} - E(B-V)_{\mathrm{in}}$. The mean value of the discrepancy (bias) and the corresponding standard deviation (scatter) of each quantity is given in the plots in Figure A.5. The bias of our mass estimates is −0.16 dex and the corresponding scatter is 0.33 dex, which is comparable to the average of the symmetrized uncertainties in the mass estimates listed in Table 4.1, 0.22 dex. This indicates that our method produces accurate stellar mass estimates with realistic uncertainties. The reddening estimates show little bias (+0.03 dex), while the level of bias in the $\langle \log_{10}\tau \rangle_{\rm M}$ and $\langle \log_{10}\tau \rangle_{{\rm L}_B}$ estimates (−0.10 dex and +0.20 dex) is acceptable given that the age bins used in the Monte Carlo SED fits each span 1 dex. The mass-weighted age estimates show more scatter than the luminosity-weighted age estimates because underlying old populations can account for a significant fraction of the total mass, while contributing a negligible fraction of the total luminosity. The average of the symmetrized uncertainties in $\langle \log_{10}\tau \rangle_{\rm M}$ and $\langle \log_{10}\tau \rangle_{{\rm L}_B}$ for the sample are 0.42 dex and 0.18 dex, respectively.

Although the age estimates are generally accurate, there are long tails in the $\langle \log_{10}\tau \rangle_{\rm M,out} - \langle \log_{10}\tau \rangle_{\rm M,in}$ distribution plotted in Figure A.5. In order to understand why the method sometimes fails to produce accurate age estimates, we identified all cases where $|\langle \log_{10}\tau \rangle_{\rm M,out} - \langle \log_{10}\tau \rangle_{\rm M,in}| > 2$ dex (this occurs in 21 of the 1000 mock SEDs tested) and examined the input and output SEDs. Despite how poorly we reconstruct the star formation history in these cases, the output SEDs generally provide a good fit to the input SEDs. In every case for which $|\langle \log_{10}\tau \rangle_{\rm M,out} - \langle \log_{10}\tau \rangle_{\rm M,in}| > 2$ dex, the input SED peaks in the UV, indicating that young populations dominate the light (but not necessarily the mass). Since the mass-to-light ratio increases by over 4 orders of magnitude as an SSP evolves from 1 Myr to 13.7 Gyr, the fits are not very sensitive to the amount of mass in the oldest age bin when the SED is dominated by a young and luminous population. However, the NCs in our sample do not have sufficiently blue spectral shapes to be susceptible to this failure mode. The bluest cluster in the sample has a F275W − F547M color of 0.41 mag, while the mean F275W − F547M color of the mock SEDs for which the age estimates fail badly (i.e., 2 dex discrepancy or greater between the output and input values of $\langle \log_{10}\tau \rangle_{\rm M}$) is −1.91 mag. For populations with $U - V$ colors redder than ~ -2 mag, our method gives unbiased mass age, and reddening estimates.

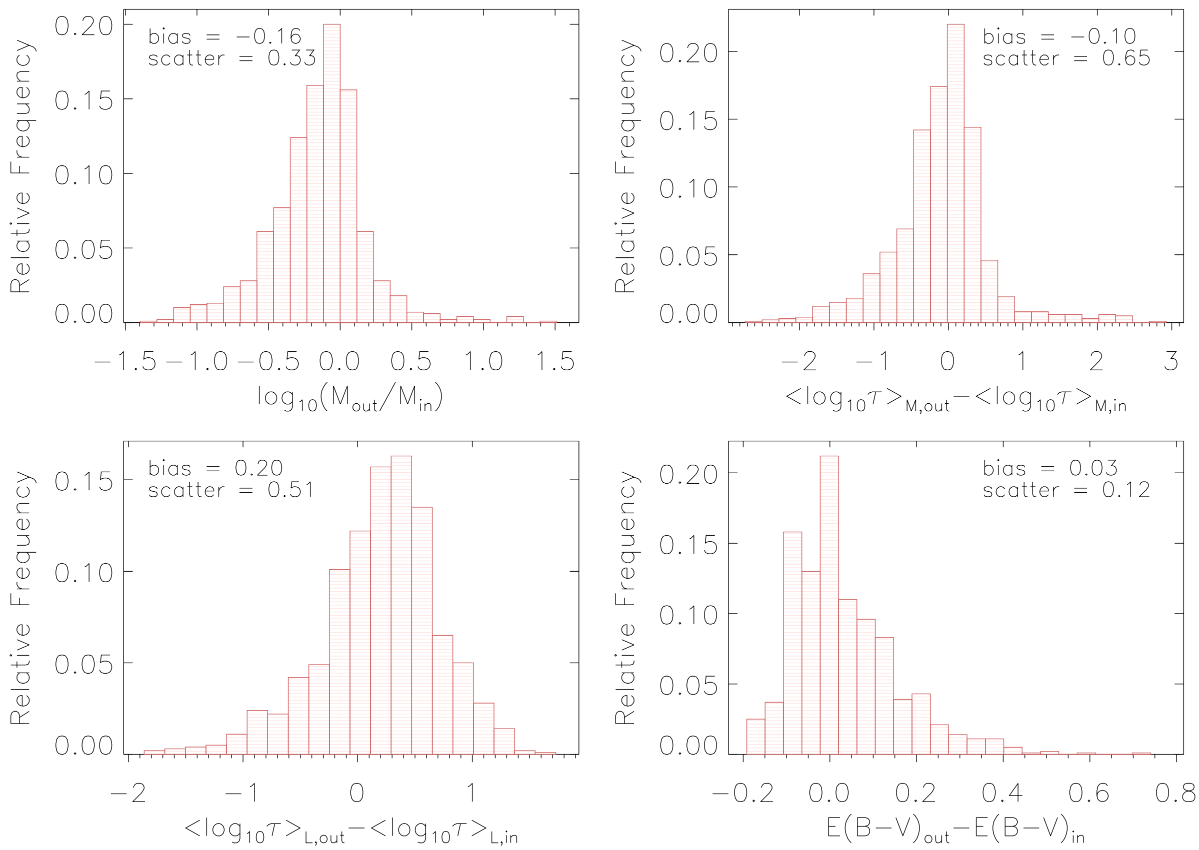

Figure A.5 Histograms of the discrepancy between the input and output values of $M_{\rm NC}$, $\langle \log_{10}\tau\rangle_{\rm M}$, $\langle \log_{10}\tau\rangle_{{\rm L}_B}$, and $E(B-V)$ for the 1000 mock SEDs based on the Walcher et al. (2006) study. The bias and scatter of each quantity plotted is also given.

We illustrate degeneracies between parameters in the fit in Figure A.6, in which we plot the following: the discrepancy between the output and input mass against the discrepancy in $\langle \log_{10}\tau \rangle_{\rm M}$, the discrepancy in mass against the discrepancy in $\langle \log_{10}\tau \rangle_{{\rm L}_B}$, the discrepancy in mass against the discrepancy in reddening, and the discrepancy in $\langle \log_{10}\tau \rangle_{\rm M}$ against the discrepancy in reddening. There is a tight, positive correlation between $\log_{10}(M_{\rm out}/M_{\rm in})$ and $\langle \log_{10}\tau \rangle_{\rm M,out} - \langle \log_{10}\tau \rangle_{\rm M,in}$, and a weaker, positive correlation between $\log_{10}(M_{\rm out}/M_{\rm in})$ and $\langle \log_{10}\tau \rangle_{{\rm L}_B,{\rm out}} - \langle \log_{10}\tau \rangle_{{\rm L}_B,{\rm in}}$, indicating that an overestimated age will result in an overestimated mass, while an underestimated age will result in an underestimated mass. There are also weak, negative correlations between $\log_{10}(M_{\rm out}/M_{\rm in})$ and $E(B-V)_{\rm out} - E(B-V)_{\rm in}$, and between $\langle \log_{10}\tau \rangle_{\rm M,out} - \langle \log_{10}\tau \rangle_{\rm M,in}$ and $E(B-V)_{\rm out} - E(B-V)_{\rm in}$.

In summary, our Monte Carlo SED fitting method produces mass, age, and reddening estimates with little bias for mock SEDs typical of NCs containing multi-age populations. There is good agreement between the scatter in the discrepancies between output and input parameters and the typical span of the 1σ confidence intervals computed by our SED fitting code. This demonstrates that our reported uncertainties are realistic. Our method reliably recovers the correct stellar mass for single-age populations with with ages > 20 Myr, but breaks down for SSPs with ages younger than 20 Myr due to a degeneracy between ~ 8 Myr SSPs and combinations of ~ 3 Myr and ~ 3 Gyr SSPs (where the older SSP accounts for the vast majority of the total stellar mass). Similarly, the method fails to produce accurate age estimates for multi-age populations whose SEDs are dominated by a young SSP. It is unlikely that any of the NCs in our sample have been affected by these failure modes, as their spectral shapes are far too red to be identified with such populations.

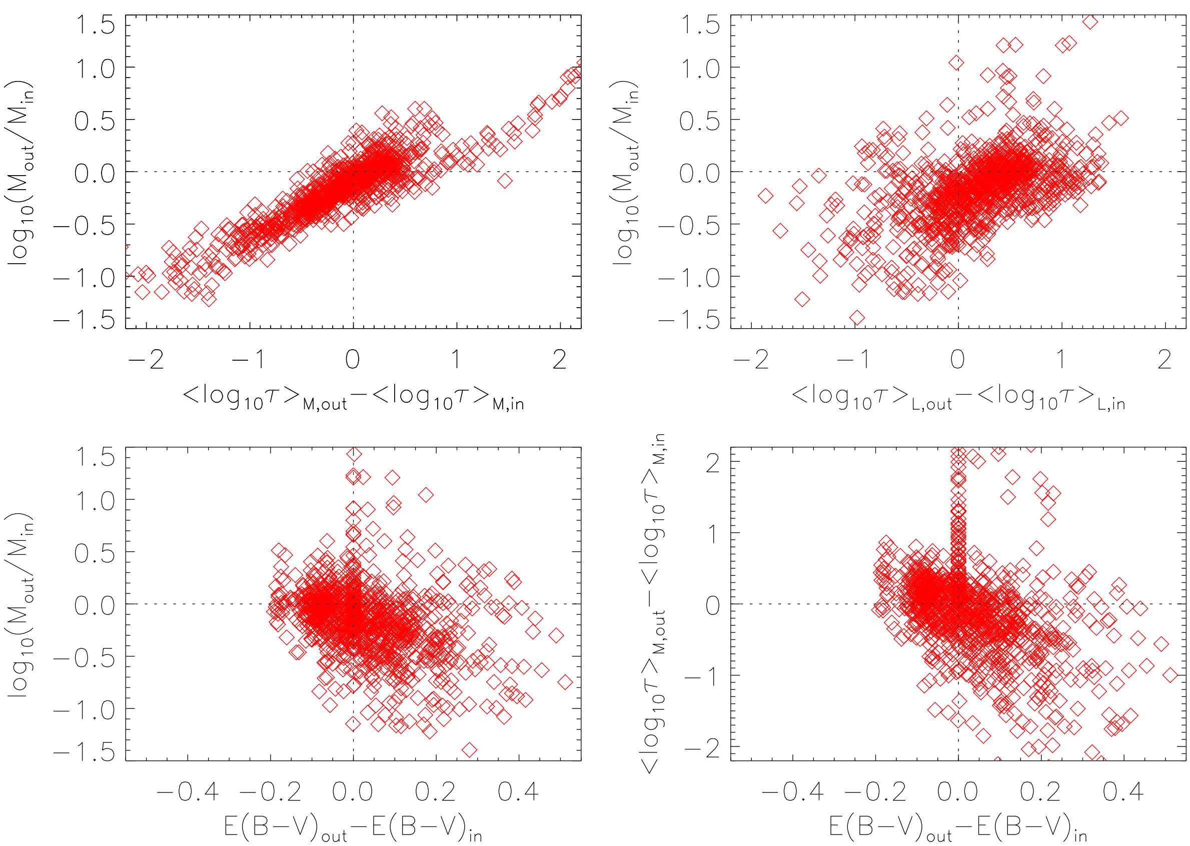

Figure A.6 In the top left panel, we plot the discrepancy between the output and input mass vs. the discrepancy in $\langle \log_{10}\tau \rangle_{\mathrm{M}}$ for the 1000 mock SEDs based on the Walcher et al. (2006) study. In the top right panel, we plot the discrepancy in mass vs. the discrepancy in $\langle \log_{10}\tau \rangle_{\mathrm{L}_B}$. In the bottom left panel, we plot the discrepancy in mass vs. the discrepancy in reddening. In the bottom right panel, we plot the discrepancy in $\langle \log_{10}\tau \rangle_{\mathrm{M}}$ vs. the discrepancy in reddening.